The penetration of a water sediment interface by a parametric array.

Wingham, Duncan J.

Award date:
1984

Awarding institution:
University of Bath

THE PENETRATION OF A WATER SEDIMENT INTERFACE BY A PARAMETRIC ARRAY

Submitted by

DUNCAN J. WINGHAM

for the degree of Ph.D. of the

University of Bath

1984

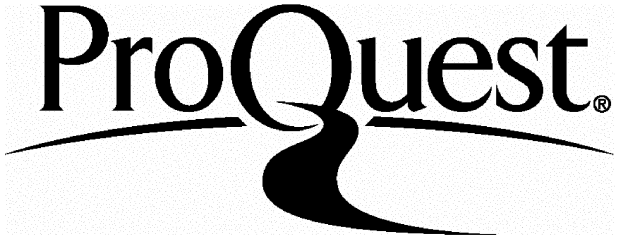

ACKNOWLEDGEMENTS

I would like to thank my advisor, Dr. N.G. Pace, for his guidance and many hours of helpful discussions; and acknowledge too, the importance of his work in providing the foundations of this study. My thanks are also due to Professor H.O. Berktay for his advice and continual interest in my progress, to all the staff of the acoustics group for their expertise, and to all the members of the School of Physics for making my stay at Bath such a happy one.

My thanks also go to Mrs. Paula Keilthy for her excellent typing of this thesis.

I also acknowledge the support of the Procurement Executive of the Ministry of Defence whilst conducting this investigation.

Finally, I would like to thank my parents, for their moral and actual support in this, as previous ventures, and my girlfriend, Emanuela, who waited so patiently, in the face of unequal competition.

ABSTRACT

A theoretical and experimental investigation into the penetration of parametric acoustic beams into sediment is conducted. The theory is based on the assumption that the interface completely truncates the array. With this assumption, the asymtotic farfield of the secondary radiation in sediment is developed and discussed. When the primary field is truncated in its nearfield, the secondary farfield is found to be due to two apertures, one coincident with the transducer and one with the truncation. At subcritical angles of incidence the field is similar to that produced by a conventional beam. At post-critical angles of beam incidence the presence of the truncation aperture results in a steeper and deeper penetration of the beam than in the conventional case. As the trucation moves into the farfield of the primaries, the effect of the truncation aperture is reduced until the parametric beam behaves qualitatively similar to a conventional beam.

Experimental measurements of the secondary field throughout two vertical planes in the sediment are made, and are in good agreement with the theoretical predictions. The wide bandwidth of the parametric array is exploited to distinguish in time Snell's law and evanescent arrivals in the sediment. These latter are seen to be important close to the interface.

It is concluded that the postcritical penetration of parametric sound beams into sediment is due to virtual secondary sources close to the interface and suitably phased.

NOMENCLATURE

$\underline{a}$	Radius vector describing a point on the edge of a circular aperture
$B(\theta)$	See equation (A.1)
$C(\theta,\phi)$	See equation (A.1)
c, c_s	Sound phase velocity in water and sediment respectively
D	See equation (3.7)
D_0	Primary farfield directivity pattern
$d = z-L$	Vertical co-ordinate of the secondary field point in sediment
$E(\theta,\phi_0)$	See equation (A.8)
$\underline{e}$	Radius vector describing a point on the edge of an elliptical aperture
e_x, e_y	Components of e in the directions $\underline{i}$ and $\underline{j}$ respectively
F	See equation (3.11)
$g(\underline{x}',\omega)$	Spatial variation of the primary radiation
$H_1^{(1)}$, $H_1^{(2)}$	First order Hankel functions of the first and second kind
$\hat{I}$, $\hat{I}_s$, $\hat{I}_s^{trunc}$	Transfer function of the parametric array in water, transfer function of the parametric array in sediment and the nearfield truncation aperture contribution to the transfer function
$I_s^{v_1}$, ${}^{r_0}I_s^{v_2}$	The nearfield contribution, and nearfield end of the farfield contribution to the transfer function in sediment when the array is farfield truncated
$\hat{I}$	Plane wave spectrum of the farfield array
$\hat{I}^{v_2}$, ${}^{r_0}\hat{I}^{v_2}$, ${}^{r_p}\hat{I}^{v_2}$	Contribution to the plane wave spectrum of the farfield primary volume, the nearfield end of the farfield primary volume and the truncation end of the farfield volume respectively
i, i_s	Impulse response of the parametric array in water and sediment respectively
$\underline{i}$, $\underline{j}$, $\underline{k}$	Unit vectors in a cartesian co-ordinate system

J_1	First order Bessel function
$J_s(\omega)$	Reciprocity parameter in sediment
$\underline{k}$, $\underline{k}^s$	Wavevector in water and sediment respectively
$k = \frac{\omega}{c}$, $k' = \frac{\omega}{c_s}$	Wavenumber in water and sediment respectively
k_x, k_y	Horizontal components of the wavenumber
k_z, k_z^s	Vertical component of the wavenumber in water and sediment respectively
k_r, k_s	See equation (3.7)
k_x'	See comments preceding equation (3.7)
L	Height of the transducer above the interface
l,u	Secondary source co-ordinates, see Figure 2
$m = 1/n$	Reciprocal refractive index
$n = c/c_s$	Refractive index
p	Secondary field point co-ordinate in water, see Figure 2
p, p_r, p_s	Secondary incident, reflected and transmitted pressure
p_0, p_m	Average primary pressure and primary modulation respectively in the nearfield of the primaries
q	Secondary source strength
R, R_0	Transducer radius and Rayliegh distance
$\underline{r}_t$	Position vector to a field point from the edge of the truncation aperture
r_t^x, r_t^y, r_b^z	Components of $\underline{r}_t$ in the directions $\underline{i}$, $\underline{j}$ and $\underline{k}$
$r = \lvert\underline{x}'\rvert$	Chapter 4 only. Length of $\underline{x}'$
r, r_m, r_t	Path lengths to the field point from a general secondary source point, the centre of the array and the truncation aperture respectively
r_0	The distance from the transducer to the boundary between the nearfield and farfield of the primaries. See Figure 11
r_p	The distance from the transducer to a point on the interface

$s(t)$, $s_{nb}(t)$, $s_{wb}(t)$	A general, narrowband and wideband secondary source wavelet respectively
s	(Appendices only) an integration variable
T	Plane wave transmission coefficient
t	Time
v_1, v_2	Nearfield and farfield secondary source volumes. See Figure 11.
$v_{nb}(t)$, $v_{wb}(t)$	Voltage waveforms used to modulate the primaries for narrowband and wideband array operation respectively
v_0	Arbitrary constant voltage
$w = L\tan\alpha+u/\cos\alpha$	Integration variable. See equation (3.36)
$\underline{x}$, $\underline{x}'$	Position vectors of the secondary field and source points respectively
x, y, x', y'	Horizontal co-ordinates of the secondary field and source points respectively
z, z'	Vertical co-ordinate of the secondary field and source point respectively in water
α	Primary beam incidence angle
α_0	Primary attenuation constant (in Np m^{-1})
$2(\beta-1)$	Non-linearity parameter of water
γ	$\frac{\beta}{8\pi\rho c^4}$
δ	Dirac delta function
ε	Angle between the wavevector $\underline{k}$ and secondary source vector $\underline{x}'$. See Figure 12
ε_0	See equation (4.16)
ε_p	Pole of $(\cos\varepsilon - 1 + 2i\alpha_0/k)$ in the complex ε plane
$\zeta(\underline{x}')$	Vector path of primary radiation to a secondary source point
η,σ	Spherical polar angles describing the direction of $\underline{x}'$. See Figure 12

Θ, Θ_s, Θ_m	See equations (3.16) and (3.26)
θ_0, θ_1, θ_2	Stationary points of Θ, Θ_s and Θ_m, with respect to θ. See also Figure 3
θ_e	Additional stationary point of θ. See also Figure 3
$\theta_c = \sin^{-1}(n)$	Critical angle
θ_M	Primary beam incident angle at which the transmitted secondary pressure at a fixed location is a maximum
θ, ϕ	Integration variables
Φ, Φ_s, Φ_m	See equations (3.16) and (3.26)
ϕ_0, ϕ_1, ϕ_2	Stationary points of Φ, Φ_s and Φ_m with respect to ϕ. See also Figure 3
ϕ_p	Pole of D in complex ϕ plane
ϕ_e	Additional stationary point of Φ. See also Figure 3
λ, λ_0	Secondary and primary wavelength respectively
μ, ρ	Chapter 4 only. Spherical polar angles describing the direction of $\underline{k}$. See also Figure 12
$\underline{\nu}$	General vector
ν_x, ν_y, ν_z	Components of ν in the directions $\underline{i}$, $\underline{j}$, $\underline{k}$
ρ, ρ_s	Density of water and sediment respectively
$\tau(\omega)$, $\tau_1(\omega)$, $\tau_2(\omega)$	Total, first order and second order receiving sensitivity of the hydrophone in water
$\tau_s(\omega)$	Receiving sensitivity of the hydrophone in sediment
ψ	Integration variable
ψ_0	See equation (4.16)
ω, ω_0	Secondary and primary radian frequency
*	Convolution
Re(z), Im(z)	Real and imaginary parts of z respectively

Note on the use of symbols

Although considerable effort has been made to use a consistent set of symbols throughout this thesis, the finite length of the Roman and Greek alphabets has meant that a few symbols have been used twice. It is particularly important to note that in Chapter 4, r and ρ have been used as integration variables and not, as elsewhere, as a path length and water density respectively. The symbol $\underline{k}$ has been used on two occasions to denote the third cartesian unit vector of the set $\underline{i}$, $\underline{j}$ and $\underline{k}$ because of its universal use in this connection; everywhere else in this thesis it is used to denote the wavevector.

There are a few equations which are unrelated to any other part of text and stand alone; here, nonstandard notation is used and explained in the immediate text, as for example equation (5.7). Appendix C, which is written as a self-contained chapter, also uses its own internal notation.

Finally, although when real many of the variables have geometric interpretations which are often made in the text, all variables are in general complex unless otherwise stated.

CONTENTS

		Page
CHAPTER 1	Introduction	1
	The present work	7
CHAPTER 2	General Solutions to Westervelt's Equation	12
	General solutions in an infinite medium	12
	General solutions in two fluid half spaces in contact at a plane boundary	15
CHAPTER 3	The Nearfield Truncated Array	21
	The truncated array in water	24
	The truncated array in sediment	26
	Getting in close: the high angle, high frequency nearfield	33
	Discussion of the asymtotic solutions to the nearfield truncation with numerical examples	38
CHAPTER 4	The Farfield Truncated Array	50
	Discussion of Farfield truncation	59
CHAPTER 5	The Apparatus, Instrumentation and Sediment	62
	Choice of experimental parameters	62
	The tank and gantry	63
	The transmission and reception system	65
	The transmission system	65
	The acoustic filter	76
	The reception system	76
	The sediment	81
CHAPTER 6	Secondary Field Measurements in Water and Sediment	88
	The secondary field in water	89
	The secondary field in sediment	93
	The secondary field in sediment at fixed primary incident angles	93
	The secondary field in sediment with varying angles of beam incidence	103
	Pulse investigation of the shallow arrivals	106

		Page
CHAPTER 7	Discussions and Conclusions	110
	Review of the present work	110
	Limitations and future work	113
	Review of previous work: the secondary nearfield	115
	Conclusions	120
APPENDIX A	Details of the Asymtotic Solution to Equation (3.15)	124
APPENDIX B	The Contour of Steepest Descent	128
APPENDIX C	The Dispersion of Sound in Sediment	132
	The measurement of the phase dispersion	135
APPENDIX D	Three Mathematical Problems	140
REFERENCES		145

LIST OF FIGURES

		Page
Figure 1	The general geometry for the problem	18
Figure 2	The secondary source volume and its co-ordinate description for the case of nearfield truncation	22
Figure 3	The geometric raypaths into the sediment from a nearfield truncated array	32
Figure 4	Geometric interpretation of the stationary point equations for a circular and an elliptical aperture	37
Figure 5	Secondary pressure contours in the sediment in the plane of the beam when the array is incident at 50°	40
Figure 6	Secondary beam cross-section in the sediment when the array incident angle is 50°	41
Figure 7	Variation of secondary pressure with incident angle, in the sediment at a fixed location	42
Figure 8	Secondary pressure contours in the sediment in the plane of the beam when the array incident angle is 70°	44
Figure 9	Secondary beam cross-section in the sediment when the array is incident at 70°	45
Figure 10	Secondary pressure in the sediment vertically beneath the truncation when the array is well postcritical	46
Figure 11	Geometry of the secondary source volume when the array is farfield truncated	51
Figure 12	The co-ordinate description of the secondary source volume for the case of spherically spreading primaries	53
Figure 13	The tanks and gantry arrangement	64
Figure 14	The transmission and reception system	66
Figure 15	The arbitrary function synthesizer	68
Figure 16	The primary frequency modulations and corresponding secondary source wavelets	69

		Page
Figure 17	The transducer construction	72
Figure 18	Primary nearfield (plane wave) transmission sensitivity as a function of frequency	74
Figure 19	Primary transmission sensitivity as a function of range and drive level	74
Figure 20	Primary transmission sensitivity across the beam at four ranges	75
Figure 21	Transmission loss of the acoustic filter	77
Figure 22	B and K 8103 hydrophone receiving sensitivity	78
Figure 23	The effect on the secondary beam pattern of primary nonlinearity on reception	78
Figure 24	The attenuation of sound in sediment	83
Figure 25	The dispersion of sound in sediment	84
Figure 26	The reciprocity calibration through an interface	85
Figure 27	The receiving sensitivity of the B and K 8103 hydrophone in sediment	87
Figure 28	The geometry of the experiments measuring the secondary field in water	90
Figure 29	The variation of secondary pressure with range and truncation length	90
Figure 30	The variation of secondary pressure with range at a fixed truncation length	92
Figure 31	The variation of secondary pressure in cross-section for a fixed truncation length	92
Figure 32	The measured secondary pressure in sediment along the line y = 0 with the array angle at 50°	95
Figure 33	The measured secondary pressure contours in the sediment in the plane of the beam when the array incident angle is 50°	97
Figure 34	The measured secondary pressure contours in the sediment in the plane x = 50 cm when the array incident angle is 50°	98

		Page
Figure 35	The measured secondary pressure contours in the sediment in the plane of the beam when the array incident angle is 70°	100
Figure 36	The measured secondary pressure contours in the sediment in the plane x = 75 when the array incident angle is 70°	101
Figure 37	The geometry of the three hydrophone locations for the fixed location experiments	104
Figure 38	The geometry and associated raypaths for the pulse experiment to distinguish the evanescent arrival	104
Figure 39	The measured secondary pressure in the sediment at the three locations shown in Figure 37 as a function of beam incidence angle.	105
Figure 40	The pulse arrivals in the sediment at a shallowly buried hydrophone as a function of incidence angle	107
Figure 41	A comparison of Muir's[3] results with the numerical calculations of Jarzinski and Flax[12]	117
Figure 42	The displacement of a narrow beam, taken from reference 2	119
Figure 43	(From reference 9) Pressure contours in the sediment due to a phase shaded elliptical spot lying at the interface	119
Figure B.1	The contour of integration for the θ integral	129
Figure B.2	The behaviour of the steepest descent contour as the field point becomes shallow	129
Figure C.1	The experimental arrangement to measure sediment dispersion	137
Figure C.2	The eight arrivals in order of increasing path length through the sediment	138

CHAPTER 1

Introduction

Total internal reflection is familiar to us from elementary physics. It occurs when a wave attempts to enter a higher velocity medium at too high an incident angle: the wave is reflected and the higher velocity medium only disturbed in a region very close to the boundary. The phenomenon is exploited in many optical instruments, from the prism of a camera viewfinder to the optical fibre of high rate transmission lines. In the natural world it is responsible for the mirage and in acoustics the same behaviour produces the SOFAR sound channels of the deep ocean.[1]

In 1979, Muir *et al.*[2] published the results of an experiment which investigated the behaviour of very narrow sound beams incident on a water sediment interface. Ordinarily, one might expect such a study to provide a demonstration of total internal reflection: the sound speed in saturated sediment is typically 1.5 times that of water, giving a critical angle for the water sediment boundary of $\sim 60°$. Muir *et al.*'s experiments examined the dependance of the transmitted pressure in the sediment on the incident angle of the beam. The results were in apparent contradiction of the rules governing total internal reflection: a travelling wave entered the sediment at large postcritical values of beam incidence angle and it was found to penetrate to depths far in excess of a few wavelengths from the interface.

The beams used by Muir *et al.* in these and earlier[3] experiments had two special properties. They were parametric beams, *i.e.*, they were generated non-linearly in the water by intense radiation from a piston source, and they were, by virtue of being parametric beams, very narrow.

The experiments posed intriguing theoretical and practical problems: was the behaviour Muir *et al.* observed because the beam was very narrow, or because it was parametric, and could this property be exploited in problems where, for some reason, the phenomenon of total internal reflection caused practical difficulties?

A particular practical difficulty caused by total internal reflection occurs when attempting to locate and/or identify by the use of sonar beams targets which lie just beneath a refracting interface. The problem becomes acute when the "line-of-sight" (*i.e.*, the straight line between the source and the target) makes a very shallow angle with the interface. Energy will not reach the target along this path because it will be totally internally reflected. In order that a sonar beam should be incident upon such a target, it must be incident upon the interface at an angle close to the critical angle. Here, it suffers large losses due to reflection and refraction. This behaviour limits the angular range, and hence aerial coverage, of a sub-bottom sonar system. The energy arriving at the target is so weak it cannot compete with scattered energy from the interface. An early observation[3] of Muir *et al.* was that when their hydrophone was shallowly buried, the maximum pressure transmitted into the sediment from a narrow parametric beam occured when the beam was coincident with the line-of-sight to the object, and not the Snell's law path between the source and object, as might have been expected. Potentially, at least, the narrow parametric beam offered some hope of improving the angular performance of sub-bottom profilers.

A theoretical explanation of these phenomena would thus have a two-fold purpose. Firstly, it would resolve the contradiction between Muir *et al.*'s results and linear theory. Secondly, it would provide a quantitative method to evaluate the potential of narrow parametric beams as sub-

bottom profilers.

A parametric beam is formed by launching a travelling wave with a high intensity from a sonar transducer. This high intensity wave, directly radiated from the transducer, is termed the primary field, and is of sufficient amplitude for non-linear effects in the water to be significant. Should the primary field contain two frequencies, say ω_1 and ω_2, then a consequence of the non-linearity is the generation, in the water, of travelling waves at frequencies $(\omega_1+\omega_2)$ and $(\omega_1-\omega_2)$. These latter, subharmonic frequencies are termed the secondary, or difference frequency field. In a now celebrated paper,[4] Westervelt showed that the difference frequency field, $p(\underline{x},t)$, satisfied an inhomogeneous wave equation whose source term was quadratic in the primary field, $p_0(\underline{x},t)$:

$$\nabla^2 p(\underline{x},t) - \frac{1}{c^2}\frac{\partial^2 p}{\partial t^2}(\underline{x},t) = \frac{\beta}{\rho c^4}\frac{\partial^2}{\partial t^2} p_0^2(\underline{x},t) \quad . \tag{1.1}$$

It was Lighthill,[5] however, who realised the significance of the fact that the primary field itself was a solution to equation (1.1), (the source term being the transducer motion). With a transducer used to generate a plane wave primary field, a set of difference frequency sources would be generated, cophasal in the direction of the primary plane wave but none other, and hence should generate a very narrow difference frequency beam in the direction of the primary radiation: the parametric acoustic array.[6] In an unbounded medium they are characterised by very narrow, sidelobe-less beams.

It was the narrowness of the beams which was first thought to be responsible for the unusual effects seen by Muir *et al.* and several theoretical studies of the behaviour of extremely narrow conventional beams [*i.e.*, beams which would result from very, (probably impossibly), large transducers] incident on a water-sediment interface were made in order to provide

an adequate explanation of these phenomena. Horton based his discussion[7] on the integral solution to the corresponding problem with a point source. This integral represents the field in the sediment as the super-position of a plane wave spectrum whose asymtotic approximation at high frequencies may be interpreted as the Snell's law raypath of geometrical optics between source and receiver.[8] Horton recognised this description to be even more suited to the behaviour of a narrow beam: the axis of the beam will follow the Snell's law raypath into the sediment, and the maximum pressure in the sediment will fall along the axis of the beam. He investigated the raypath into lossy sediment at incident angles greater than critical and found it to dip increasingly steeply as the incident angle increased. He concluded this raypath to be responsible for Muir *et al.*'s results. These arguments were based solely on the phase of the arrival in the sediment, and did not give consideration to the amplitude of the transmitted field. This was unfortunate, for the raypath he had investigated belonged to an evanescent wave, which decays exponentially with depth from the boundary and could not, therefore, be responsible for the results seen by Muir *et al.*

Tjotta and Tjotta[9] tried a rather different approach. They argued that a narrow beam incident upon the interface would produce a spot on the sediment, (in much the same way that a searchlight throws a spot onto its target). A very narrow beam would throw a very sharp edged spot; the field from such a spot in sediment could be calculated by applying Helmholtz's integral over the surface of the spot. They showed that such a spot would diffract into the sediment, even at postcritical angles of beam incidence, and provided near- and far-field expressions for such a case. As an explanation of Muir *et al.*'s experiments, however, this description was flawed. Parametric beams may be narrow, but they do not have sharp edges and they should not diffract in this fashion. The steeply dipping beams at postcritical angles of incidence were achieved by the disingenious use

of a boundary condition which was not physically realistic, but forced the transmitted pressure to zero near the interface. Agreement with Muir's results was obtained by the rather arbitrary selection of a beam profile.[10] In addition, neither they nor Horton could shed any light on the role of the parametric nature of the beam.

This neglect was important. The mode of generation of a parametric beam is particularly relevant to the present problem because the secondary sources, called virtual sources, are widely distributed in space; as widely distributed as the primary field $p_0(\underline{x}',t)$ itself. This introduces the possibility that the effects seen by Muir *et al.* were not due to the narrowness of the beam at all; but to the presence of virtual sources close to the interface being much nearer to a receiver in the sediment than those virtual sources at the transducer.

Two studies which explicitly acknowledged the parametric nature of the beam[11,12] considered the primary field to be narrow enough to be considered a line distribution of point sources. Each point source was assumed to transmit sound through the interface in a manner described by the asymtotic solution previously exploited by Horton. The sources were numerically integrated over the length of the array to calculate the transmitted pressure in the sediment. Both these studies were considerably more successful in predicting the qualitative features of Muir *et al.*'s results, in particular they both exhibited the "line-of-sight" property of the experiments. It became clear that the virtual sources close to the interface could not be ignored in any description of the secondary field in the sediment. However, much of the physics of the problem, as is often the case with numerical studies, remained unclear. It was not understood why, in the case of Jarzinski and Flax's calculations for example, the maximum pressures in the sediment were consistently over-

estimated, sometimes by as much as 9dB, and their position as a function of incident angle also consistently over-estimated. The problem still awaited a useful theoretical formulation.

A very important contribution to the understanding of the problem was made by Pace and Ceen. This arose from their investigations into pulsed parametric arrays.[13,14] In common with much heterodyne equipment, the parametric array can generate signals of very wide bandwidth. For example: a 1 MHz transducer radiating a primary field with a bandwidth of 100 kHz could generate a secondary field whose spectrum was centred at 175 kHz with a bandwidth of 300 kHz. This wide bandwidth permits a parametric array to generate very short pulses. Working in water, Pace and Ceen used very short signals to demonstrate that when the primary field of a parametric array is truncated in its nearfield, the secondary field radiated from it is comprised of two arrivals, the first associated with the transducer, the second associated with the truncation. This second arrival has no analogue in the primary field. These experiments were complemented by an elegant description of the parametric array impulse response in water. They then investigated the secondary field in sediment and found the same two arrivals to be present there too: the interface was truncating the primary field and providing a second radiating 'aperture', in addition to the transducer, from which energy could enter the sediment. This second, truncation, aperature could explain in broad qualitative terms the results of Muir *et al.*'s experiments. The penetration at high angles of primary beam incidence was due to the arrival in sediment from this truncation aperture. Its arrival time at the receiver in the sediment varied with primary beam incidence angle, which dictated the position of the truncation. Its intensity was also a function of beam incidence angle by virtue of the increasing length of the array as the incident angle increased.

The success of Pace and Ceen's model[13] in predicting the behaviour of the truncation aperture in water suggested that a model of equal sophisitication would be similarly successful in predicting the behaviour of the truncation aperture in sediment. Such a model would acknowledge the finite width of the primary beam and the obliqueness of its truncation at the interface; but would not concern itself with the details of the primary field. In the present study a quantitative description of just such a model is developed, discussed and compared with experiment.

The present work

The purpose of this study is to provide a theoretical description of the secondary pressure in sediment due to a parametric beam incident on the water sediment interface and to compare this description with the measured field in sediment from such a source. At the beginning of this study the only closed form solution to the problem available[9] had been derived on the assumption that the modification of the primary field by the interface could be ignored, contrary to the most important conclusion to be drawn from Pace and Ceen's work. The theory of reference 9 could not account for the two arrivals found in sediment for certain geometries.

The theoretical account presented here explicitly acknowledges the truncation of the primary field by the interface. It is based upon the representation of the Green's function of equation (1.1) as an integral over a plane wave spectrum. This is the representation used by Horton[7] in his discussion of the problem and the asymtotic representation of which Jarzynski and Flax[12] and Moustafa[11] numerically integrated over a line array. The extension of the point surce solution, the Green's function, to an arbitrary distribution of sources is formally easy: the Green's function is convolved with the spatial distribution of the sources. Expressed as three dimensional Fourier integrals, *i.e.*, as plane wave spectra, the

problem is formally even simpler: the spectrum of the Green's function is multiplied by the spectrum of the source distribution. This is a particularly useful form for the present problem because the geometry of the plane waves matches that of the plane boundary and applying the boundary conditions is straightforward. Berktay and Moustafa[15] replaced the point source spectrum with that corresponding to a conventional aperture to investigate the behaviour of narrow beams penetrating sediment.

In the present study the point source spectrum is replaced with the spectrum of the parametric array. The calculation of this spectrum is equivalent to calculating the farfield of the parametric array. In an infinite medium this problem has received considerable attention.[16-19] These analyses are of little direct use because of the truncation, which reduces the symmetry of the problem. However, a closed form may be calculated if the truncation falls in the nearfield of the primary field. If the truncation lies in the farfield of the primaries only an asymtotic form is available for the plane wave spectrum.

The calculated spectrum is substituted into the integral solution to the problem which is then evaluated asymtotically in a similar fashion to the point source case by a combination of stationary phase[20] and steepest descent[21] methods. This yields high frequency, farfield solutions for the field in sediment, from which considerable qualitative and quantitative understanding is deduced.

The case of nearfield truncation is the most important and is given the most attention. This is the subject of Chapter 3. A simple description of the primary field in its nearfield is employed in order to obtain closed form solutions for the array spectrum. It is assumed that when incident on lossy sediment the transmitted part of the primary field is rapidly attenuated, effectively truncating it. The reflected part of

the primary field is, in the first instance, ignored because its contribution is small.

On these assumptions, the high frequency secondary farfield in the sediment is derived, together with expressions indicating the range of validity of the theory. By making the additional assumption that the incidence angle of the array is well postcritical, expressions for the nearfield of the truncation aperture are derived. The chapter is concluded with a discussion of these solutions, illustrated with numerical examples chosen to fit the later experimental parameters.

In Chapter 4, the case of farfield truncation is studied. The general integral form for the parametric array plane wave spectrum is constructed and found to split into two terms, one associated with nearfield of the primaries and the second with the truncation. Both terms are too complex for exact integration: a mixture of heuristic and asymtotic approximations are exploited to examine their properties. The chapter closes with a discussion of these properties and in particular, addresses the question of how far distant the array must be from the interface before its behaviour is indistinguishable from a conventional array.

This chapter concludes the theoretical work and the experimental investigation is introduced in Chapter 5, which details the apparatus, instrumentation and sediment. A description is given of the construction and calibration of 1.85 MHz, 4 cm diameter transducer, together with measurements of its primary and secondary fields in water. These latter are compared with the predictions of Chapter 3. The transmission and reception system are described and their linearity assessed. The 250 μm ϕ sand, chosen as a typical sediment, has its physical and acoustical properties described and measurements of its attenuation and dispersion are presented. These

latter are the first of their kind ever made: they are considered in greater detail in appendix C.

Chapter 6 presents the measurements of the secondary field in sediment due to the parametric array incident on the interface in the nearfield of the primaries. The object of these experiments was to confirm the main qualitative features of the model discussed in Chapter 3 and to see how good the qualitative predictions are.

The field at fixed angles of primary beam incidence angle the secondary field was measured in two vertical planes through the sediment, one containing the primary beam axis and the other perpendicular to it. A sub- and post-critical angle, 50° and 70° respectively, was investigated and the results are presented here in the form of contour plots of the pressure variation throughout the planes. The field at a fixed location in the sediment was studied as a function of primary beam incidence angle; three depths were chosen to ensure a complete picture emerged. These measurements are described, and, together with the contour plots, compared with the theoretical predictions of Chapter 3.

The final experiment described in Chapter 6 is an investigation of the field very close to the interface, using the array in the pulsed mode. In a similar way to Pace and Ceen,[13,14] the wide bandwidth, short time-width signals are used to distinguish the various arrivals. The time domain data are compared with the theoretical arrival times and the Snell's law and evanescent arrivals distinguished.

In the concluding chapter, Chapter 7, a review of the main results of the thesis is presented. The previous literature in the field, particularly references 2, 9 and 11, is reviewed in the light of the present findings, together with a discussion of the nearfield of the secondary field, and the possibility, originally raised by Muir *et al.*[2], that the

parametric beam is significantly displaced. The thesis is concluded with a general discussion of the features of the parametric field in sediment.

CHAPTER 2

General Solutions to Westervelt's Equation

Westervelt's equation for the scattering of difference frequency sound from a primary sound field is the inhomogeneous wave equation. General solutions, both in an infinite medium and in the presence of a boundary, are well known in both acoustic[8] and electromagnetic[22] theory. In this chapter these general solutions are exploited, and a number of integral solutions to equation (1.1) in an infinite medium are introduced and cast in a form particularly suited to the present problem. The boundary is introduced and the solutions modified to take account of it. The resulting integral solutions form the starting point for the specific cases discussed in later chapters.

General solutions in an infinite medium

The general solution to Westervelt's equation (1.1) for the difference frequency pressure in an infinite medium is

$$p(\underline{x},t) = \frac{\rho}{4\pi}\int_V \frac{\partial}{\partial t}\frac{q(\underline{x}',t-|\underline{x}-\underline{x}'|/c)}{|\underline{x}-\underline{x}'|}\,d\underline{x}' \quad . \tag{2.1}$$

The source function $q(\underline{x}',t)$ is quadratic in the primary pressure field:

$$q(\underline{x}',t) = (\beta/\rho^2c^4)\frac{\partial}{\partial t}p_0^2(\underline{x}',t) \quad . \tag{2.2}$$

It has been established[23] that equations (2.1) and (2.2) are of sufficient generality to include the case where $p_0(\underline{x}',t)$ is the primary field radiated

from a large piston at low Mach number. To this degree of accuracy, $p_0(\underline{x}',t)$ is given by its parabolic approximation,[24] and as a result Berktay's[25] "self-demodulation" result may be used so that we can write

$$q(\underline{x}',t) = (\beta/2\rho^2c^4)g^2(\underline{x}',\omega_0)\frac{\partial}{\partial t}\, p_m^2(t - |\underline{\zeta}(\underline{x}')|/c) \quad . \tag{2.3}$$

Here, $g(\underline{x}',\omega_0)$ accounts for the spatial variation of the primary; $p_m^2(t)$ is the average nearfield pressure.

Substitution of equation (2.3) into (2.1) yields

$$p(\underline{x},t) = \frac{\beta}{8\pi\rho c^4}\int_V g^2(\underline{x}',\omega_0)\frac{\partial^2 p_m^2(t-(|\zeta(\underline{x}')|+|\underline{x}-\underline{x}'|)/c)}{|\underline{x}-\underline{x}'|}\, d\underline{x}' \tag{2.4}$$

Equation (2.4) may be rewritten

$$p(\underline{x},t) = s(t)*\frac{\beta}{8\pi\rho c^4}\int_V g^2(\underline{x}',\omega_0)\frac{\delta(t-(|\zeta(\underline{x}')|+|\underline{x}-\underline{x}'|)/c}{|\underline{x}-\underline{x}'|}\, d\underline{x}' \ , \tag{2.5}$$

and we can identify

$$i(\underline{x},t) = \frac{\beta}{8\pi\rho c^4}\int_V g^2(\underline{x}',\omega_0)\frac{\delta(t-(|\zeta(\underline{x}')|+|\underline{x}-\underline{x}'|)/c}{|\underline{x}-\underline{x}'|}\, d\underline{x}' \tag{2.6}$$

as being the impulse response of the parametric array. This definition is consistent with Pace and Ceen's,[13] but not that of Rolleigh,[26] who includes the travel time to $\underline{x}$ within an "input" term $p_m^2(t-(|\underline{x}'|+|\underline{x}-\underline{x}'|)/c)$. I prefer the present definition as being neater: the "input", or

secondary source, term

$$s(t) = \frac{\partial^2}{\partial t^2} p_m^2(t) \tag{2.7}$$

is determined entirely by the voltage supplied to the transducer; the impulse response of equation (2.6) is a function of the geometry alone. There is, of course, no "correct" choice.

The transfer function, $I(\underline{x},\omega)$, is defined by

$$I(\underline{x},\omega) = \frac{1}{\sqrt{2\pi}} \int_{-\infty}^{+\infty} i(\underline{x},t) e^{-i\omega t} dt \quad , \tag{2.8}$$

which, from equation (2.6), yields

$$I(\underline{x},\omega) = \frac{\beta}{8\sqrt{2}\pi^{3/2}\rho c^4} \int_v g^2(\underline{x},\omega_0) \frac{e^{-ik(|\zeta(\underline{x}')|+|\underline{x}-\underline{x}'|)}}{|\underline{x}-\underline{x}'|} d\underline{x}' \quad . \tag{2.9}$$

A very useful form for $I(\underline{x},\omega)$ is obtained from Weyl's integral representation of a point source:[8]

$$\frac{e^{-ik|\underline{\upsilon}|}}{|\underline{\upsilon}|} = \frac{i}{2\pi} \iint_{-\infty}^{+\infty} \frac{e^{-i(k_x \upsilon_x + k_y \upsilon_y + k_z \upsilon_z)}}{k_z} dk_x dk_y \quad , \tag{2.10}$$

where

$$\underline{\upsilon} = \upsilon_x \underline{i} + \upsilon_y \underline{j} + \upsilon_z \underline{k}$$

and

$$k_z = \sqrt{(k^2 - k_x^2 - k_y^2)} \quad , \tag{2.11}$$

the sign of the square root taken so that $I_m(k_z) < 0$. Substituting for the point source in equation (2.9) with equation (2.10) and reversing the order of integration gives

$$I(\underline{x},\omega) = \frac{\beta i}{8(2\pi)^{3/2}\rho c^4} \int_{-\infty}^{+\infty}\int \hat{I}(k_x,k_y,\omega) e^{-ik_x x - ik_y y - ik_z z} \, dk_x dk_y \quad , \quad (2.12)$$

where

$$\hat{I}(k_x,k_y,\omega) = \frac{1}{k_z} \int_V g^2(\underline{x}',\omega_0) e^{-ik|\zeta(\underline{x}')| + ik_x x' + ik_y y' + ik_z z'} d\underline{x}' \quad (2.13)$$

The exponentials in equation (2.12) are themselves solutions of the homogeneous linear wave equation by virtue of equation (2.11), so that it is natural to term $\hat{I}(k_x,k_y,\omega)$ the "plane wave spectrum" of the parametric array. It is also worth noting that solving the integral of equation (2.13) is equivalent to calculating the farfield of $I(\underline{x},\omega)$. Making the usual farfield approximations of

$$|\underline{x}-\underline{x}'| \tilde{-} |\underline{x}| - \underline{x}'.\hat{\underline{n}} \quad (2.14)$$

in the integrand's phase term and $|\underline{x}-\underline{x}'| \tilde{-} |\underline{x}|$ in its denominator reduces the integral of equation (2.9) to the integral of equation (2.13).

General solutions in two fluid half spaces in contact at a plane boundary

This study is concerned with the behaviour of a parametric array near a water sediment interface. Accordingly, the solution for the impulse response, equation (2.6), must be modified to take account of the boundary;

and this modification must recognise the fact that both the general solution for the secondaries, equation (2.1), and the particular solution for the primaries $p_0(\underline{x}',t)$, of the inhomogeneous wave equation (1.1), are incomplete in the presence of a boundary. A sufficiently detailed account, (for the purposes of this study), of the new solution for the primary pressure near an interface can be deduced from the work of Brekhovskikh[27] (reflection) and a paper by Berktay and Moustafa[11] (transmission). It may be concluded from these sources that a narrow high frequency beam incident on a fluid fluid boundary gives rise to a geometrically reflected beam and a Snell's law refracted beam at subcritical angles and an evanescent wave at post critical angles. The presence of small signal absorption in the sediment makes no qualitative change to this picture.

At subcritical angles of primary beam incidence this small signal absorption is assumed to make the contribution to the secondary from the primary field in the sediment negligible; with evanescent primary penetration this will certainly be the case at post critical angles of primary beam incidence. For example: the transmission coefficient at normal incidence in the experimental part of this study is 1.34, the small signal attenuation 0.4 dB/λ, so that the secondary source strength in the sediment will be 11 dB down within one secondary wavelength of the interface.

The reflected primary is incorrectly phased to contribute to the secondary and we initially assume that it too may be ignored. This is not a necessary assumption, an additional reflected array may be added to the incident one. However, a more comprehensive light may be shed on this problem once we have solved for the secondary field from the incident array, (see the discussion of Chapter 3).

The justification for these *a priori* theoretical assumptions (and historically the reason for making them), is the work of Pace and Ceen[13,14] on truncated parametric arrays, the importance of which has been noted in the introduction, and whose major conclusion is that the secondary field in sediment contained an arrival which could be associated with the discontinuous truncation of the primary beam by the interface.

Thus, to the extent that it affects the secondary field, the primary field $p_0(\underline{x}',t)$ is assumed to be zero in the half-space occupied by the sediment, and unchanged in the water above it. In equation (2.1) this can be accommodated by changing the limits of V, the volume over which the primaries are integrated.

Formally then, equation (2.1) is unaffected by the change in the primaries due to the interface. This is not the case when we come to calculate the secondary pressure. However, with the transfer function and hence pressure [*via* equation (2.5)] in the form equation (2.12) (with V suitably redefined), the formal calculation of the impulse response in the sediment (treated as a fluid) is identical to that for a point source. This problem, a classic problem in seismology, is dealt with in a number of textbooks, see, for example, reference 8, and so will only be summarised here. That Weyl's integral, equation (2.10), should lead to a form suitable for this problem is, of course, no coincidence: it was introduced for just this purpose. Sommerfeld's[28] more compact expansion in cylindrical waves has not been exploited because its symmetry is not echoed by the array volume.

In Figure 1, the general geometry for this and succeeding discussions is shown. Two fluids, characterised by sound speed and densities c,ρ and c_s,ρ_s respectively, occupy two half spaces in contact at a plane boundary.

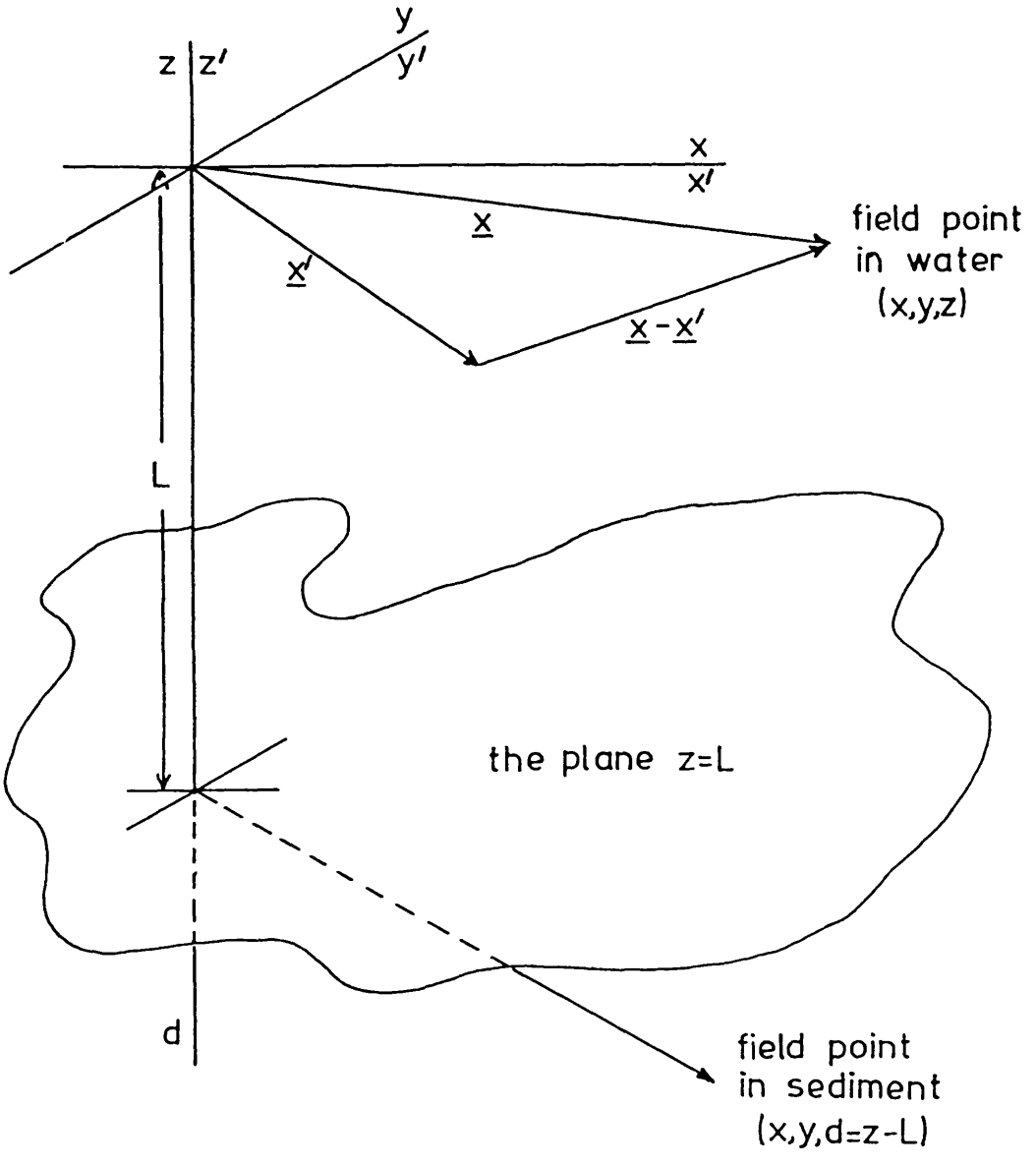

Figure 1. The general geometry for the problem. Two half spaces are in contact at a plane boundary. The sources lie entirely in the upper half space and are described by the co-ordinates x', y', z'. The field point in the upper half space is described by co-ordinates x, y, z and in the lower half space by co-ordinates x, y, d = z-L.

The sources are completely contained in the upper fluid; the interface lies in the plane z = L in the co-ordinates x,y,z chosen to describe the secondary field in the upper medium; the field in the sediment is described by an alternative depth co-ordinate, d = z-L, measured positive from the interface.

The calculation proceeds by representing a reflected wave (in the upper medium) and a transmitted wave (in the lower) in the form of equation (2.12), as integrals over as yet unknown plane wave spectra. These are then substituted into the boundary conditions requiring continuity of pressure and normal velocity at the interface:

$$p_s = p + p_r$$

and (2.15)

$$\frac{\rho}{\rho_s}\frac{\partial p_s}{\partial z} = \frac{\partial p}{\partial z} + \frac{\partial p_r}{\partial z} \quad .$$

Algebraic elimination of the reflected wave allows the formal solution for the transfer function in the sediment to be written down:

$$I_s(x,y,d,\omega) = \frac{\beta i}{8(2\pi)^{3/2}\rho c^4}\int_{-\infty}^{+\infty}\int T(k_x,k_y,\omega)\hat{I}(k_x,k_y,\omega)e^{-ik_x x - ik_y y - ik_z L - ik_z^s d}\,dk_x dk_y, \tag{2.16}$$

where

$$k_z^s = \sqrt{(\omega^2/c_s^2 - k_x^2 - k_y^2)} \quad \text{with} \quad I_m(k_z^s) < 0 \tag{2.17}$$

and

$$T(k_x,k_y,\omega) = \frac{2\rho_s k_z}{(\rho_s k_z - k_z^s)} \quad , \tag{2.18}$$

which can be identified as the plane wave transmission coefficient.[27] In general, c_s, and hence k_z^s, will be complex as the lower medium is assumed absorbing.

To obtain an explicit form for $I_s(x,y,d,\omega)$ the integration (2.13) over the secondary source volume V must be performed. Because of the differing geometry, the treatment of this integral depends on whether the termination at the interface is in the near- or farfield. As it turns out, this distinction has a physical significance in that it (roughly) determines the performance of the array in sediment. The two cases are treated separately, starting first with the most important: the nearfield truncation.

CHAPTER 3

The Nearfield Truncated Array

This chapter is concerned with calculating the radiated farfield secondary pressure in sediment from a parametric array when the incident primary beam strikes the interface within its nearfield. As Westervelt pointed out in one of his early papers,[29] linear beam theory is not in a satisfactory enough state to allow an exact substitution in equation (2.3) for the primary pressure in the nearfield. The primary field is therefore approximated by collimated plane waves lying within a cylinder bounded at one end by the transducer and at the other by the truncation which may, or may not, be normal to the primary beam axis. In the co-ordinates of Figure 2, the functions $g(\underline{x}',\omega_0)$ and $\zeta(\underline{x}')$ take the following definitions:

$$g(\underline{x},\omega_0) = e^{-\alpha_0 \ell} , \tag{3.1}$$

$$|\zeta(\underline{x}')| = \ell \tag{3.2}$$

and V is the volume shown in Figure 2. As we shall see, there would be little point in designing an array for which $\alpha_0 \ell$ was not very small within V, so equation (3.1) is simplified still further by putting

$$g(\underline{x}',\omega_0) = 1 \quad . \tag{3.3}$$

Physically equations (3.2) and (3.3) are likely to be good approximations if the secondary wavelengths are very long in comparison with variations in $g(\underline{x}',\omega)$. They have been used almost universally by investigators dealing explicitly with the nearfield.

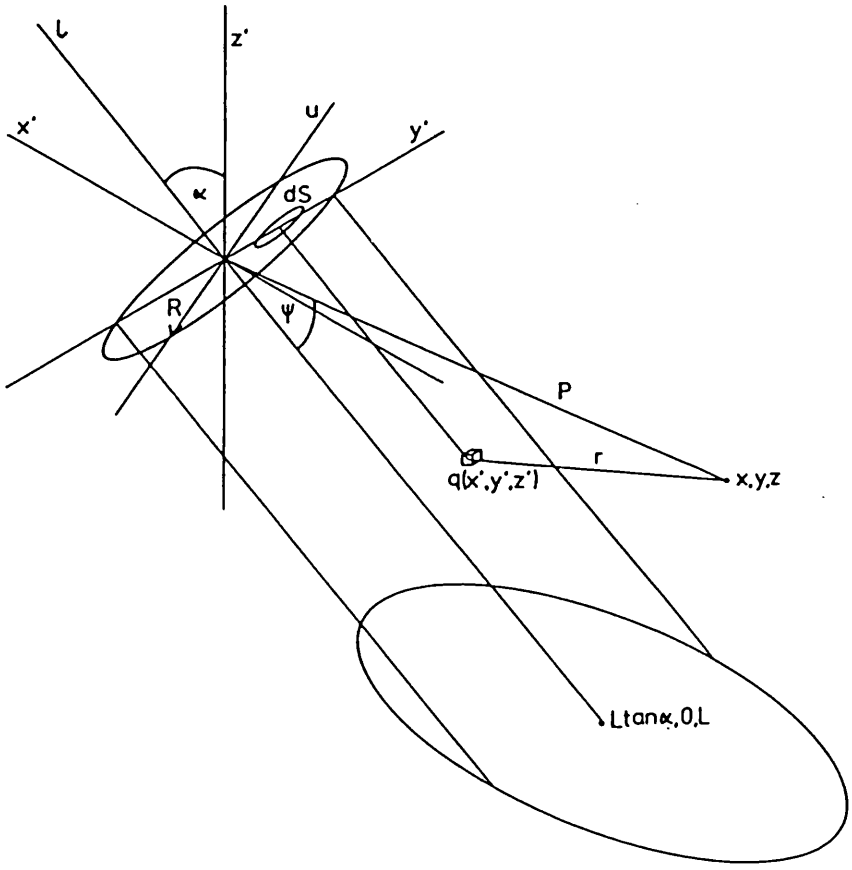

Figure 2. The secondary source volume V and its co-ordinate description for the case of nearfield truncation.

With these simplifications the plane wave spectrum can be calculated exactly from equation (2.13), which, with equations (3.2) and (3.3) becomes

$$\hat{I}(k_x,k_y,\omega) = \frac{1}{k_z}\iint_{S\ L} e^{-ik\ell + ik_z z' + ik_x x' + ik_y y'}\,dudyd\ell \qquad (3.4)$$

where L singles out a particular line array and S is the transducer aperture. The L integral integrates directly to give

$$\hat{I}(k_x,k_y,\omega) = i/k_z(k_x\sin\alpha + k_z\cos\alpha - k)\cdot$$

$$\iint_S [e^{i(k_z u\sin\alpha + k_x u\cos\alpha + k_y y')} -$$

$$e^{i(k_z L + k_x(L\tan\alpha + u/\cos\alpha) + k_y y' - k(L/\cos\alpha + u\tan\alpha))}]\,dudy' \qquad (3.5)$$

with u as in Figure 2. This integral has two terms corresponding to each end of the volume. The first describes a set of time coincident sources lying at the transducer, the second term describes a set of sources lying at the termination with a phase shading corresponding to the arrival time of the primary field from the transducer.

Both these terms may be reduced to a standard form by a suitable redefinition of the wavenumbers. The first term requires rotating the k_x and k_z axis so that $k_x' = k_x\cos\alpha - k_z\sin\alpha$ lies in the plane of the transducer. The second requires defining $k_x' = k_x/\cos\alpha - k\tan\alpha$ to take account of the phase shading. Then both integrals are of the standard form

$$\iint_S e^{ik_x' u + ik_y y}\,dudy' \quad ,$$

and equation (3.5) integrates to

$$\hat{I}(k_x,k_y,\omega) = \frac{2\pi i}{k_z} D(k_x,k_y,\omega) \cdot$$

$$\left[RJ_1(k_r R) - e^{-ikL/\cos\alpha + ik_z L + ik_x L\tan\alpha} RJ_1(k_s R)\right] \qquad (3.6)$$

$$\frac{}{k_r} \qquad\qquad \frac{}{k_s}$$

where $D(k_x,k_y,\omega) = 1/(k_x\sin\alpha + k_z\cos\alpha - k)$,

$$k_r = [(k_x\cos\alpha - k_z\sin\alpha)^2 + k_y^2]^{\frac{1}{2}}$$

and (3.7)

$$k_s = [(k_x/\cos\alpha - k\tan\alpha)^2 + k_y^2]^{\frac{1}{2}} ,$$

the square roots taken so that $\mathrm{Re}(k_r) > 0$ and $\mathrm{Re}(k_s) > 0$. The second of these two terms $RJ_1(k_s R)/k_s$ is identical to that of Tjotta and Tjotta.[9] It is important to note the integration is over the primary beam cross-section; R being the transducer radius.

It will be useful to have an alternative form for $\hat{I}(k_x,k_y,\omega)$ near the poles of $D(k_x,k_y,\omega)$. As $k_x \to k\sin\alpha$, and $k_y \to 0$, k_s and $k_r \to 0$, $J_1(k_r R)$ and $J_1(k_s R) \to k_r R/2$ and $k_s R/2$ respectively and

$$\hat{I}(k_x,k_y,\omega) \simeq \frac{-2\pi R^2}{k_z} D(k_x,k_y,\omega) \cdot$$

$$e^{i(k_z L + k_x L\tan\alpha - kL/\cos\alpha)/2} \sin(L/2\cos\alpha D(k_x,k_y,\omega)) \quad . \qquad (3.8)$$

The truncated array in water

The ability to truncate the primaries artificially means that the description of the primaries, equations (3.1) - (3.3), can be investigated

independently of the sediment. Remembering the comments following equations (2.13) and (2.14), the farfield in water with a normal truncation ($\alpha = 0$) follows directly from equation (3.7):

$$I(\underline{x},\omega) \sim \frac{i\sqrt{2}\pi\gamma e^{-ikP}RJ_1(Rk\sin\psi)}{Pk^2\sin\psi(1 - \cos\psi)}\left[e^{-ikL(1 - \cos\psi)} - 1\right] \quad , \qquad (3.9)$$

large $|\underline{x}|$

with P and ψ as in Figure 2. In fact, equation (3.9) may be improved upon by the addition of a Fresnel-type of correction to improve the description of the phase variation with the length of array. The correction is identical to that described by Berktay[30] for line arrays and so we will simply quote the result. With $a = (k\sin^2\psi)/2P$ and $b = k(1 - \cos\psi)$,

$$I(P,\Psi) \simeq \frac{-i\gamma(\pi/\sqrt{a})RJ_1(Rk\sin\psi)}{k\sqrt{2}P\sin\psi(1 - \cos\psi)} e^{-ik(P - b^2/4a)} F(P,\psi) \qquad (3.10)$$

where $$F(P,\psi) = \int_{\sqrt{\frac{2}{\pi}}\left(\frac{b}{2\sqrt{a}} - \frac{\sqrt{a}h}{2}\right)}^{\sqrt{\frac{2}{\pi}}\left(\frac{b}{2\sqrt{a}} + \frac{\sqrt{a}h}{2}\right)} e^{iu^2}\,du \qquad (3.11)$$

which may be evaluated in terms of the tabulated Fresnel integrals.[31]

It is also possible to give an exact expression for the on-axis transfer function when the array is truncated normally. One way is to use the transform, equation (2.8), of the on-axis impulse response, which in turn may be calculated from the recipe provided by Pace and Ceen.[13] The impulse response is given by

$$i(0,0,z > L,t)/\gamma$$

$$= 2\pi L \quad \text{when} \quad z \leqslant ct \leqslant \sqrt{R^2 + z^2},$$

$$= \frac{\pi R^2}{ct+z} - \pi(ct + z - 2L) \text{ when } \sqrt{z^2 + R^2} \leqslant ct \leqslant \sqrt{(2-L)^2 + R^2} + L , \tag{3.12}$$

$$= 0 \quad \text{when} \quad ct < z \quad \text{or} \quad ct > L + \sqrt{(2-L)^2 + R^2} .$$

Putting

$$r_1 = \sqrt{R^2 + z^2} \quad \text{and} \quad r_2 = \sqrt{R^2 + (z-L)^2} + L$$

it may be shown that

$$\left(\frac{1}{\gamma}\right)\sqrt{\frac{2}{\pi}}\, I(0,0,z > L,\omega) = R^2 e^{-ikz}[Ci(k(r_2-z)) - Ci(k(r_1-z))$$

$$- isi(k(r_2-z)) + isi(k(r_1-z))] \tag{3.13}$$

$$+ \frac{2iLc}{\omega} e^{-ikz} + ce^{-ikr_1}\left[\frac{2iL}{\omega} + \frac{ir_1}{\omega} + \frac{c}{\omega^2} + \frac{i(z-L)}{\omega}\right]$$

$$- ce^{-ikr_2}\left[\frac{ir_2}{\omega} + \frac{c}{\omega^2} + \frac{i(z-L)}{\omega}\right] ,$$

where si(x) and Ci(x) are the tabulated sine and cosine integrals.[31] This is not the only way of deriving this formula. The untruncated version has been given by Berktay *et al.*[51]

The truncated array in sediment

The field in the sediment is found by substituting the plane wave spectrum, equation (3.6), into the inverse transform, equation (2.16). Introducing the new variables θ and ϕ *via*

$$k_x = k\sin\theta\cos\phi ,$$

$$k_y = k\cos\theta\sin\phi \tag{3.14}$$

and hence

$$k_z = k\cos\theta ,$$

we find

$$I_s(x,y,d,\omega) = \frac{-k\gamma}{\sqrt{2\pi}} \int_0^{\pi/2+i\infty} T(\theta)\sin\theta d\theta \int_0^{2\pi} D(\theta,\phi,\omega)d\phi \tag{3.15}$$

$$e^{-ik(\sin\theta(x\cos\phi+y\sin\phi) + L\cos\theta + d(n^2-\sin^2\theta)^{\frac{1}{2}})}$$

$$\cdot$$

$$[\frac{RJ_1(k_rR)}{k_r} - \frac{RJ_1(k_sR)}{k_s} e^{-ik(L/\cos\alpha - L\cos\theta - L\tan\alpha\sin\theta\cos\phi)}] ,$$

with $Im(n) < 0$.

The problem of finding an asymtotic solution to equation (3.15) is similar to that for a point source above a fluid fluid boundary, which has been discussed by a number of authors.[27,33] The solution of equation (3.15) by a stationary phase integration over ϕ followed by a steepest descent integration over θ has, however, a number of additional complications. $D(\theta,\phi,\omega)$ has poles in the ϕ and θ planes which must be accounted for. The two aperture terms $J_1(k_rR)/k_r$ and $J_1(k_sR)/k_s$ should be slowly varying in comparison with the exponential and have, in addition, radicals in their arguments. Finally, the truncation aperture lies at the interface and so has no term in $\cos\theta$ in the phase of its exponential. In appendix A it is demonstrated that the singularities of the integrand may be ignored in the asymtotic solution of equation (3.15). The problem of the truncation phase is discussed, together with a wider description of the steepest descent contour, in appendix B. The restriction on the apertures leads to limitations discussed later.

With the notation

$$\Phi = x\cos\phi + y\sin\phi ,$$

$$\Phi_s = (x - L\tan\alpha)\cos\phi + y\sin\phi , \tag{3.16}$$

$$\Theta = \Phi\sin\theta + L\cos\theta + d(n^2 - \sin^2\theta)^{\frac{1}{2}}$$

and

$$\Theta_s = \Phi_s\sin\theta + d(n^2 - \sin^2\theta)^{\frac{1}{2}} ,$$

the result of the stationary phase integration of equation (3.15), equation (A.6), is

$$I_s(x,y,d,\omega) \sim e^{-i\pi/4}\gamma k^{\frac{1}{2}} \int_{-\pi/2-i\infty}^{\pi/2+i\infty} T(\theta)\sin^{\frac{1}{2}}\theta d\theta \cdot \tag{3.17}$$

$$\left[\frac{D(\theta,\phi_0)}{(\Phi''(\phi_0))^{\frac{1}{2}}} \frac{RJ_1(k_r(\theta,\phi_0)R)}{(k_r(\theta,\phi_0)} e^{-ik\Theta(\theta,\phi_0)} \right.$$

$$\left. - \frac{D(\theta,\phi_1)}{(\Phi''(\phi_1))^{\frac{1}{2}}} \frac{RJ_1(k_s(\theta,\phi_1)R)}{k_s(\theta,\phi_1)} e^{-ikL/\cos\alpha - ik\Theta_s(\theta,\phi_1)} \right]$$

where

$$\Phi'(\phi_0) = 0 , \tag{3.18}$$

i.e.,

$$\tan\phi_0 = y/x \tag{3.19}$$

and

$$\Phi_s'(\phi_1) = 0 . \tag{3.20}$$

From equation (A10) the result of the steepest descent integration of equation (3.17) is

$$I_s(x,y,d,\omega) \sim$$

$$- i\gamma(2\pi)^{\frac{1}{2}}T(\theta_0)\left[\frac{\sin\theta_0}{\Phi''(\phi_0)\,\Theta''(\phi_0,\theta_0)} \right]^{\frac{1}{2}} \frac{RJ_1(k_r(\phi_0,\theta_0)R)}{k_r(\phi_0,\theta_0)} D(\theta_0,\phi_0)e^{-ik\Theta(\theta_0,\phi_0)} \tag{3.21}$$

$$+i\gamma(2\pi)^{\frac{1}{2}}T(\theta_1)\left[\frac{\sin\theta_1}{\Phi_s''(\phi_1)\Theta''(\phi_1,\theta_1)}\right]^{\frac{1}{2}}\frac{RJ_1(k_s(\phi_1,\theta_1)R)}{k_s(\phi_1,\theta_1)}D(\theta_1,\phi_1)e^{-ik[L/\cos\alpha+\Theta_s(\theta_1,\phi_1)]}\,.$$

Here

$$\Theta'(\theta_0) = 0\,, \tag{3.22}$$

i.e.,

$$\Phi(\phi_0)\cos\theta_0 + L\sin\theta - \frac{d\sin\theta_0\cos\theta_0}{(n^2-\sin^2\theta_0)^{\frac{1}{2}}} = 0 \tag{3.23}$$

and

$$\Theta_s'(\theta_1) = 0 \tag{3.24}$$

When the values θ_0 and ϕ_0 correspond to directions close to the array axis ($\phi = 0$, $\theta = \alpha$), equation (3.21) becomes singular. In this case the alternative form for $I(k_x,k_y,\omega)$, equation (3.8), is used in equation (3.15) and results in

$$I(x,y,d,\omega) \sim$$

$$(2\pi)^{\frac{1}{2}}R^2\gamma T(\theta_2)\left[\frac{\sin\theta_2}{\phi_m''(\phi_2)\Theta_m''(\phi_2,\theta_2)}\right]^{\frac{1}{2}}D(\theta_2,\phi_2)\,.$$

$$1e^{-ik(L/2\cos\alpha\,+\,\Theta_m(\phi_2,\theta_2))}\,.\,\sin(L/2\cos\alpha D(\theta_2,\phi_2)^2\,, \tag{3.25}$$

where

$$\phi_m = (x - (L/2)\tan\alpha)\cos\phi + y\sin\phi \tag{3.26}$$

and

$$\Theta_m = \phi_m\sin\theta + (L/2)\cos\theta + d(n^2-\sin^2\theta)^{\frac{1}{2}}\,,$$

with

$$\phi_m'(\phi_2) = 0 \tag{3.27}$$

and

$$\Theta_m'(\phi_2,\theta_2) = 0$$

Provided $\sin\theta < n$ and θ is not too close to θ_c, the square bracket terms in equations (3.21) and (3.25) may be regarded as 'spherical spreading' terms. For example,

$$\left[\frac{\sin\theta_1}{\Phi''_s(\phi_1)\Theta''_s(\phi_1,\theta_1)}\right]^{\frac{1}{2}} \sim \frac{n}{r_t} \qquad (3.28)$$

where r_t is the path length from the truncation to the field point. As θ approaches θ_c, however, all three terms tend to zero.

The two solutions, equations (3.21) and (3.25), are subject to the following restrictions:

$$kr >> 1 \ , \qquad (3.29)$$

where r is any path length from within the volume V to the field point, in order that higher order terms of the asymtotic expansion may be ignored;

$$kd > 1 \ , \qquad (3.30)$$

prevents the field point getting too close to the interface where $T(\theta)$ varies rapidly in the vicinity of θ_0; the previously mentioned requirement that the aperture terms be slowly varying in comparison with the phase leads, with equations (3.28) and (3.29), to the estimate that

$$r_t > \pi R^2 \tan^2\alpha/\lambda \ , \qquad (3.31)$$

when using equation (3.21), putting the field point in the farfield of the truncation aperture, and

$$r_m < L/\cos\alpha \ , \qquad (3.32)$$

when using equation (3.25), putting the field point in the farfield of the array. [Interestingly, equation (3.32) is independent of frequency, a

feature of line arrays previously noted by Berktay and Shooter.[34]]

The three pairs of angles (θ_0,ϕ_0), (θ_1,ϕ_1) and (θ_2,ϕ_2) correspond to the raypaths shown in Figure 3. In addition to these angles, equations (3.22), (3.24) and (3.27) have an additional set of solutions for some $\theta > \theta_c$. These have been discussed by (among others) Gerjouy[33] and Brekhovskikh,[27] and correspond to the evanescent arrival in the sediment. The raypath associated with the evanescent arrival from the transducer is shown in Figure 3, marked θ_e, ϕ_e.

The problem of finding the solutions to equations (3.22), (3.24) and (3.27) is a numerical one; the details are left to appendix B. As shown there, a close numerical examination of the behaviour of the steepest descent contour confirmed Gerjoy's[33] suspicion that the evanescent arrival need only be included when

$$\mathrm{Re}[\Theta(\theta_0)] \lesssim \mathrm{Re}[\Theta(\theta_e)] \quad . \tag{3.33}$$

Not only is (3.33) easy to check once the stationary points have been found, it also has a simple physical explanation. This can be seen by noting that if

$$a(t) = \frac{1}{\sqrt{2\pi}} \int_{-\infty}^{+\infty} F(\omega) e^{-ik\mathrm{Im}[\Theta(\theta)]} e^{i\omega t} d\omega \tag{3.34}$$

then

$$\frac{1}{\sqrt{2\pi}} \int_{-\infty}^{+\infty} F(\omega) e^{-ik\Theta(\theta)} e^{i\omega t} d\omega = a(t) * \delta(t - \mathrm{Re}(\Theta)/c) \tag{3.35}$$

so equation (3.33) requires the arrival time of the evanescent wave to be equal to or greater than the Snell's law arrival time before it need be included in the asymtotic solution to equation (3.15).

Note added in explanation:

The angle θ_i is not a real angle. It only exists as the incident counterpart to the transmission angle $\arccos(n^2-\sin^2\theta)^{1/2}$ shown in Fig 3.

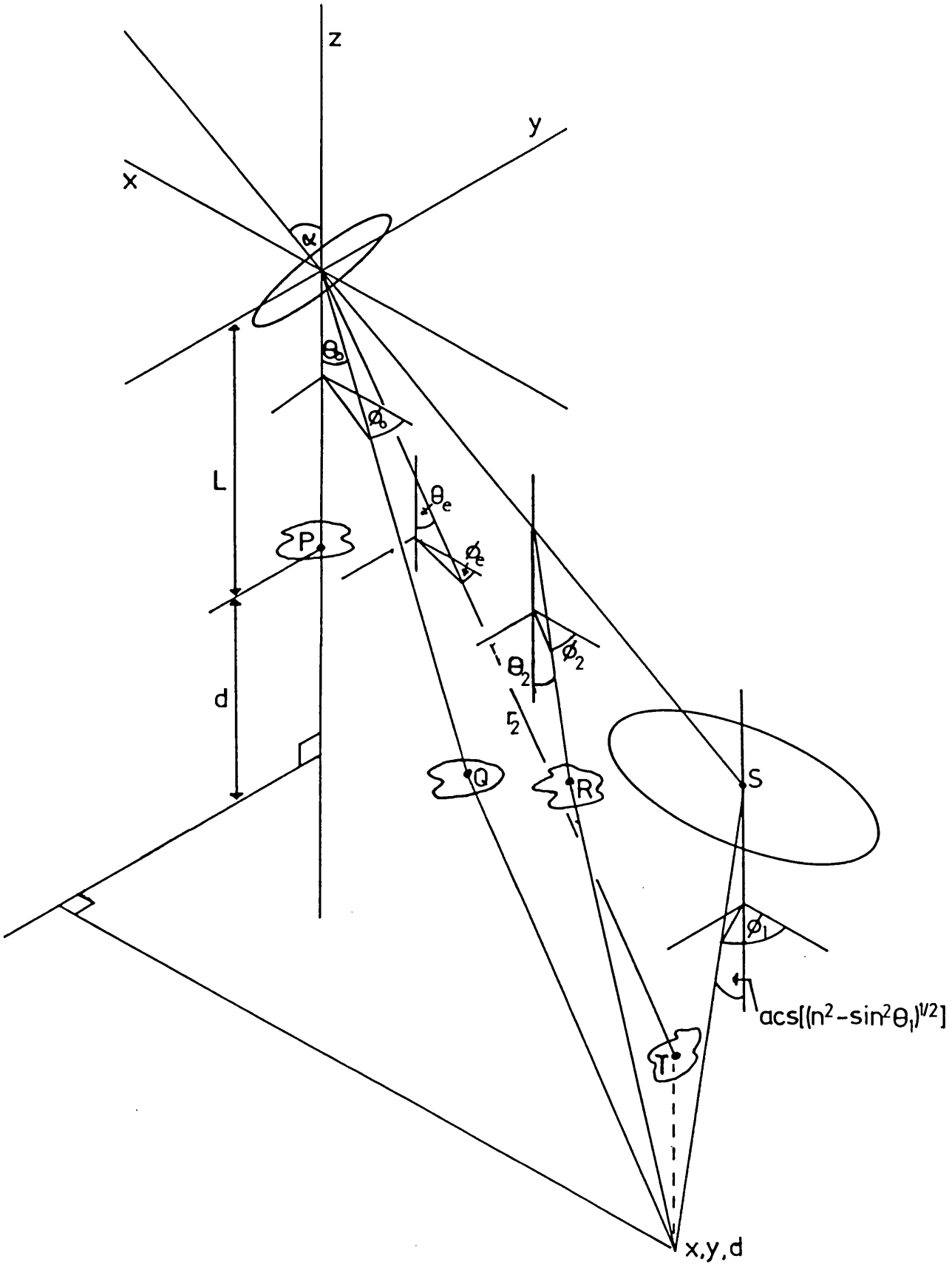

Figure 3. The geometric raypaths into the sediment from a nearfield truncated array. θ_0, ϕ_0: Snell's law arrival from the transducer; θ_1, ϕ_1: Snell's law arrival from the truncation; θ_2, ϕ_2: Snell's law arrival from the middle of the array; θ_e, ϕ_e: evanescent arrival from the truncation. The points P, Q, R, S and T lie in the plane of the interface.

Horton[7] has shown that the ray (θ_e,ϕ_e) may be appreciably displaced (*i.e.*, suffer a discontinuous horizontal shift at the interface), if Im(n) is large and ω sufficiently small. This is achieved (theoretically) by including the phase of $T(\theta)$ in the exponent of (3.15). This amounts to the selective inclusion of second order terms in the asymtotic expansion of (3.15); to do this consistently requires the remaining terms to be included. To the level of approximation implied by equation (3.29) these terms are small and so any displacement is ignored in this study.

Getting in close: the high angle, high frequency nearfield

Useful as they are, equations (3.21) and (3.25) are limited to the farfield and it is natural to ask what analytic progress can be made as the field point approaches the truncation. This problem is a more complicated version of the more familiar piston radiator problem, which, as we have noted, is itself unsolved. Moreover, the one approximation which has led to some progress,[35] that the piston is many wavelengths across, is unlikely to be a useful one for a parametric beam.

To see what can be done the truncation aperture term is first made to look like a piston problem. Substituting the second term of equation (3.5) into (2.15), changing the order of integration, integrating asymtotically over k_x and k_y, and substituting $w = L\tan\alpha+u/\cos\alpha$, the truncation aperture may be written

$$I_S^{trunc}(x,y,d,\omega) \sim \frac{\gamma n}{(2\pi)^{\frac{1}{2}}} e^{-ikL/\cos\alpha} \cdot$$

(3.36)

$$\int_{-R}^{R} \int_{-\sqrt{R^2+y^2}/\cos\alpha}^{\sqrt{R^2+y^2}/\cos\alpha} D(w,y',\omega)T(w,y')\frac{e^{-ik'[(x-w)^2+(y-y')^2+d^2]^{\frac{1}{2}}+(w/n)\sin\alpha}}{r_t(y',w)} dy'dw ,$$

where $k' = \omega/c_s$. This integral is seen to be the field from an amplitude and phase shaded elliptical piston, provided $r_t(w,y')$, which like $T(w,y')$ and $D(w,y')$ is an implicit function of w and y' by virtue of equations (3.30) and (3.24), may be approximated by

$$r_t^2 \simeq (x-w)^2 + (y-y')^2 + d^2 \quad . \tag{3.37}$$

This approximation is just equation (3.28), and so is subject to the same constraints. It should also be noted that equation (3.36) ignores the evanescent arrival, so is unlikely to work close to the interface. [Tjotta and Tjotta[9] have used a similar integral for their study of conventional beam penetration, based on the Helmholz integral. That integral is generally valid, of course, provided the boundary conditions are dealt with properly. The Tjotta's approximation to it, however, is subject to the same constraints as equation (3.36). This should be borne in mind when interpreting their results.]

If $\alpha > \theta_c$, then $D(w,y')$ is well behaved throughout the region of integration, because there is no ray for which θ_1 can be $> \theta_c$, and the poles of D lie at $\theta_1 = \alpha$. Secondly, the phase is nowhere stationary, for $(1/n)\sin\alpha > 1$, so that the non-linear term is not enough to change the gradient of $(w/n)\sin\alpha$. For large k, we can use the following asymtotic expansion, equation D4,

$$\int_a^b \psi(t) e^{i\lambda\phi(t)} dt = \left(\frac{1}{i\lambda}\right)\left[\frac{e^{i\lambda\phi(t)}}{\phi(t)}\right]_a^b + O\left(\frac{1}{\lambda^2}\right) \tag{3.38}$$

provided $\phi'(t) \neq 0$ on a,b.

Identifying $\phi(t)$ with $[(x-w)^2 + (y-y')^2 + d^2]^{\frac{1}{2}} + (w/n)\sin\alpha$, and applying (3.38):

$$I_s^{trunc}(x,y,d,\omega) \sim \frac{i\gamma n}{R(2\pi)^{\frac{1}{2}}} e^{-ikL/\cos\alpha} .$$

$$\int_{-R}^{R} \left[\frac{D(w,y')T(w,y')e^{-ik'r_t(w,y')-(w/n)\sin\alpha}}{r_t[(x-w)/r_t + m]} \right]_{\frac{-\sqrt{R^2+y^3}}{\cos\alpha}}^{\frac{\sqrt{R^2+y^2}}{\cos\alpha}} dy' . \qquad (3.39)$$

This can be recognised as an integral around the 'rim' of the ellipse. In addition, the phase is stationary over y' and so the straightforward stationary phase approximation can be used.

Putting $y' = R\sin\phi$, the phase of equation (3.39) is

$$\Phi = [(x - \frac{R\cos\phi}{\cos\alpha})^2 + ((y - R\sin\phi)^2 + d^2)^{\frac{1}{2}} + m\tan\alpha R\cos\phi] \qquad (3.40)$$

and the stationary points are given by

$$\Phi' = \pm \frac{(x \pm \frac{R\cos\phi}{\cos\alpha})}{r_t} \frac{R\sin\phi}{\cos\alpha} - \frac{(y - R\sin\phi)R\cos\phi}{r_t} \pm m\tan\alpha R\sin\phi = 0 \qquad (3.41)$$

Equation (3.41) is polynomial in $\sin^8\phi$, and algebraically it is far from clear that equation (3.41) has real roots. The stationary phase method usually has a geometrical interpretation: if equation (3.41) has real roots they will correspond to a particular raypath.

Consider first the case when $\alpha = 0$. Then equation (3.39) describes a circular aperture and equation (3.41) becomes

$$\frac{(x \pm R\cos\phi)}{r_t} R\sin\phi - \frac{(y - R\sin\phi)}{r_t} R\cos\phi = 0 \qquad (3.42)$$

Suppose $\underline{a}$ is the position vector of the point on the edge of the aperture from which the geometric raypath leaves. $\underline{a}$ lies in the plane of the aperture and so has no vertical component:

$$\underline{a} = R\cos\phi\, \underline{i} + R\sin\phi\, \underline{j} \qquad (3.43)$$

The vector $\underline{r}_t = r_t^x \underline{i} + r_t^y \underline{j} + r_t^z \underline{k}$ describing the raypath is

$$(x - R\cos\phi)\underline{i} + (y - R\sin\phi)\underline{j} + d\underline{k} \qquad (3.44)$$

so equation (3.42) is a statement to the effect that

$$\underline{a} \wedge (r_t^x \underline{i} + r_t^y \underline{j}) = 0 \quad , \qquad (3.45)$$

i.e., the projection of $\underline{r}_t$ in the plane of the transducer is colinear with $\underline{a}$. Figure 4(a) shows this interpretation.

At angles of incidence away from normal equation (3.41) may still be considered a homogeneous equation of the sort equation (3.45). Because the aperture is now elliptical, $\underline{a}$ is replaced by $\underline{e}$ where

$$\underline{e} = \frac{R\cos\phi}{\cos\alpha}\, \underline{i} + R\sin\phi\, \underline{j} \qquad (3.46)$$

and equation 3.41 may be written

$$\left(\frac{e_y}{\cos\alpha}\, \underline{i} + e_x \cos\alpha \underline{j}\right) \wedge \left[\left(\frac{r_t^x}{|\underline{r}_t|} + m\sin\alpha\right)\underline{i} + \frac{r_t^y}{|\underline{r}_t|}\underline{j}\right] = 0 \qquad (3.47)$$

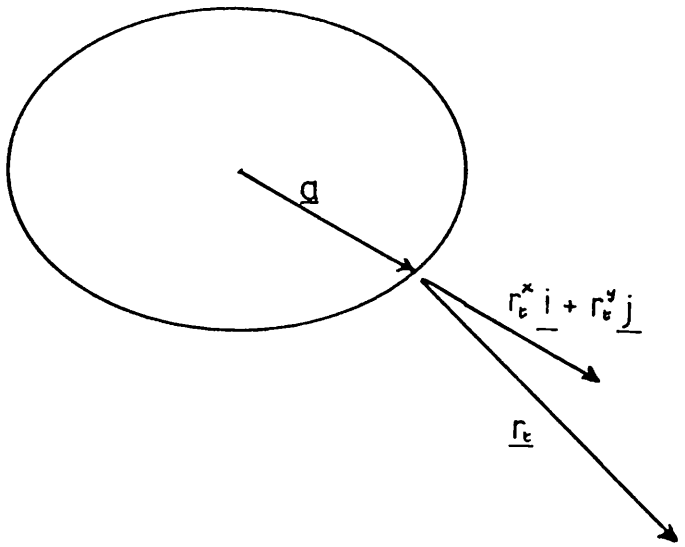

Figure 4(a) Geometric interpretation of the stationary phase equation from a circular aperture. The vectors $\underline{a}$ and $r_t^x \underline{i} + r_t^y \underline{j}$ are co-linear.

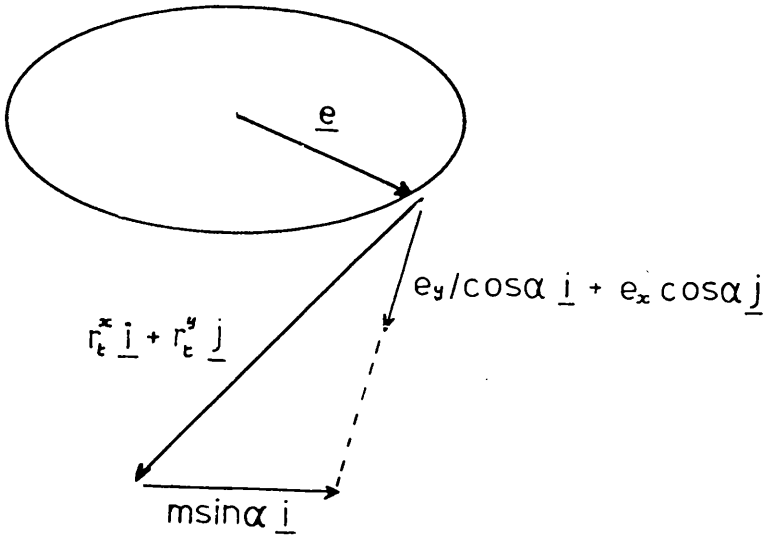

Figure 4(b) Geometric interpretation of the stationary phase equation from an elliptical phase shaded aperture. The equation selects a ray closer to the major axis than in the circular case.

Equation (3.46) says that, in general, $\underline{e}$ and $r_x\underline{i} + r_y\underline{j}$ are no longer co-linear. The ellipticity and phase shading of the aperture result in a raypath closer to the major axis of the ellipse than is the case with a circular aperture. Figure 4(b) shows this interpretation. That equation (3.47) has such a solution is seen when it is realised that taking the raypath around the edge of the ellipse takes $\underline{e}$ through 360°, but $r_t^x\underline{i} + r_t^y\underline{j}$ considerably less. At some point (two, actually), equation (3.47) is satisfied.

The result of integrating equation (3.39) by stationary phase is thus

$$I_s^{trunc}(x,y,d,\omega)$$

$$\sim \pm i \frac{e^{\pm i\pi/4}\gamma_n}{k'^{3/2}} \frac{T(\pm)D(\pm)}{r_t(\pm)} \frac{e^{ikr_t(\pm)\mp m\sin\alpha R\cos\phi}}{\Phi''_t(\pm)[(x \pm R\sec\alpha)^2 + m\sin\alpha]} , \qquad (3.48)$$

the ± signs indicating arrivals from either edge. It is possible to show, with some algebra, that as r_t becomes large, equation (3.48) is the first term of the expansion of the truncation term of equation (3.21) for large k_s with the Bessel function replaced with Hankel functions:

$$2J_1(z) = H^{(1)}{}_1(z) + H^{(2)}{}_1(z) . \qquad (3.49)$$

Discussion of the asymtotic solutions to the nearfield truncation with numerical examples

To examine the beaviour of the solutions, equations (3.21) and (3.25) were used to calculate the secondary pressure in the sediment. Numerical values for the constants were chosen to allow comparison of the theoretical predictions with the experimental measurements: R = 0.02 m, L = 0.2 m,

$C = 1500$ m s^{-1}, $\omega = 2\pi \times 10^5$ s^{-1}, $\rho = 10^3$ kg m^{-3}, $\rho_s = 1.8 \times 10^3$ kg m^{-3}, $n = 0.866 - 0.007i$ [hence $Re(\theta_c) = 60°$] and the source function [equation (2.5)] was taken to be a unity amplitude cosine wave at 100 kHz.

Figure 5 shows the secondary pressure contours in the plane $y = 0$ with a subcritical primary beam incidence angle of 50°. At subcritical values of α, α can equal θ_2 and equation (3.25) is used to determine the pressure in the main beam. For a fixed value of α, this expression behaves similarly to a conventional beam. The maximum pressure occurs along the Snell's law angle of transmission associated with α (*i.e.*, 62°) and the evanescent arrival is too small to influence the contours. The slight asymmetry of the beam is due to the 'spherical spreading' term. This asymmetry is obvious in the beam cross-section of Figure 6, which is the pressure in the plane $x = 0.5$ m. The contours are compressed as the field point approaches the interface. The beam width, on the other hand, is hardly changed by the presence of the interface.

At a fixed location in the sediment, however, the maximum pressure does not occur when the array is aligned with the Snell's law path from the transducer to that point. Figure 7 shows the pressure at $x = 0.75$ m, $y = 0$ and $d = 0.1$ m as a function of α. The most striking feature is that the peak pressure occurs at an angle $\theta_M = 62°$, which is 5° greater than the Snell's law angle θ_0 and 2° greater than the critical angle θ_c. The cause of this behaviour is twofold. Firstly, as α increases, so too does the array volume. This is implicit in equation (3.25), for as $\theta_2 \to \alpha$, $\sin[kL/2\cos\alpha D(\theta,o)] \to (L\tan\alpha)/2$; *i.e.*, half the array length. Secondly, the centre of the array is also a function of α and becomes closer to the field point as α increases, so that the spherical spreading reduces. This shift of the effective centre of the source volume from

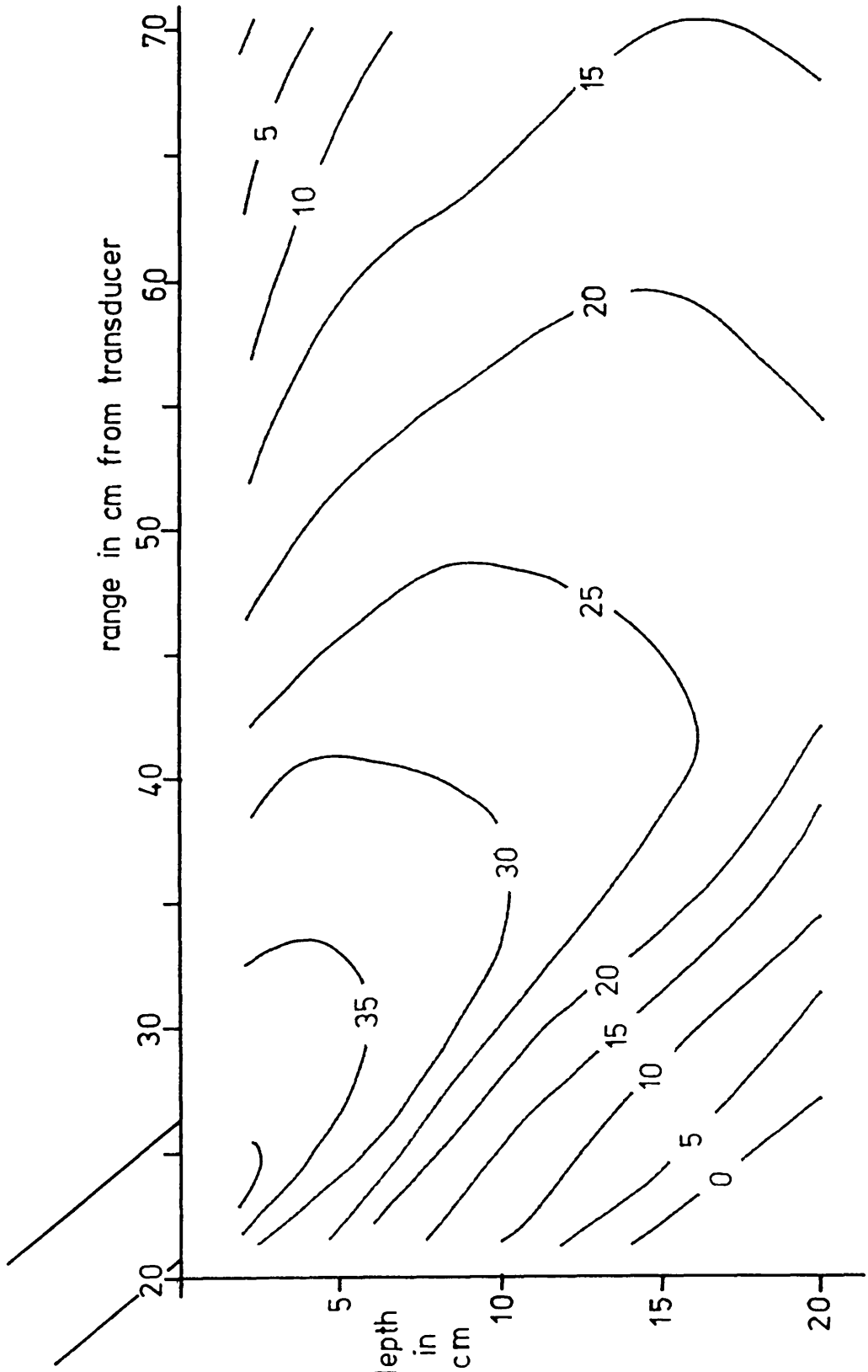

Figure 5 Secondary pressure contours [dB re 10^{-6} Y Pa] in the sediment in the plane of the beam when the array is incident at 50°. The location of the truncation is shown in the top left-hand corner.

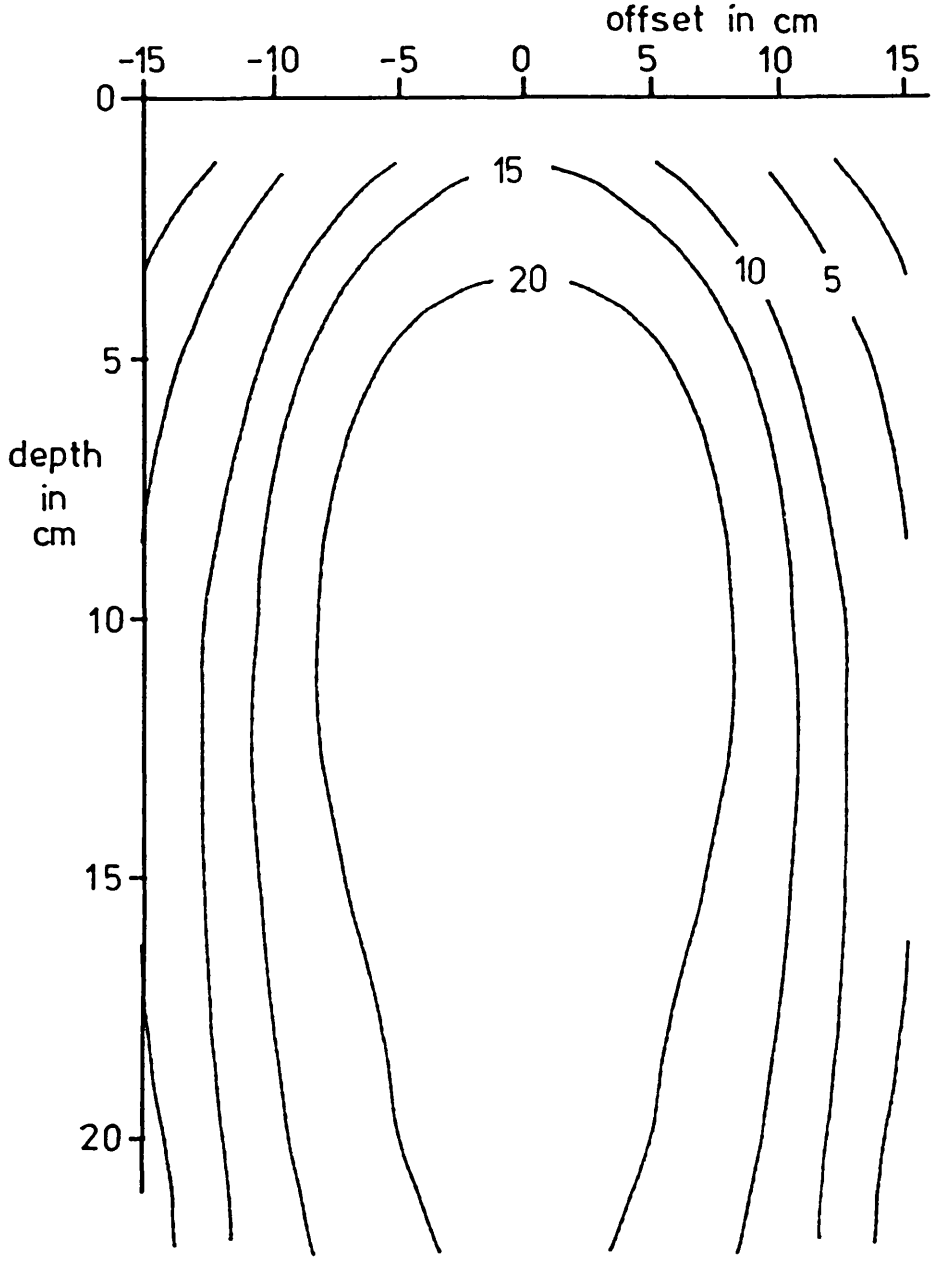

Figure 6. Secondary beam cross-section in the sediment in the plane x = 50 cm, when the array incident angle is 50° [dB re 10^{-6} Y Pa].

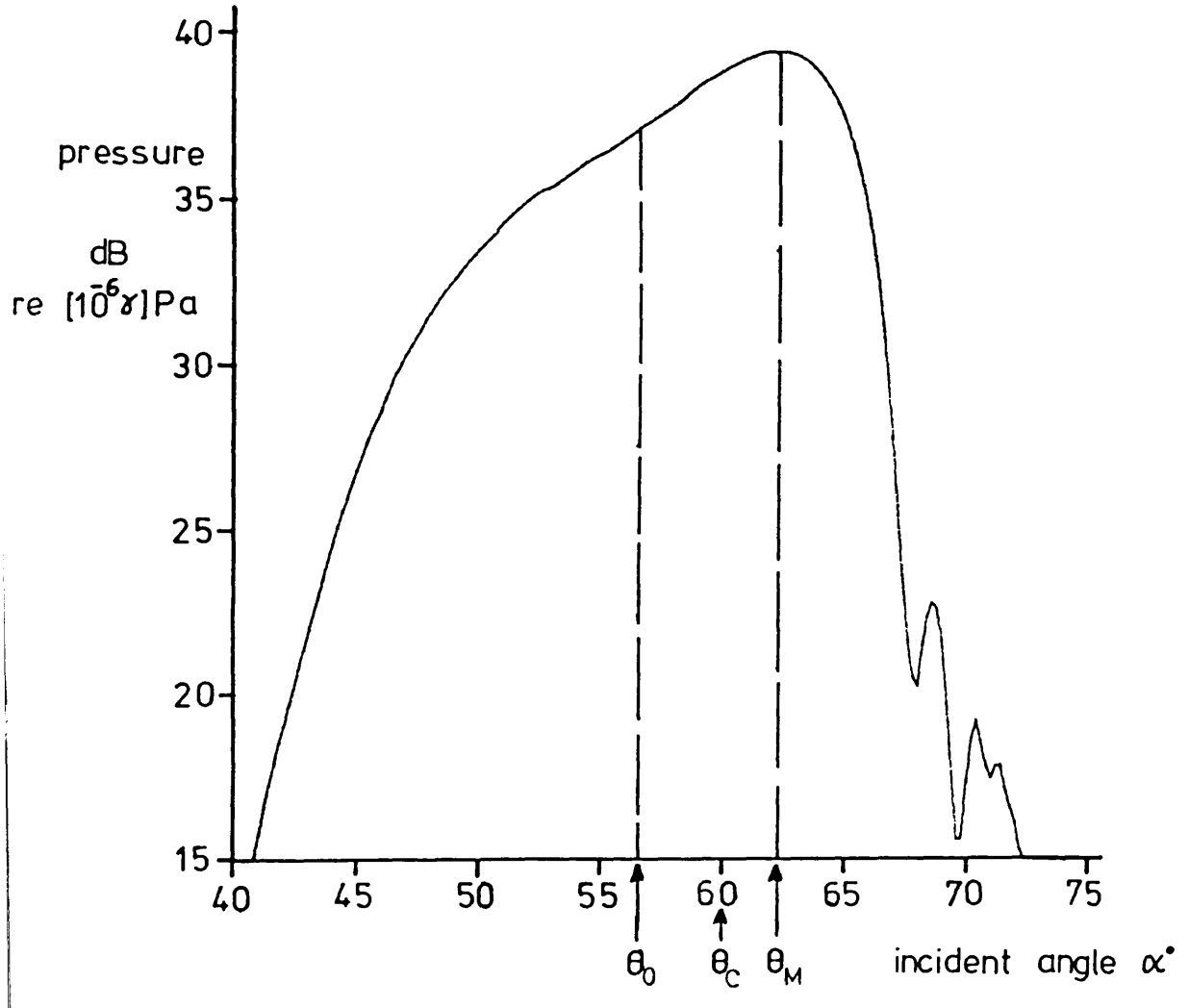

Figure 7 Variation of secondary pressure in the sediment at a fixed location, x = 75 cm, y = 0 and d = 10 cm, as a function of beam incident angle. θ_0: Snell's law angle to the field point from the transducer; θ_c: the critical angle; θ_M: angle of maximum pressure.

the transducer towards the field point is responsible for the essential differences between conventional and parametric beam behaviour through an interface.

As α becomes increasingly postcritical, $\alpha-\theta_2$ increases until the main beam only penetrates the interface at small depths and the field in the sediment is largely determined by the interference of the two apertures of equation (3.21). Figure 8 shows the pressure contours in the plane $y = 0$ with a postcritical primary beam incidence angle of 70°, and their behaviour may be understood in the relative importance of the arrivals from the two apertures.

At very large distances from the array, the spherical spreading is similar for both arrivals and they are of equal importance. As the field point approaches the array, the raypath from the truncation becomes significantly shorter than that from the transducer. In this region, which accounts for most of Figure 8, the importance of the transducer arrival is reduced. Whether the termination aperture is in a position to take advantage of this reduction depends on α.

The directivity of the aperture has its maximum when $\theta_1 = \alpha$ and dies away as $\alpha-\theta_1$ gets larger. If the array incident angle is greater than critical, then the minimum value $\alpha-\theta_1$ may take is $\alpha-\theta_c$, because θ_1 is an 'incident' angle, *i.e.*, $\theta_1 \lesssim \theta_c$. This limitation on θ_1 introduces a marked top/bottom asymmetry at postcritical angles of incidence, which is the main feature of the beam cross-section in Figure 9. The top half of the beam is reflected at the interface. This behaviour also provides a justification for ignoring the reflected primaries in the source volume V. The raypath from such a beam would make such a large angle with its axis that its contribution would be negligible.

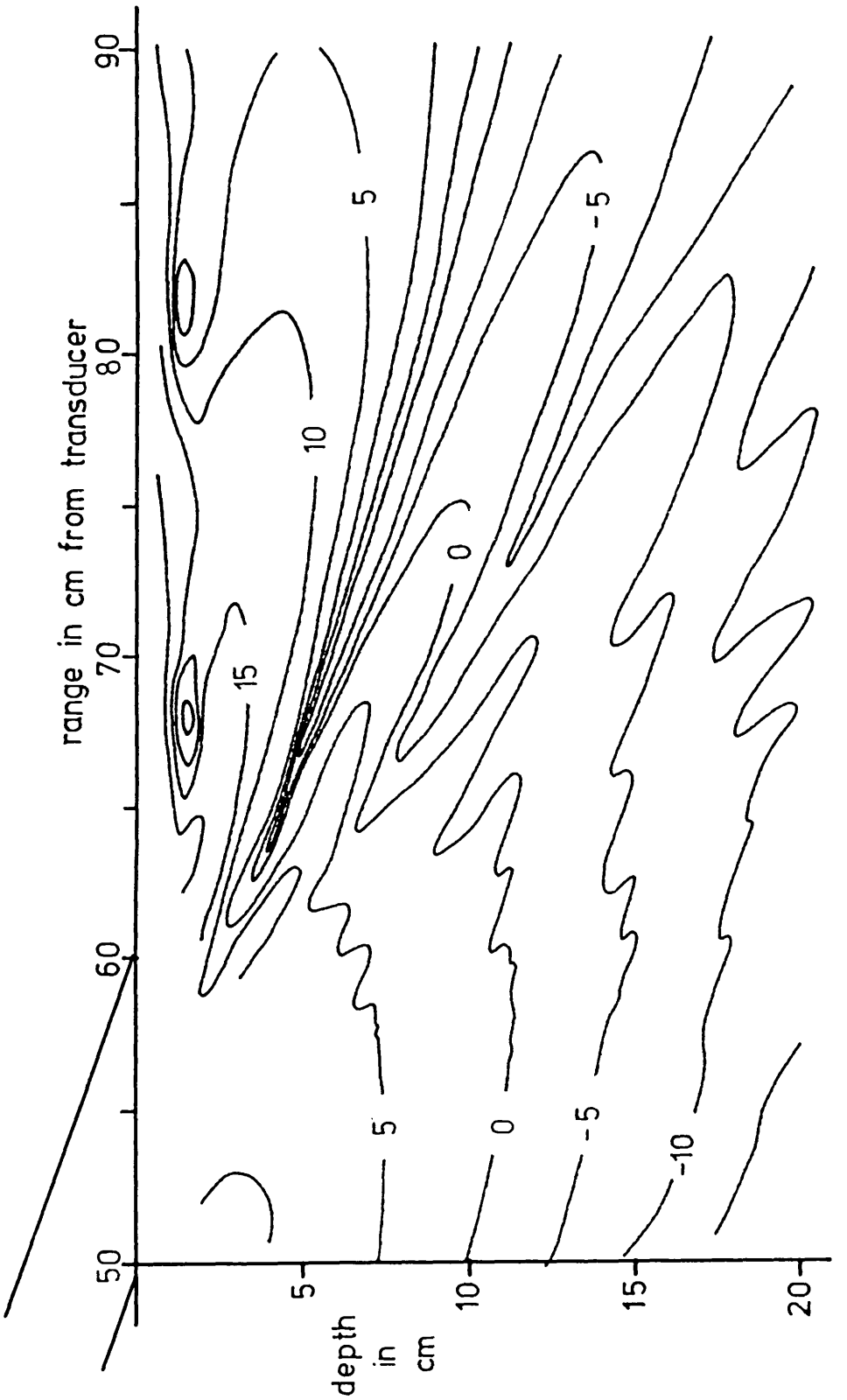

Figure 8 Secondary pressure contours [dB re 10^{-6} Y Pa] in the sediment in the plane of the beam when the array is incident at 70°. The position of the truncation is shown in the top left-hand corner.

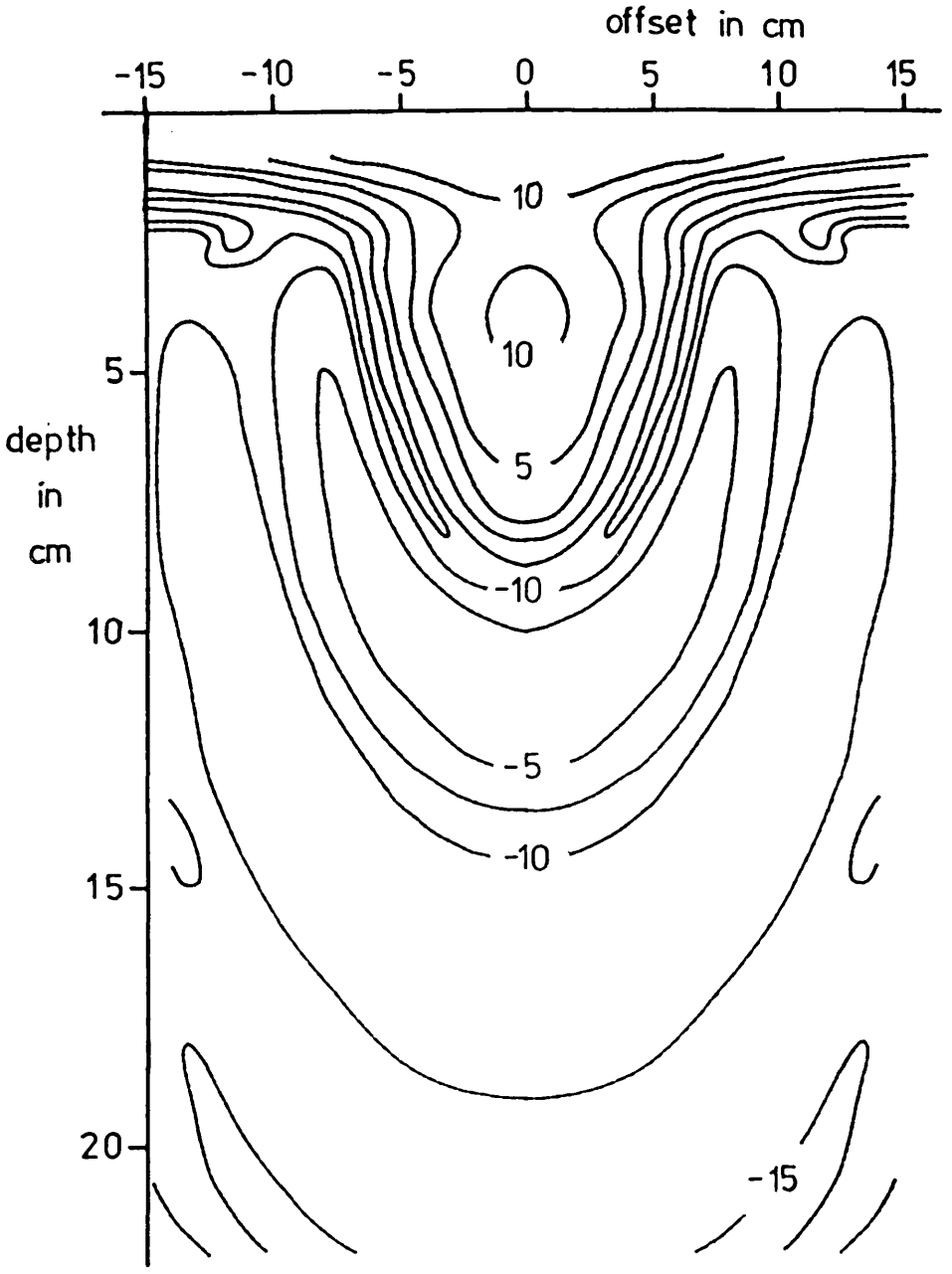

Figure 9 Secondary beam cross-section in the sediment in the plane x = 75 cm when the array is incident at an angle of 70° [dB re 10^{-6} Y Pa].

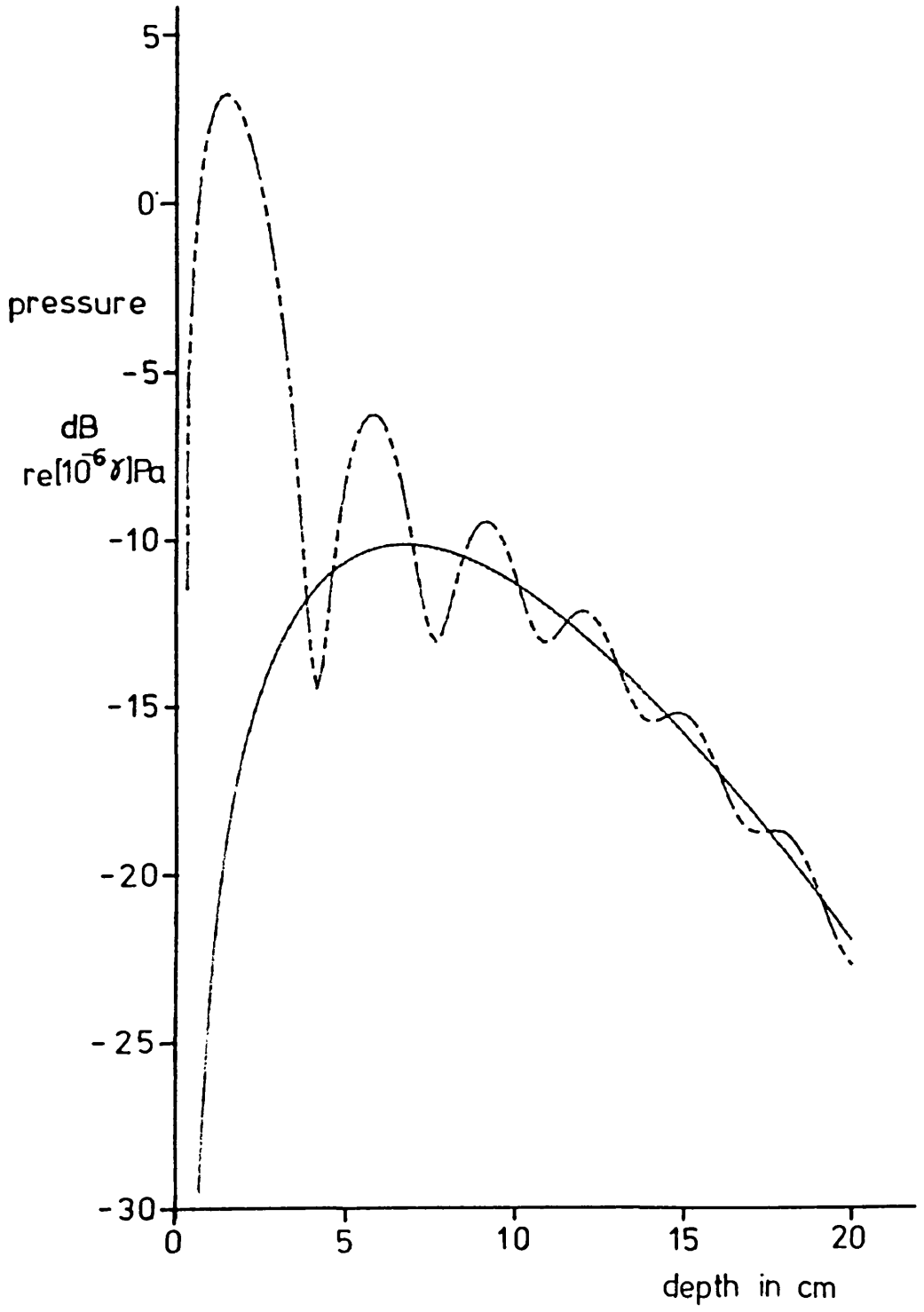

Figure 10 Secondary pressure in the sediment vertically beneath the truncation when the array is well postcritical, $\alpha = 75°$. ——— : transducer arrival only; ------: transducer plus truncation arrival.

In addition, the argument of the Bessel function, k_s, and hence the directivity term $J(k_sR)/k_s$ is asymmetric about $\theta_1 = \alpha$. If $\phi = 0$, then $k_s = k[\sin(\theta_1-\alpha) - \tan\alpha\sin^2(\theta_1-\alpha)]$. If $\alpha > \theta_c$, $\theta_1-\alpha$ is negative and k_s will grow much more rapidly than k_r as the depth increases when α is large.

The effect of increasing α is thus to confine the penetration to an increasingly shallow region beneath the interface; clearly seen in Figure 8, where the importance of the truncation arrival is limited to a fan of angles with its apex at the truncation. This behaviour is emphasised by considering the behaviour of the high angle nearfield, equation (3.48). Figure 10 shows the pressure vertically beneath the truncation when $\alpha = 75°$ as a function of depth. Here, the asymtotic solution to the transducer aperture has been added to equation (3.45) to give the total field, and it is seen that the trucation aperture is merely a high frequency ripple on the more slowly varying transducer term. Only at the smallest depths does the truncation term differ significantly from the transducer term. In this region, however, the assumptions leading to the derivation of the truncation term become questionable, so care must be taken before attaching too much significance to the peak at a depth of 2 cm [see the remarks following equation (3.37)]. The effect of phase is so powerful that the reduced spherical spreading of the truncation arrival is irrelevant at high enough angles of α. [It is a pity, considering the industry put into its derivation, that equation (3.45) turns out only to be useful in this negative sense: if the assumptions behind equation (3.45) are satisfied, the answer will not be of much interest.]

The detailed form of the sidelobe activity seen in Figures 8-10 is a consequence of the simplified form, equations (3.1)-(3.3), used to model the primary beam, which becomes increasingly inadequate as the array length approaches the Rayleigh distance of the primary beam. Tjotta and Tjotta[24] have calculated the departure of the secondary source strength $q(\underline{x}',t)$ from

that used here [equation (3.3)] at several fractions of the Rayleigh distance of the primary beam and show that it becomes increasingly smooth and narrow. It is difficult to assess the consequence acknowledging this behaviour would have on the sidelobes of the two apertures; whilst narrowing the truncation aperture would broaden its directivity, smoothing it would reduce its sidelobes.

Very close to the interface the contours turn horizontal, due to the evanescent arrival. As the field point approaches the surface, there is a narrow region where evanescent arrival, growing rapidly as e^{-kd}, and the Snell's law arrival, dying away as $\theta_1 \rightarrow \theta_c$, are of the same amplitude and interfere with one another, producing very localised maxima and minima. The evanescent arrival is most noticeable as the field point approaches the truncation, *i.e.*, as $\theta_e \rightarrow \alpha$. This localisation is to be expected of the evanescent arrival from a beam which would be greatest where the beam strikes the interface (ignoring any displacement), dying away horizontally due to the beam directivity and vertically due to its evanescent nature.

A consequence of the truncation of the primary beam by the interface is that the parametric beam width in the sediment is a function of α. At subcritical values of , the farfield directivity of the array is, with $\eta = \alpha - \theta_m$, $\sin[kL\sin^2(\eta/2)/4\cos\alpha]/2k\sin^2(\eta/2)$, so that as α increases, the beamwidth narrows. The importance of the interface in determining the beamwidth and signal level in the sediment mean that the performance of the parametric array incident on sediment differs considerably from the same array used in an unbounded medium. Conversely, should the array be so distant from the interface that there are no virtual sources near the interface, the parametric beam performance will be qualtiatively similar to that in an unbounded medium. In such a case the shift of the effective centre of the source

volume would be negligible in comparison with the length of the raypath into the sediment and postcritical penetration would also be negligible. These remarks beg the obvious question: how far away must the array be from the interface for this to occur? To answer this we need to consider the case of farfield truncation, which is the subject of the next chapter.

CHAPTER 4

The Farfield Truncated Array

In this chapter the qualitative features are discussed of the radiated farfield secondary pressure in sediment from a parametric array incident in its primary farfield on the interface.

When the truncation of the array lies in the farfield of the primaries it becomes necessary to split the source volume integral, equation (2.12), into two volumes. The first, v_1, includes the entire nearfield of the primaries which are assumed to halt abruptly at some distance r_0. The second, v_2, encloses the farfield. These are assumed to start abruptly at r_0 and extend out to the truncation. The choice of the distance r_0 is somewhat arbitrary; Zemanek's[36] and the Tjotta's[35] numerical calculations suggest it should be somewhat less than the Rayleigh distance $\pi R^2/\lambda_0$, and here we will take

$$r_0 = R^2/\lambda_0 \quad . \tag{4.1}$$

The geometry of the array is now that shown in Figure 11.

The secondary field resulting from the volume v_1 is given by the straightforward extrapolation of the nearfield truncation results, equation (3.21), allowing that the truncation (of the nearfield) is normal to the array axis and no longer lies in the plane z = L. In fact, as soon as the nearfield is any distance from the farfield truncation, ($> 2r_0$ say), all the raypaths from within v_1 to the field points of interest may be considered parallel; then a single term will suffice for this contribution:

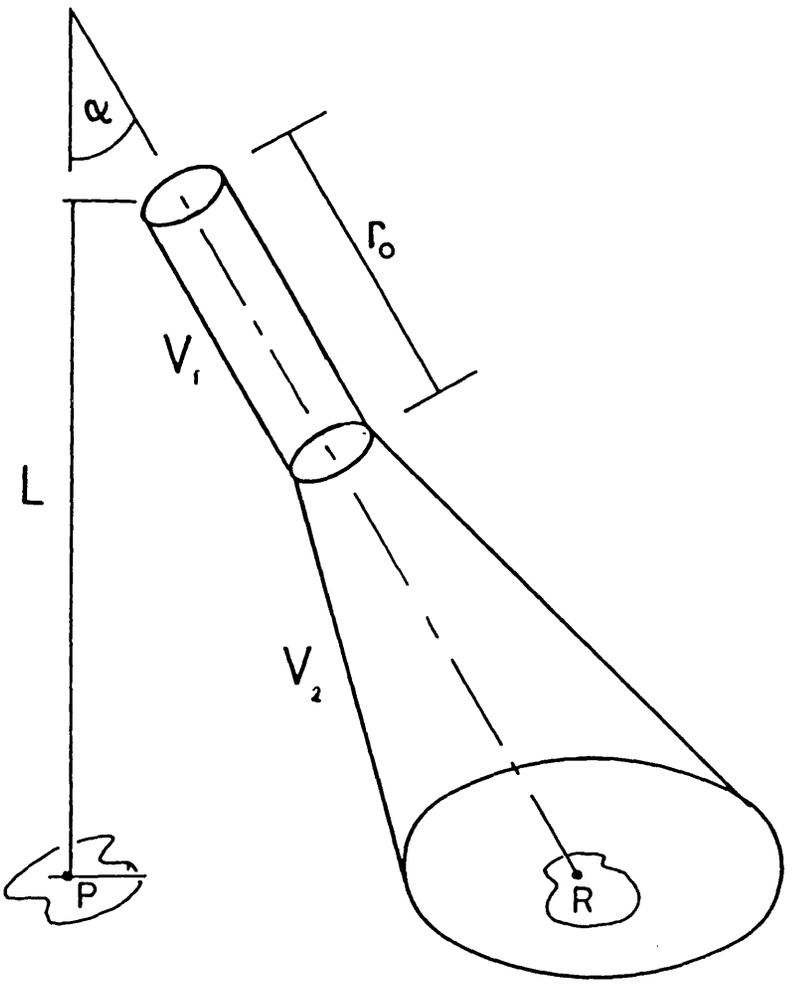

Figure 11 Geometry of the secondary source volume when the array is farfield truncated. V_1 and V_2 contain the nearfield and farfield of the primaries respectively. The points P and R lie in the plane of the interface.

$$I_S^{v_1}(x,y,d,\omega) \sim 2\gamma(2\pi)^{\frac{1}{2}} T(\theta_2) e^{-ik\Theta(\phi_2,\theta_2)}$$

$$\left[\frac{\sin\theta_2}{\Phi''(\phi_2)\Theta''(\theta_2,\phi_2)}\right]^{\frac{1}{2}} \frac{RJ_1[k_r(\phi_2,\theta_2)R]}{k_r(\phi_2,\theta_2)} D(\theta_2,\phi_2) \quad . \tag{4.2}$$

$$\sin[kr_0(1 - \sin\alpha\cos\phi_2\sin\theta_2 - \sin\alpha\cos\theta_2)/2\ ].$$

The first step for the volume v_2 is to calculate its plane wave spectrum from equation (2.12). Noting the comments concerning equation (2.13), equation (2.12) may be written

$$\hat{I}^{v_2}(k_x,k_y,\omega) = \frac{1}{k_z} \int_{v_2} g^2(\underline{x}',\omega_0) e^{-ik|\underline{\zeta}(\underline{x}')| + i\underline{k}.\underline{x}'} d\underline{x}' \quad , \tag{4.3}$$

where $\underline{k}$ is the wavevector. (The geometric interpretation of this formalism breaks down when k_z becomes complex, but this need not concern us.)

Within v_2 the primaries are assumed spherically spreading. They are most easily described by a set of spherical polars, r, η and σ, seen in Figure 12. The wavevector $\underline{k}$ is described by a similar set having the same axis: k, ρ and μ. These are also seen in Figure 12. The interface still lies in the plane z' = L, so that any point in the plane obeys the equation

$$r_p(\eta,\sigma)\cos\alpha_p = L \tag{4.4}$$

The functions $g(\underline{x}',\omega_0)$ and $\underline{\zeta}(\underline{x}')$ are now given by

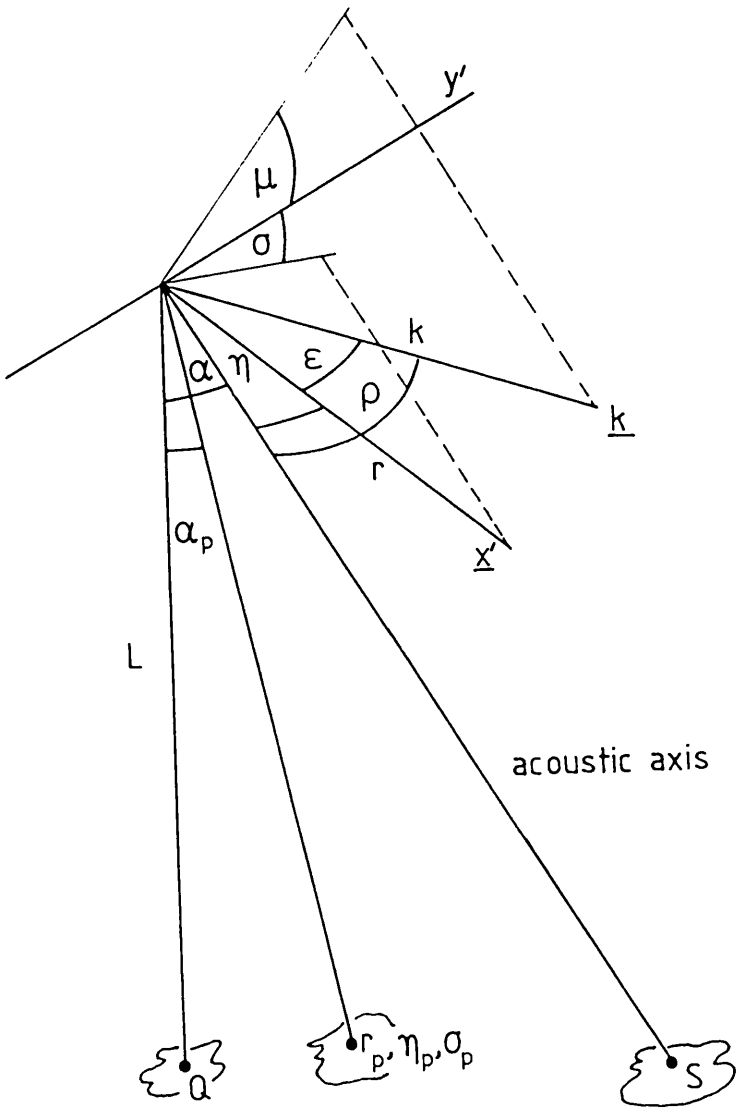

Figure 12 The co-ordinate description of the secondary source volume $\underline{x}'(r, \eta, \sigma)$, and the wavevector $\underline{k}(k, \rho, \mu)$, for the case of spherically spreading primaries. Q, r_p and S lie in the plane of the interface.

$$g(\underline{x}',\omega_0) = \frac{\omega_0 R^2}{2c} \frac{D_0(\eta)e^{-\alpha_0 r}}{r} \tag{4.5}$$

and

$$\underline{\zeta}(\underline{x}') = \underline{x}' \tag{4.6}$$

Defining $g(\underline{x}',\omega_0)$ in this way means that, with $D_0(\eta)$ normalised to unity, $p_m(t)$ entering in equation (2.7) is still the average nearfield pressure.

Substituting equations (4.5) and (4.6) into (4.3) gives

$$\hat{I}^{v_2}(k_x,k_y,\omega) = \frac{\omega_0 R^2}{2ck_z} \int_0^{2\pi}\int_0^{\pi}\int_{r_0}^{r_p(\eta,\sigma)} D_0^2(\eta)e^{-2\alpha_0 r - ikr} \cdot e^{ikr[\cos\rho\cos\eta+\sin\rho\sin\eta\cos(\mu-\sigma)]} \sin\eta dr d\eta d\sigma \tag{4.7}$$

The r integral is elementary:

$$\hat{I}(k_x,k_y,\omega) = \frac{\omega_0 R^2}{2ck_z} \int_0^{2\pi}\int_0^{\pi} D_0^2(\eta)\sin\eta d\eta d\sigma \quad . \tag{4.8}$$

$$\left[\frac{-ike^{ikr\{\cos\rho\cos\eta+\sin\rho\sin\eta\cos(\mu-\sigma) - (1-2i\alpha_0/k)\}}}{[\cos\rho\cos\eta + \sin\rho\sin\eta\cos(\mu-\sigma) - (1-2\alpha i/k)]}\right]_{r_0}^{r_p(\eta,\sigma)}$$

Just as in the nearfield case, there are two contributions from each end of the volume. The term corresponding to the lower limit, denoted ${}^{r_0}\hat{I}^{v_2}$, is

$$r_0\hat{I}^{v_2}(k_x,k_y,\omega) =$$

$$\frac{i\omega_0 R^2 k}{2ck_z}\int_0^{2\pi}\int_0^{\pi}\frac{D_0^2(\eta)\,e^{ikr_0[\cos\varepsilon(\eta,\sigma)\,-\,1\,+\,2i\alpha_0/k]}\sin\eta d\eta d\sigma}{[\cos\varepsilon(\eta,\sigma)\,-\,1\,+\,2i\alpha_0/k]}\quad , \tag{4.9}$$

because $\underline{k}.\underline{x}' = kr[\cos\rho\cos\eta+\sin\rho\sin\eta\cos(\mu-\sigma)] = kr\cos\varepsilon$ (see Figure 12). Noting that the line corresponding to the length L in Figure 12 has co-ordinates L,α,π we can see that from equation (4.4) and a similar argument in reverse that

$$r_p = L/(\cos\alpha\cos\eta - \sin\alpha\sin\eta\cos\sigma)\quad , \tag{4.10}$$

so that the term corresponding to the upper limit is

$$r_p\hat{I}^{v_2}(k_x,k_y,\omega) =$$

$$-\frac{i\omega_0^2 R^2 k}{2ck_z}\int_0^{2\pi}\int_0^{\pi}\frac{D_0^2(\eta)\,e^{-ikL[\cos\varepsilon(\eta,\sigma)\,-\,1\,+\,2i\alpha_0/k]}}{(\cos\alpha\cos\eta - \sin\alpha\sin\eta\cos\sigma)}\frac{\sin\eta d\eta d\sigma}{[\cos\varepsilon(\eta,\sigma)\,-\,1\,+\,2i\alpha_0/k]} \tag{4.11}$$

Neither of the integrals (4.9) and (4.11) are simple; not surprisingly, I have been unable to integrate them exactly. Considerable progress, in understanding at least, can be made by approximate methods.

The term $r_0\hat{I}^{v_2}$, equation (4.9), can be investigated with methods substanially the same as developed by Moffett and Mellen[19] to calculate the farfield of parametric arrays. This entails enquiring as to the behaviour of $r_0\hat{I}^{v_2}$ when $\underline{k}$ is aligned with the array axis (*i.e.*, $\rho = 0$) and when $\underline{k}$ is

well away from the axis (*i.e.*, ρ is large), and assuming that when $\underline{k}$ lies between these limits nothing 'silly' happens to $r_0 \hat{v}_2$. First note that $D_0(\eta)$ is only substantially non-zero for small η. [This is the implicit assumption of equation (2.3).] At the distance r_0 the phase in (4.9) can thus be simplified with

$$\cos[\varepsilon(\eta,\sigma)] \sim \cos\rho + \eta\cos(\mu-\sigma) \quad , \tag{4.12}$$

so that equation (4.9) becomes

$$r_0 \hat{v}_2 \simeq \frac{i\omega_0 R^2 k}{2ck_z} e^{-ikr_0-2\alpha_0 r} \int_0^{2\pi} \int_0^{\text{small } \eta} \frac{D_0^2(\eta) e^{ikr_0[\cos\rho+\eta\sin\rho\cos(\mu-\sigma)]} \sin\eta d\eta d\sigma}{[\cos\rho+\eta\sin\rho\cos(\mu-\sigma)-1+2i\alpha_0/k]} \tag{4.13}$$

When ρ is large the denominator is slowly varying, so that

$$r_0 \hat{v}_2 \sim \frac{i\omega_0 R^2 k\pi}{ck_z} \frac{e^{-ikr_0-2\alpha_0 r}}{(\cos\rho - 1)} \int_0^{\text{small } \eta} D_0^2(\eta) e^{ikr_0\cos\rho} J_0(kr_0\eta\sin\rho) \cdot \sin\eta d\eta \tag{4.14}$$

When ρ is small the phase can be neglected, so that

$$r_0 \hat{v}_2 \sim \frac{i\omega_0 R^2 k}{2ck_z} e^{-ikr_0-2\alpha_0 r_0} \int_0^{2\pi} \int_0^{\text{small } \eta} \frac{D_0(\eta)\sin\eta d\eta d\sigma}{[\cos\rho-\eta\sin\rho\cos(\mu-\sigma)-1+2i\alpha_0/k]} \tag{4.15}$$

The integral of equation (4.14) is the farfield of an amplitude shaded circular piston; the integral of (4.15) is essentially that of Berktay and

Leahy.[17] The most important (though scarcely surprising) conclusion to be drawn from equations (4.14) and (4.15) is that the integrals contribute little to the phase of ${}^{r_0}\hat{I}^{v_2}$, which is dominated by kr_0. When ${}^{r_0}\hat{I}^{v_2}$ is substituted into equation (2.12), its phase, as we have seen, determines both the location and angular dependance of ${}^{r_0}I_s^{v_2}(x,y,d,\omega)$. The effect of ${}^{r_0}\hat{I}^{v_2}$ is thus of an aperture of unspecified directivity lying at $x = r_0\sin\alpha$, $y = 0$ and $z = r_0\cos\alpha$. It is clear from (4.14) and (4.15), however, that the directivity will be similar to a conventional aperture in that it is a symmetric function of ρ and independant of μ, and has its maximum when $\underline{k}$ coincides with the normal to the aperture.

Turning now to the truncation term, equation (4.11), the first step is to simplify the exponential by assuming that the change in absorption for points on the interface is small and so it may be removed from the integral with a representative value, the obvious choice being $e^{-2\alpha_0 L\tan\alpha}$. A stationary phase evaluation of equation (4.11) is complicated by the pole in the denominator which in the co-ordinates η and σ is difficult to deal with. For this reason the integral is transformed to another pair of polar angles, ε and ψ, whose axis is the direction of the $\underline{k}$ vector. In this system the pole always lies at $\varepsilon = 0$ (*i.e.*, ignoring absorption, when the wavevector $\underline{k}$ and source vector $\underline{x}'$ coincide). Denoting the new co-ordinates of the line L in Figure 12 as ε_0,ψ_0, equation (4.11) becomes

$$
{}^{r_p}\hat{I}^{v_2}(k_x,k_y,\omega) = \frac{-i\omega_0^2R^2ke^{-2\alpha_0 L\tan\alpha}}{2ck_z}
\iint \frac{D_0^2(\varepsilon,\psi)\,e^{\frac{-ikL(1-\cos\varepsilon)}{[\cos\varepsilon\cos\varepsilon_0-\sin\varepsilon\sin\varepsilon_0\cos(\psi_0-\psi)]}}\sin\varepsilon\,d\varepsilon\,d\psi}{(\cos\varepsilon - 1 + 2i\alpha_0/k)} \quad . \qquad (4.16)
$$

Geometrically this transform is straightforward; algebraically is is messy. However, in the stationary phase evaluation of equation (4.16) the only concern is with points near the stationary points of the phase, $(1-\cos\varepsilon)$, and so it is not necessary to enquire too closely into the limits of equation (4.16). Geometrically at least, (see Figure 12), it can be seen that the range of values of ε is small because η is small, and because, in addition, it is noted that the phase is stationary at $\varepsilon = 0$, ε may be restricted to be small so that $\underline{x}'$ lies close to $\underline{k}$, and then equation (4.16) can be integrated to get

$$r_{p\hat{I}^{v_2}}(k_x,k_y,\omega) = \frac{-i\omega_0^2R^2ke^{-2\alpha_0 L\tan\alpha}}{2k_zc} \tag{4.17}$$

$$\int \frac{J_0\left[\frac{kL(1-\cos\varepsilon)\tan\varepsilon\tan\varepsilon_0)}{\cos\varepsilon\cos\varepsilon_0}\right] D_0^2(\varepsilon,o)\, e^{\frac{-ikL(1-\cos\varepsilon)}{\cos\varepsilon\cos\varepsilon_0}} \sin\varepsilon d\varepsilon}{(\cos\varepsilon - 1 + 2i\alpha_0/k)}$$

The phase of the exponential in equation (4.17) has a stationary point at $\varepsilon = 0$, and because of the $\tan\varepsilon$ term in its phase the Bessel function may be assumed slowly varying. The poles in the denominator, however, lie at $\varepsilon_p = \pm\, 2\sqrt{\frac{\alpha_0}{k}}\, e^{i\pi/4}$ and these may be brought arbitrarily close to $\varepsilon = 0$ depending on the value α_0. An asymtotic representation of equation (4.17), for large $kL/\cos\varepsilon_0$, can be found by approximating it with

$$r_{p\hat{I}^{v_2}}(k_x,k_y,\omega) = \frac{-i\omega_0^2R^2ke^{-2\alpha_0 L\tan\alpha}}{2k_zc} D_0^2(o,o) \int_0^{\infty} \frac{\varepsilon e^{\frac{-ikL\varepsilon^2}{\cos\varepsilon_0}} d\varepsilon}{(\varepsilon^2+\varepsilon_p^2)} , \tag{4.18}$$

and, from equation (D.9), we finally get

$$r_{p\hat{I}}{}^{\hat{v}_2}(k_x,k_y,\omega) \simeq \frac{i\omega_0^2 R^2 k e^{-2\alpha_0 L\tan\alpha}}{4k_z c} D_0^2(o,o)\, e^{\frac{-ikL\varepsilon_p^2}{\cos\varepsilon_0}} E_1\left(\frac{-ikL\varepsilon_p^2}{\cos\varepsilon_0}\right) \qquad (4.19)$$

where E_1 is the tabulated exponential integral.[31] [$D_0^2(o,o)$ is taken to refer to $D_0^2(\eta = \rho, \sigma = \mu)$, not $D_0^2(\eta = 0, \sigma = 0)$.] Unlike the previous expressions for $\hat{I}^{\hat{v}_1}$ or $r_0\hat{I}^{\hat{v}_2}$, $r_{p\hat{I}}{}^{\hat{v}_2}$ has no phase term corresponding to a particular location in space, so that when substituted into the inverse transform, the raypath selected by steepest descent is unaffected by $r_{p\hat{I}}{}^{\hat{v}_2}$ and is simply given by equations (3.18) and (3.22): the raypath from the transducer. It will be recalled that in addition to determining the direction of the raypath, equations (3.18) and (3.22) determine the spherical spreading of the arrival. That part of the transfer function provided by the truncation arrival thus has the directivity of the primaries and 1/r spreading from the transducer. In short: it is indistinguishable from a conventional arrival.

Equation (4.19) is a stationary phase approximation and is only good provided the directivity D_0 does not vary too fast in the vicinity of the stationary point. D_0 has a half power angle given by $\lambda_0/\pi R$. If this angle is used as a limiting value for this condition to be satisfied, then

$$\frac{L}{\cos\varepsilon_0} > \left(\frac{\pi R^2}{\lambda_0}\right)\left(\frac{\lambda}{\lambda_0}\right) \quad , \qquad (4.20)$$

i.e., the truncation must be further away than a distance given by the product of the primary Rayleigh distance and the ratio of the primary to secondary frequency.

Discussion of farfield truncation

The main purpose of this chapter is to arrive at the conclusion implicit in equations (4.19) and (4.20): if the truncation lies beyond the

range $\pi R^2\lambda/\lambda_0^2$ the parametric array will behave in a similar fashion to a conventional beam. This is not to say that secondary sources beyond this range do not contribute to the incident secondary field; their contribution is reflected. The limit, equation (4.20), is a familiar one in parametric array theory. Moffet and Mellen[19] have shown that it characterises the distance at which the secondary sources become spherical with a directivity that is a function of angle only. Such a beam has a plane wave spectrum (or farfield) qualitatively similar to a conventional beam and so it is not surprising (in retrospect!) that this limit should also be important in determining the behaviour of a parametric beam incident on an interface.

Rolleigh's[26] theoretical investigation of the nearfield of a parametric source in water has shown that as the range from the transducer increases, so the sources which contribute to the secondary field become increasingly restricted to locations near to the raypath between the transducer and the field point. The same conclusion may be drawn from the stationary phase behaviour of equation (4.17), where, as the range of the truncation increases, so the important range of ε decreases. In the sediment an analogous explanation applies: the sources which contribute to the secondary field become increasingly restricted to locations near to the Snell's law path between the transducer and the field point. This is also why the oblique truncation has no affect on the directivity.

This behaviour is in sharp contrast to that of nearfield truncation, where the truncation arrival is due to virtual sources lying where the primary beam strikes the interface. The difference between the two cases emphasises the importance of phase in determining the farfield, in this case the phase introduced by the spherical spreading of the primaries. As the truncation moves into the farfield of the primaries and the useful secondary sources

become increasingly restricted in direction, so the effective centre of the array will move away from the interface and the post-critical penetration will reduce, until the limit of equation (4.20) is reached, when the parametric array will be indistinguishable from a conventional narrow beam.

CHAPTER 5

The Apparatus, Instrumentation and Sediment

In this and the succeeding chapter a description of the experimental half of the study is given. The experiments and their results are left to Chapter 6; here, the equipment and its specification, arrangement and calibration are described.

Choice of experimental parameters

The aim of the experiments was to investigate the theoretical predictions of the nearfield truncation theory, developed in Chapter 3, by measuring the secondary pressure in sediment due to a parametric array incident in its primary nearfield on the water sediment interface. The choice of various experimental parameters, and in particular, the choice of transmitter, was made to allow direct comparison with the theory, whilst being constrained by the physical limits of the tank and sediment.

The first constraint was size. The maximum useable area of sediment was 1 x 1 m^2, and the maximum usable depth of 0.8 m of sediment. Secondly, the sediment had an absorption of 0.4 dB/λ, upon which rapid truncation of the primary field depended. The theory predicted the secondary nearfield of the array to be within a distance of twice the array length of the transducer [equation (3.32)]. This limited the maximum array length to $\sim$0.7 m, and in order to accommodate incident angles of up to 75°, the height of the transducer above the interface was limited to being $\lesssim$ 0.2 m.

The primary nearfield had to be larger than 0.7 m to ensure nearfield truncation. This could be achieved with either a large aperture or high frequency. The aperture dimension needed to be large enough to influence the secondary directivity, and the primary frequency low enough to avoid

excessive non-linear attenuation. A suitable combination was found to be a 4 cm diameter, 1.85 MHz transducer. This has a Rayleigh distance of 1.61 m, and the primary field would be absorbed in sediment at 5.5 dB/cm (which is 11 dB/cm loss in virtual source strength). The choice of a secondary frequency of 100 kHz met the following requirements: it was sufficiently high for the asymtotic solutions to be valid; it provided a moderate value of kR for the two apertures as desired (∿12 for the transducer aperture); it was sufficiently low enough for the secondary field to be insensitive to the high frequency variation of the primary nearfield, and in particular, to "see" the truncation as sharp; and finally, it was high enough to ensure useably large secondary signal levels (which are proportional to ω^2).

With these choices for the fundamental parameters made, the specification of the receiver, a B & K 8103 miniature hydrophone, and supporting instrumentation was straightforward, the main requirement being a bandwidth of ∿250 kHz centred around 150 kHz, which would be needed when the array was used in the pulse mode.

The tank and gantry

The experiments were all performed in the School of Physics underwater laboratory at the University of Bath. Figure 13 shows a sketch of the experimental arrangement. Within the large underwater tank, 1.5 m x 5 m x 2 m deep, was a second tank, 1.3 m x 1.3 m x 1 m deep, filled to a depth of 1 m with saturated air-free sand. On two rails running the length of the large tank, a gantry was mounted. The gantry comprised two trolleys, one moving the length of the tank, and a second, mounted on the first, running the width of the tank. From this second trolley, *via* a turntable, a vertical shaft dropped into the tank, and at its base was a second, horizontal, shaft. Onto this second shaft the transducer was mounted. This arrangement allowed

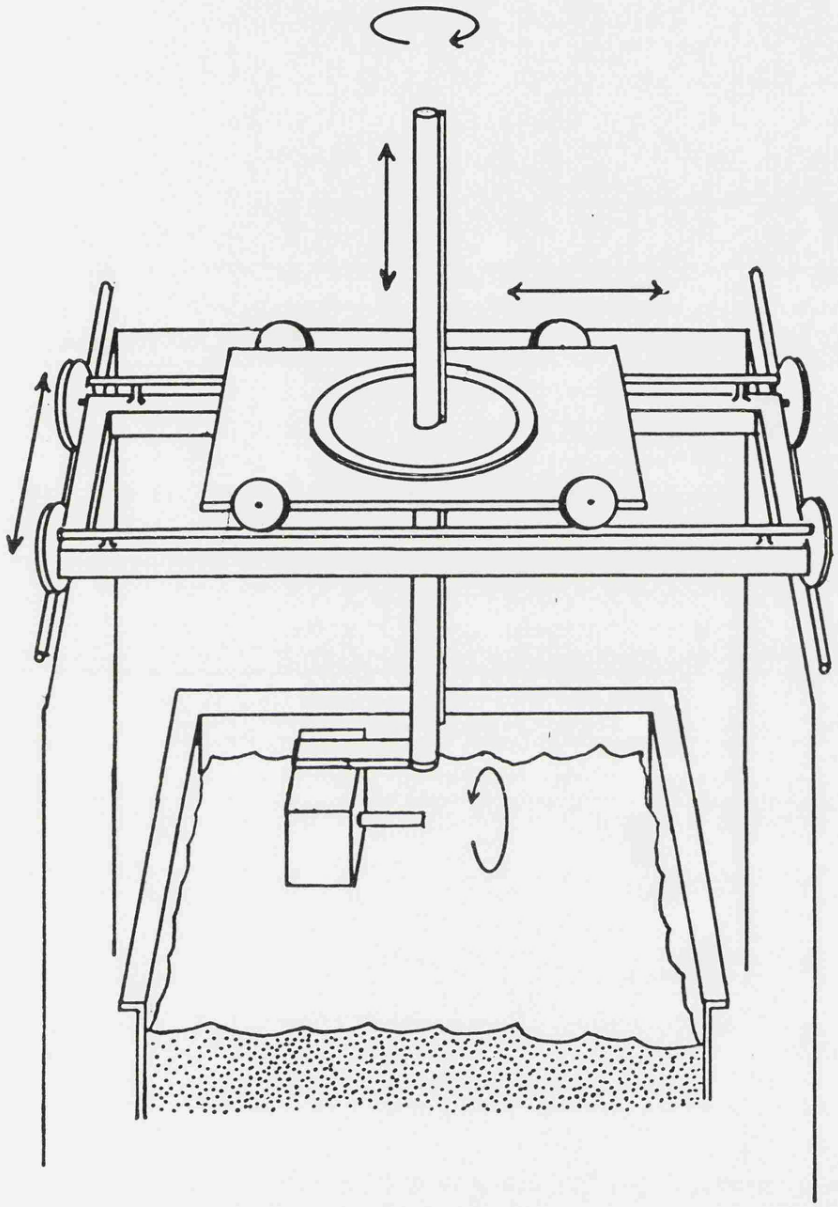

Figure 13 The tanks and gantry arrangement. The transducer is mounted on the horizontal shaft closest to the sediment tank. The five degrees of freedom are indicated by arrows.

the transducer the five degrees of freedom shown in Figure 13, three linear and two axial.

With the exception of the vertical motion, the position and orientation of the transducer was controlled by stepping motors instructed by computer. This allowed measurements to be made at numerous locations swiftly and accurately. The relative linear accuracy of the transducer position was 0.002 m, and the angular accuracy <0.1°. Absolute accuracy was maintained by linear and angular scales attached to the rails and trolleys, or, in the case of the horizontal axis, by a mechanical stop, from which the rotation was measured in stepping motor increments.

The author was fortunate enough to inherit the gantry. Full details of its design and construction may be found in reference 37.

The transmission and reception system

The transmission and reception system used for this study was designed for general purpose experimental acoustics and could supply and record a very wide range of signals varying in shape, length, frequency and power. A box diagram of the arrangement is shown in Figure 14.

The transmission system

The signal source and transducer had to satisfy a number of requirements:

(1) a long enough nearfield to ensure nearfield truncation within the dimensions of the sediment tank;

(2) wide enough bandwidth to allow pulse operation of the parametric array;

(3) a primary frequency low enough that non-linear attenuation of the primaries is negligible at distances less than the truncation distance, but not so low as to overlap the primary and secondary frequency spectra; and

(4) 'good' nearfield behaviour and linearity at the primary frequency.

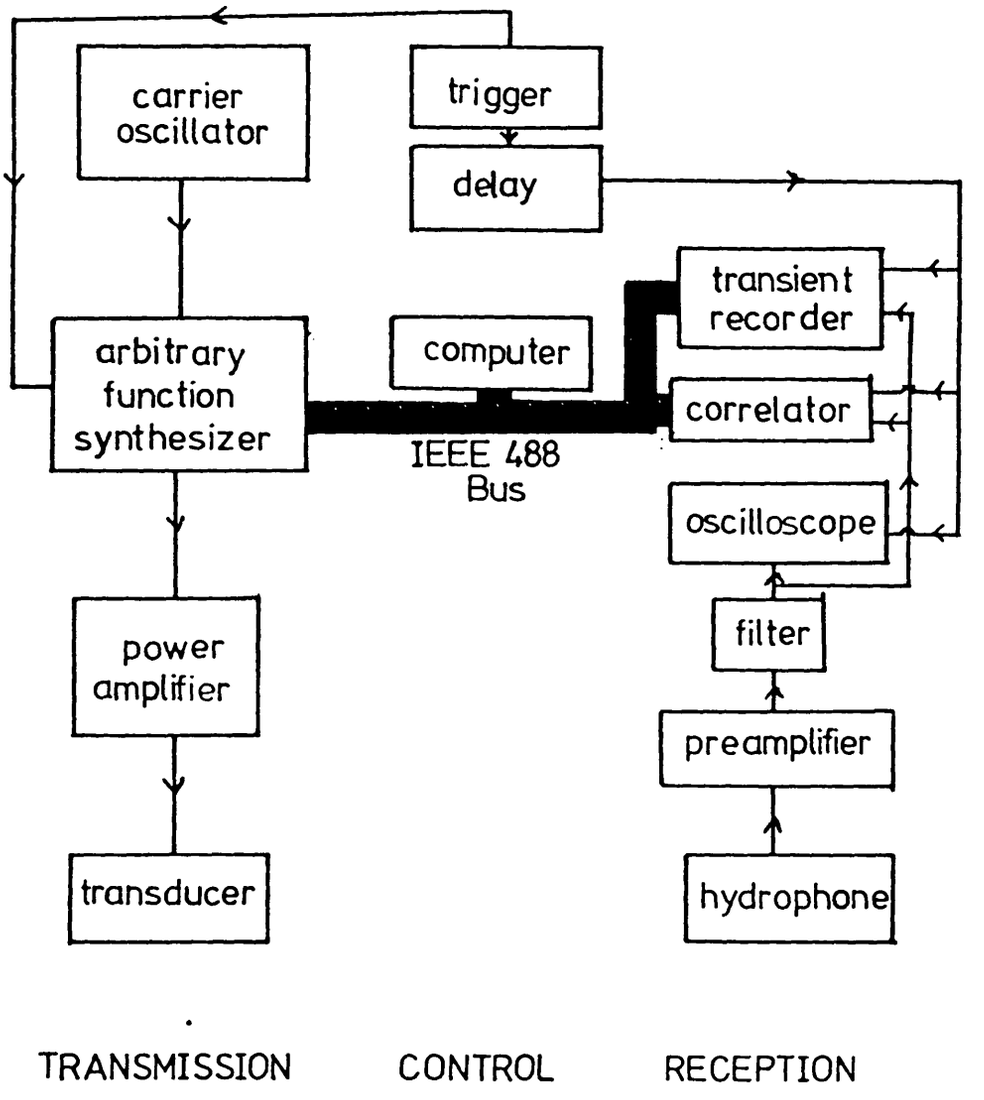

Figure 14 Box diagram of the transmission and reception system.

These criteria were satisfied by the purchase of a very flexible signal source and careful construction of the transducer, and these are described below.

The Signal Source

The Database Arbitrary Function Synthesizer,[38] was designed and built to the author's specification for the purpose of this study. Its function was to generate an analogue voltage waveform from a computer defined digital input which could be output directly to the power amplifier, or, alternatively, used to amplitude modulate a high frequency carrier.

The input waveform was built up from (up to) 2048 8-bit voltage levels spearated in time by (at least) 0.125 μs. In response to an external trigger, the waveform was output from a D/A converter directly to a 50Ω driver or passed first to a modulator with an externally supplied carrier. The combined effect of the A/D converter and drivers also produced a gentle low pass filtering, which removed the steps from the waveform. Figure 15 has a schematic diagram of the synthesizer. The device was interfaced to an I.E.E.E. 488 bus, and limited remote control (triggering, on/off, hold) was possible.

An extremely wide range of signals was available from this source, including FM sweeps, specially shaped pulses, tonebursts or a high frequency carrier modulated with any of these. In this study, two particular forms were used to modulate a 1.85 MHz carrier to the transducer, corresponding to narrowband and wideband use of the parametric array.

In Figure 16 the narrowband modulation, $V_{nb}(t)$, and the wideband modulation, $V_{wb}(t)$, are shown, together with the secondary source waveforms $s_{nb}(t)$ and $s_{wb}(t)$, calculated from equation (2.7), which would result with a very wideband transducer.

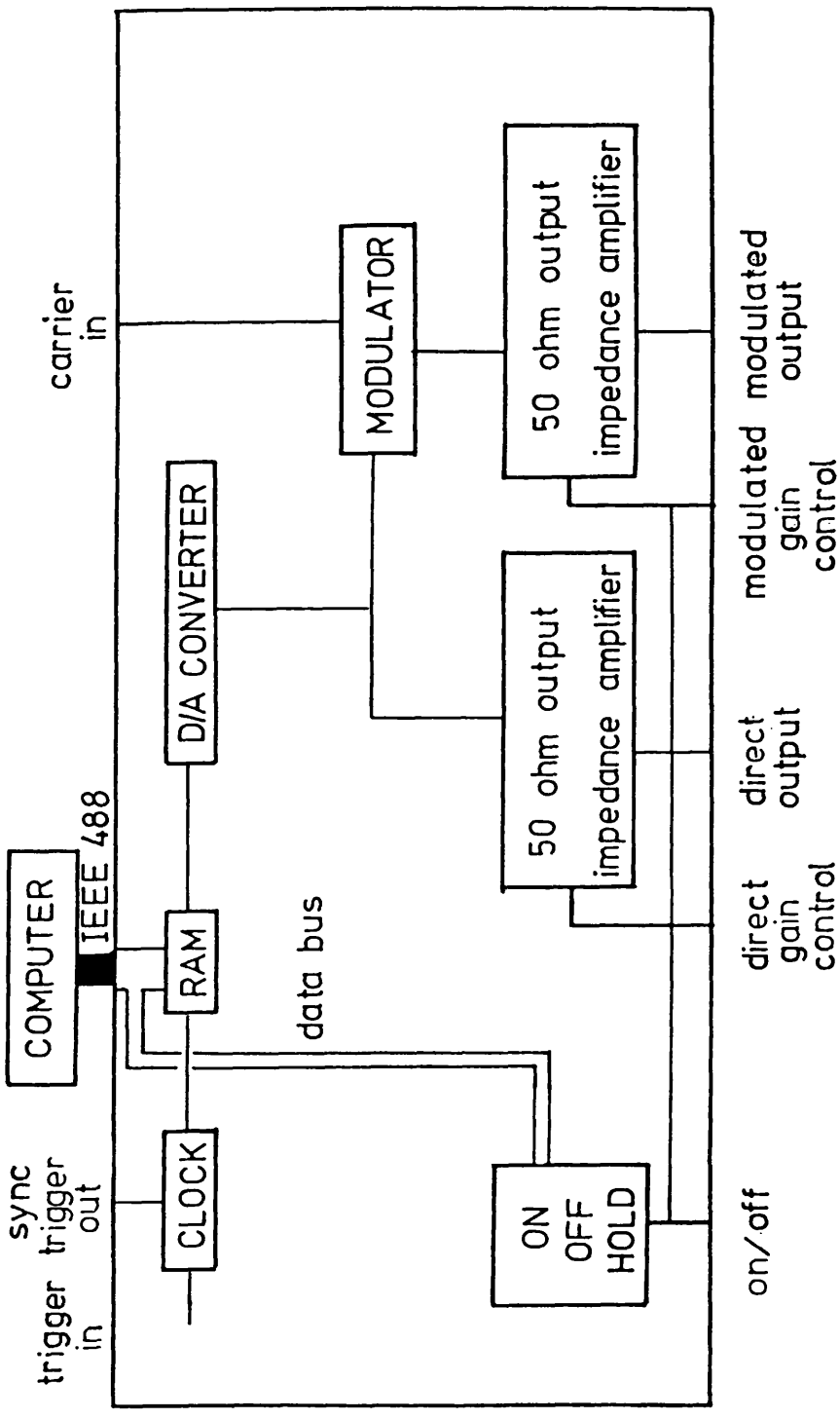

Figure 15 Schematic diagram of the arbitrary function synthesizer.

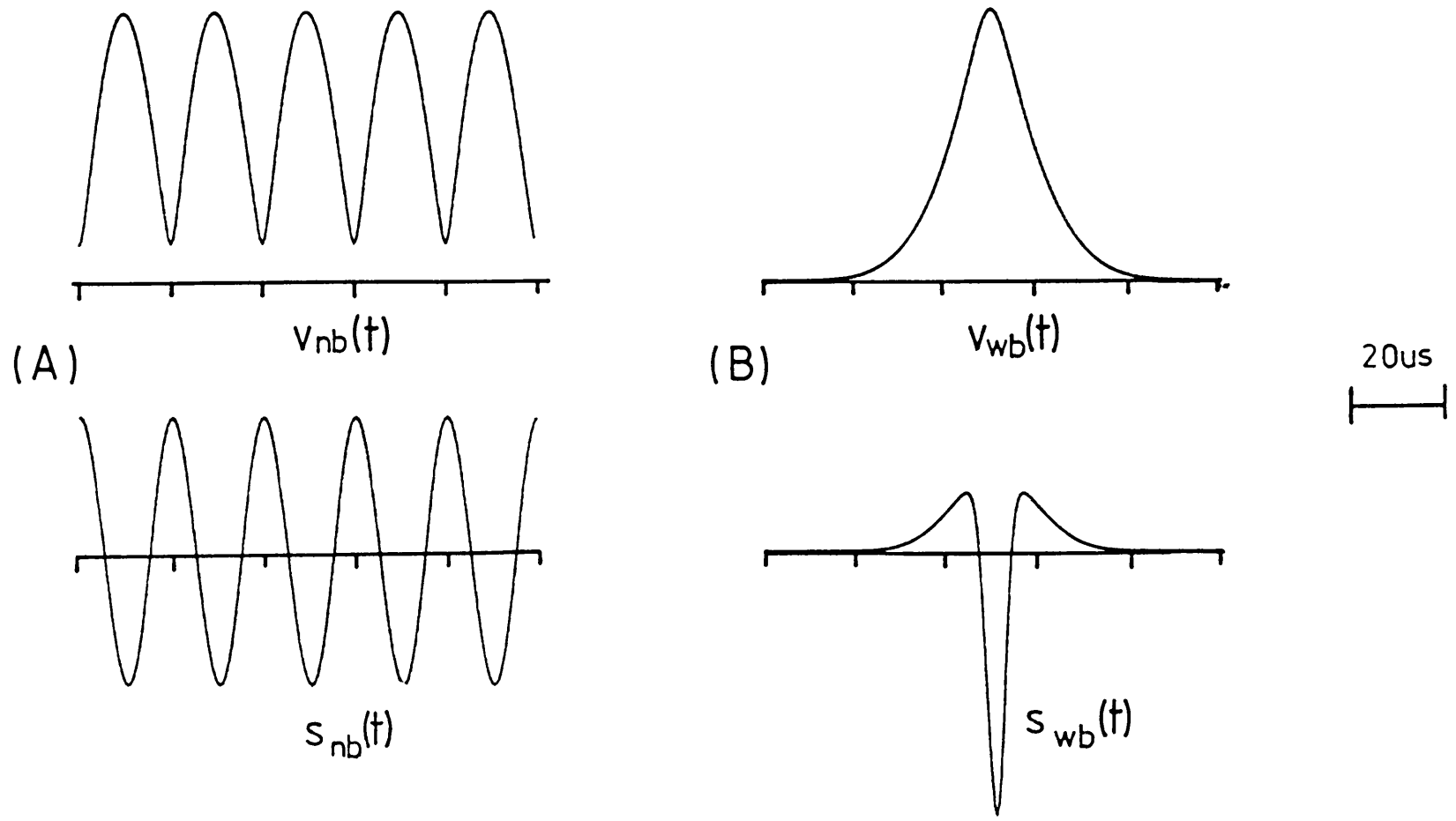

Figure 16 The two primary frequency modulations, $v_{nb}(t)$ and $v_{wb}(t)$, for narrowband and wideband operation respectively, and the corresponding difference frequency source wavelets $s_{nb}(t)$ and $s_{wb}(t)$.

The narrowband modulation, Figure 16(a), was chosen to be

$$v_{nb}(t) = v_0(a + b\cos\omega t)^{\frac{1}{2}} \tag{5.1}$$

[With a = b = 1 the signal supplied to the transducer, $v_{nb}(t)\cos\omega_0 t$ would have been

$$v_{nb}(t)\cos\omega_0 t = \frac{v}{\sqrt{2}}\{\cos[(\omega_0+\frac{\omega}{2})t] + \cos[(\omega_0-\frac{\omega}{2})t]\} \tag{5.2}$$

which is the usual theoretical description of the signal supplied to a narrowband parametric array.]

The modulator circuits were not capable of producing the full depth of modulation implied by equation (5.2). For this reason, the constants a and b were chosen to be a = 1.02 and b = 0.98, which produces the modulation shown in Figure 16.

The wideband modulation shown in Figure 16 is given by:

$$v_{wb}(t) = v_0\{\frac{e^{-2n_1^2t^2}}{n_1} - \frac{e^{-2n_2^2t^2}}{n_2} + t\sqrt{2\pi}[\mathrm{erf}(\sqrt{2}n_1t) - \mathrm{erf}(\sqrt{2}n_2t)]\}^{\frac{1}{2}} \tag{5.3}$$

This complicated looking function has the useful property that as $n_1 \to 0$ and $n_2 \to \infty$, the secondary source function $s_{wb}(t)$ tends to a delta function, as is shown in Appendix D. In practice, the values of n_1 and n_2 are limited by the bandwidth of the transducer. Within these limits, n_1 and n_2 provide convenient control over the bandwidth of the secondary spectrum. From equation (D.13), this spectrum is

$$s_{wb}(\omega) = 4v_0\sqrt{\pi}/2(e^{-\omega^2/8n_1^2} - e^{-\omega^2/8n_2^2}) \tag{5.4}$$

so the difference $n_2 - n_1$ determines the secondary signal bandwidth. For applications in the sediment, $n_1 = 5 \times 10^5$ Hz and $n_2 = 2 \times 10^5$ Hz.

The power amplifier

Whichever of the two modulations were used, the output from the function synthesizer was passed to a 200 W, 50 dB fixed gain E.N.I. power amplifier. This amplifier has a transfer function flat to within 2 dB over the frequency range 10 kHz to 12 MHz, *i.e.*, more than sufficient for the present purpose, and its output circuitry is sophisticated enough to be insensitive to load impedance.

The transducer

The transducer design combined simplicity of construction with a wide bandwidth and long nearfield. The principles of construction were those followed by Kossoff:[41] the P.Z.T. element was provided with a low impedance backing and a quarter wavelength plate on the front to improve the bandwidth. The backing material was a mixture of epoxy resin and 400 μ ∅ glass spheres. This composite has a low acoustic impedance and a high absorption (1.5×10^6 Rayls, > 45 dB/cm at 2 MHz[42]). A 2.5 cm depth of epoxy-glass mixture was poured into a 4 cm length of 8 cm diameter plastic pipe (plastic drainpipe, in fact), and allowed to set hard. A (nominally) 2 MHz, 4 cm diameter P.Z.T.4 disc was cut into four sectors to prevent low frequency flexing and set into the machined surface of hard epoxy-glass at one end of the pipe. This end of the pipe was then sealed with epoxy resin and the upper surface machined down (with great care, to avoid removing the wiring contacts to the disc), to a quarter wavelength thickness. Mounted onto the back of the pipe and immersed in epoxy resin was a matching transformer with the primary and secondary coils adjusted to remove the static capacitance and tune the input impedance to 40 Ω. Figure 17 shows the details of its construction.

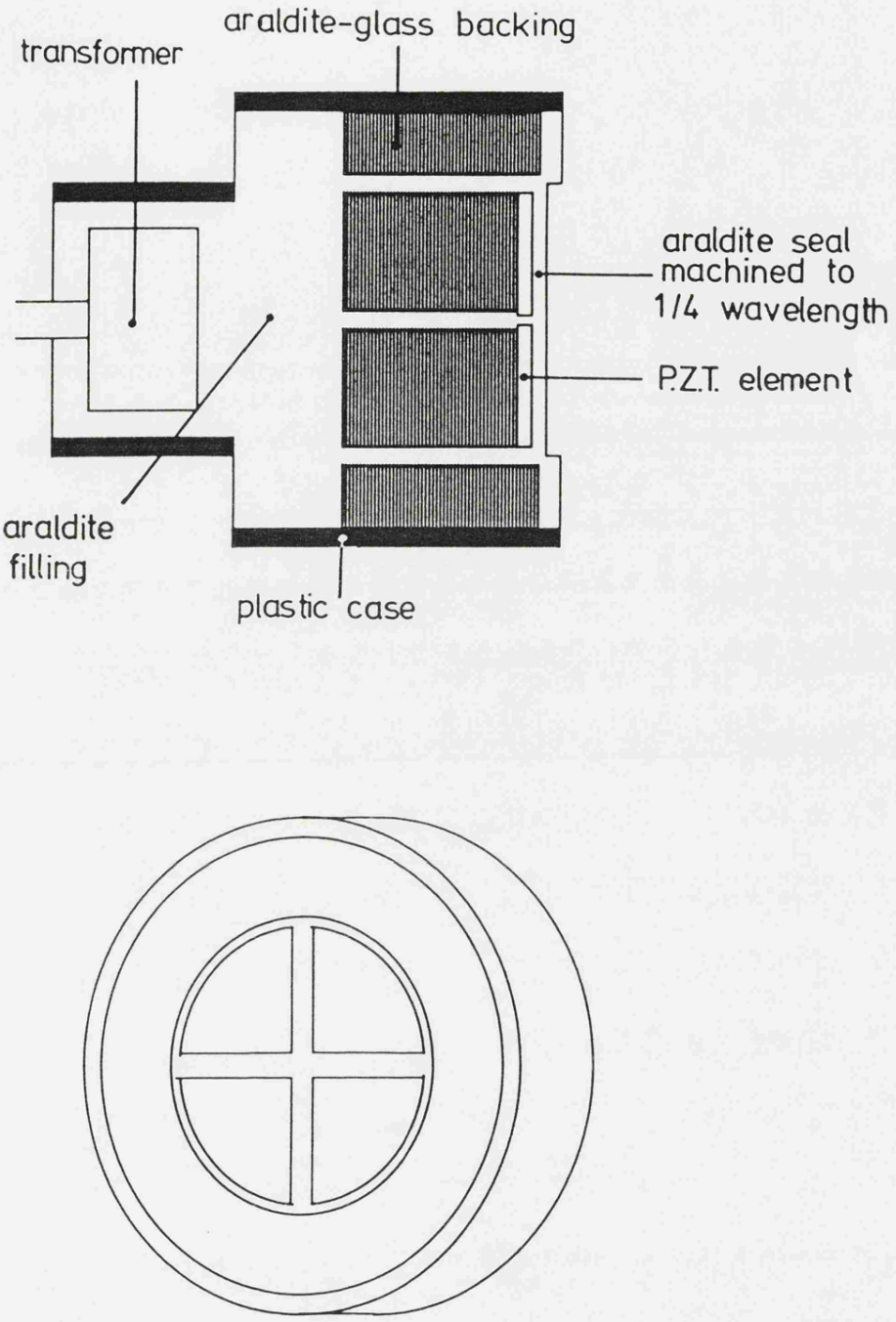

Figure 17 Details of the transducer construction and schematic view of its front face. The wires are not shown for clarity.

The primary field

The primary field calibration of the transducer was done using the plane wave self-reciprocity technique,[43] incorporating the diffraction correction of Brendel.[44] The nearfield transmission sensitivity as a function of frequency is shown in Figure 18. The low Q of about 5 has been bought at the cost of the efficiency, which was typically 30%. However, the sensitivity was quite sufficient for the purposes of this study, and the useful bandwidth of ∿250 kHz sufficiently large.

To investigate the degree to which the primary field conformed to the theoretical assumptions of a long and collimated nearield and negligible non-linear attenuation, the primaries were measured with a plastic P.D.F. film hydrophone.[45] The variation of on-axis transmission sensitivity with drive voltages is shown in Figure 19, and the variation of beam cross-section with range is shown in Figure 20. At low drive voltages ($\lesssim$ 10 V), the behaviour is a good approximation to the theoretical behaviour of a baffled piston:[36] the last axial maximum occurs at a range of $R^2\omega_0 c/2\pi$, and is accompanied by a corresponding focussing of the primary field, clearly seen in cross-section (Figure 20) at 0.5 m range. At ranges less than 0.5 m, the field is well collimated, but beyond it becomes progressively less so. Remembering, however, that the virtual source strength is proportional to the square of the primary pressure, it can be seen that even at 0.75 m the assumption of collimation is still reasonable.

At drive voltages higher than 10 V, the effect of non-linear attenuation becomes increasingly important. It can be deduced from Figure 19 that at a range of 1 m, the absolute primary pressure on axis at 80 V drive level is the same as at 40 V drive level! To avoid non-linear attenuation having any significance, a drive level of 30 V was chosen. For ranges $\lesssim$ 0.5 m, approximately the largest distance to the truncation, this ensured a linear primary transmission sensitivity.

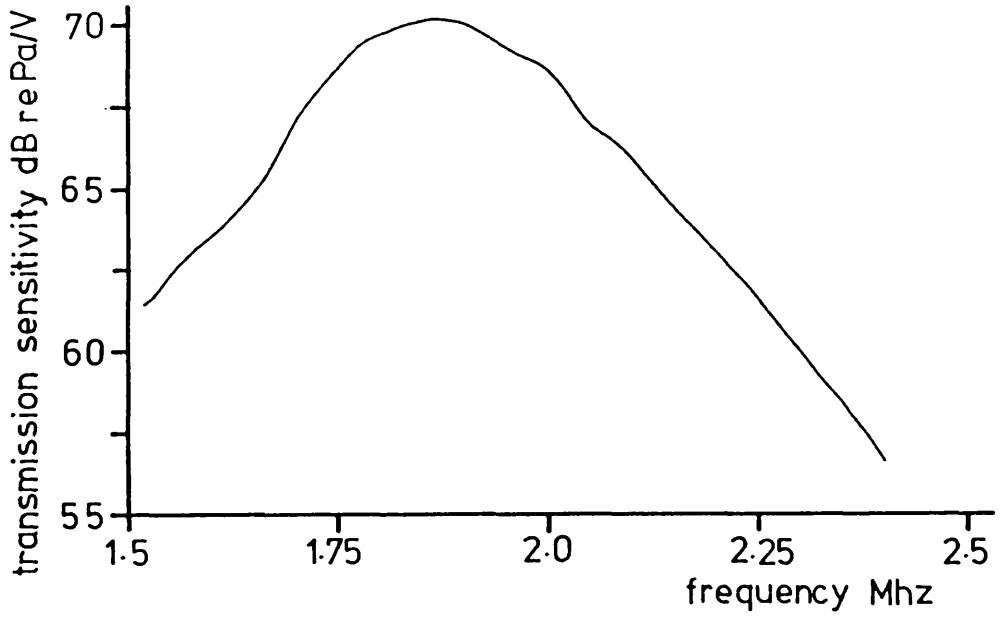

Figure 18 Primary nearfield (plane wave) transmission sensitivity as a function of frequency.

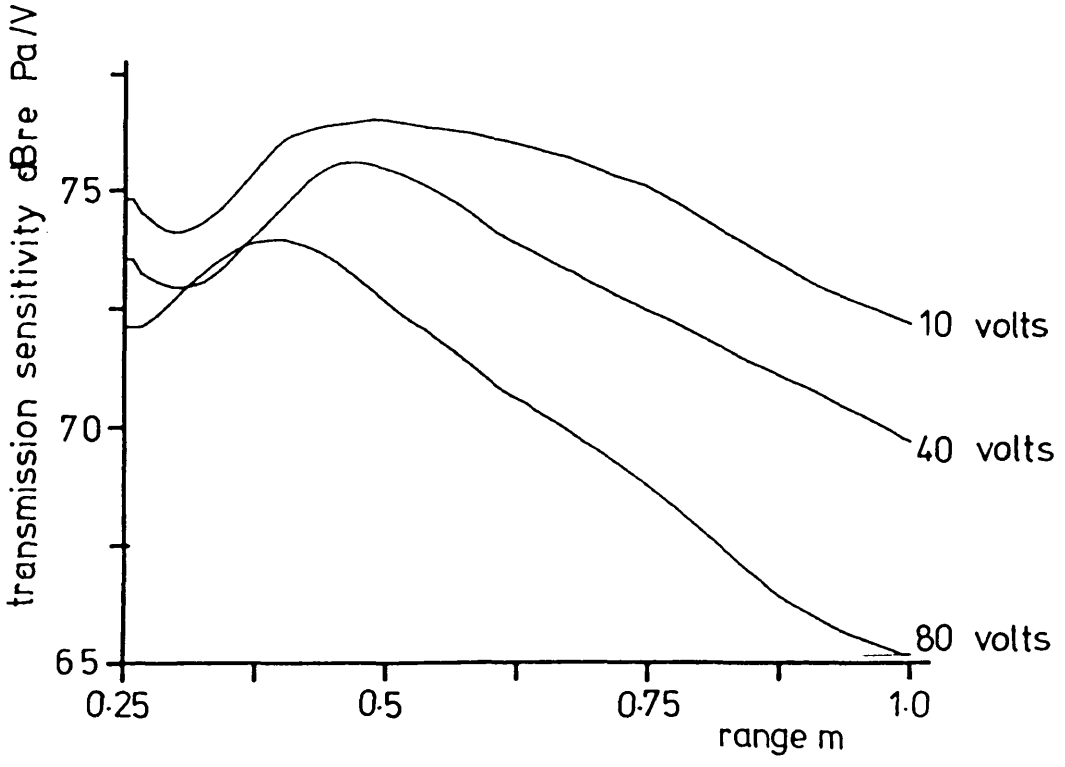

Figure 19 Primary transmission sensitivity as a function of range at three drive voltages, 10 V, 40 V and 80 V.

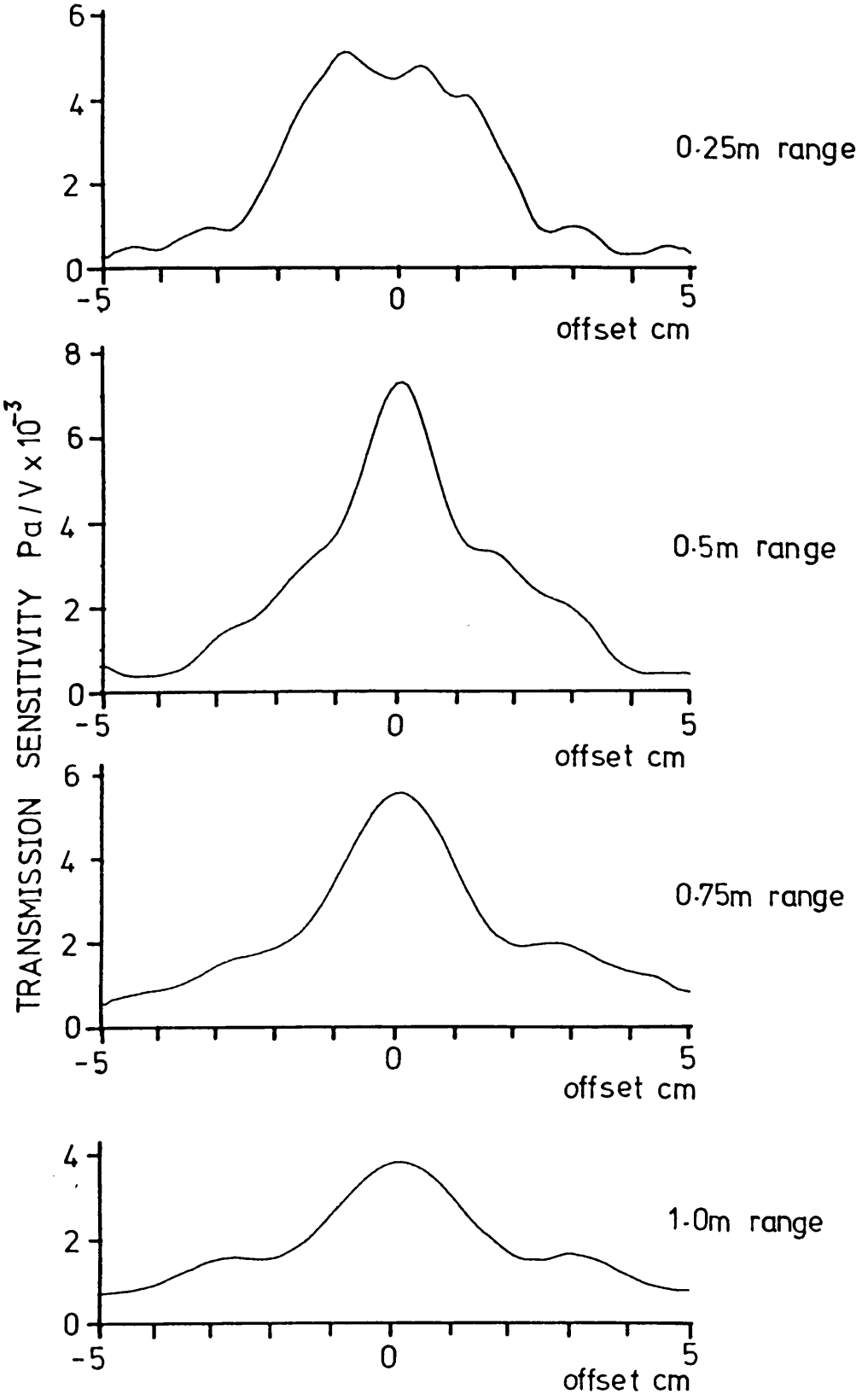

Figure 20 Primary transmission sensitivity across the beam at four ranges. R^2/λ for this transducer is at 0.5 m.

The acoustic filter

The acoustic filter provides a mechanism for artificially truncating the primaries in water. It is a cork loaded butyl rubber sheet, which acts as a low pass filter to plane waves. To find the loss at difference frequencies, the pulse from an already terminated array was measured with and without the filter present. Above 300 kHz, the loss was measured with the direct radiation of the primaries. The transmission loss as a function of frequency is shown in Figure 21. At the primary frequency of 2 MHz, the loss is ∿60 dB, which is a 120 dB loss in secondary source level.

The reception System

The hydrophone

For reception of difference frequency signals both in water and in sediment a B & K 8103 miniature hydrophone was used. The receiving sensitivity in water of the hydrophone was measured with three transducer reciprocity and is shown in Figure 22. (The calibration in the sediment is discussed later.) The directivity of the hydrophone in the equitorial plane is quoted as ±2 dB at 200 kHz, so it was always orientated in the same sense when used for absolute measurements.

Amplification and filtering

The output from the hydrophone was passed to a Brookdeal 9452 Precision pre-amplifier with variable gain from 20 - 100 dB. The input impedance of 100 MΩ in parallel with 20 pF was essentially open circuit for the hydrophone with a capacitance of 3.6 nF. The output was passed to a Krohn-hite 3100(R) bandpass filter. This was a Butterworth low pass filter in series with a Butterworth high pass. In both cases the attenuation was 3 dB at the cut-off, continuing downwards at 24 dB/octave. The phase response was poorer, ±180° for 3 octaves on either side of the cut. Usually

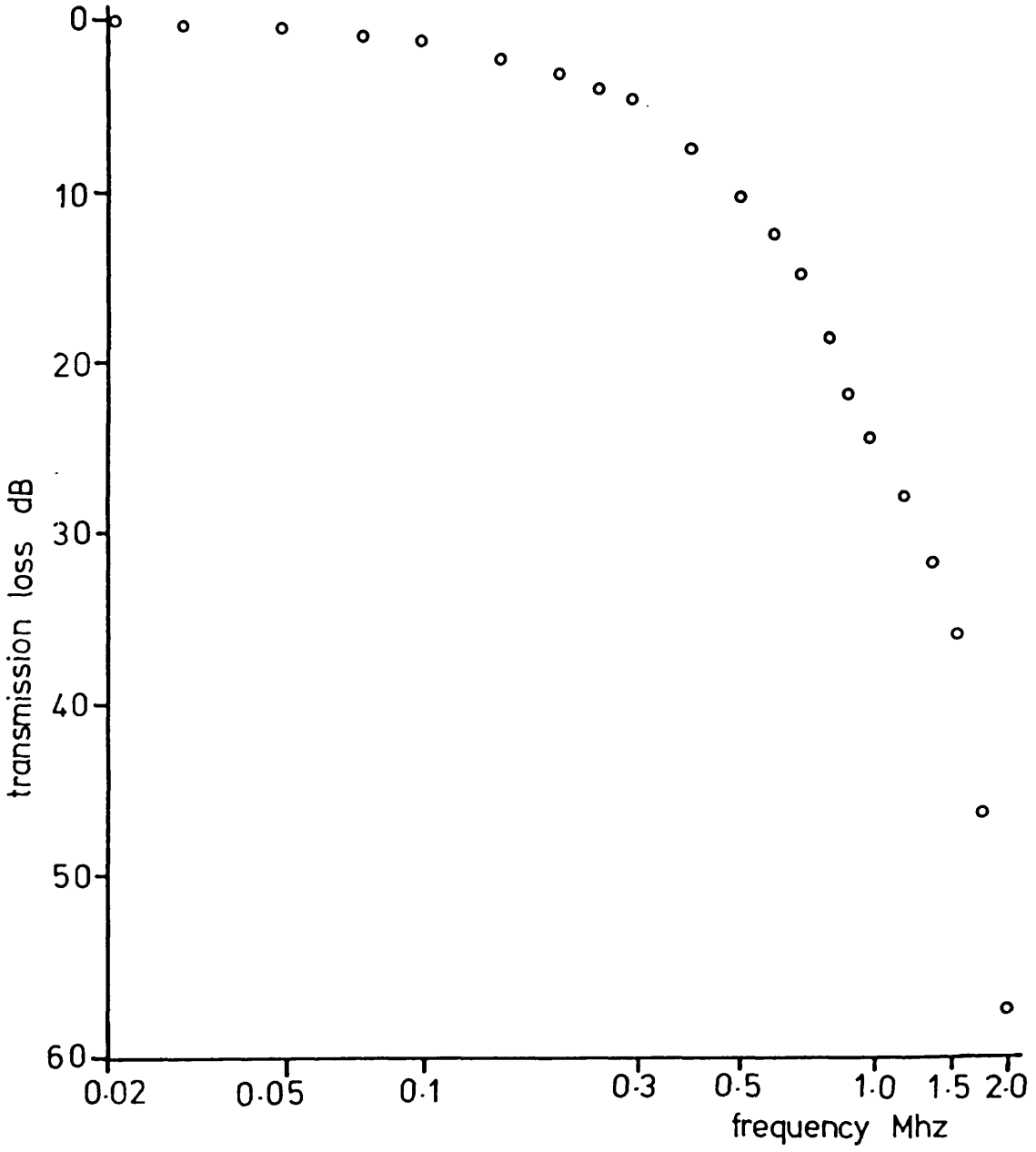

Figure 21 Transmission loss of the acoustic filter as a function of frequency.

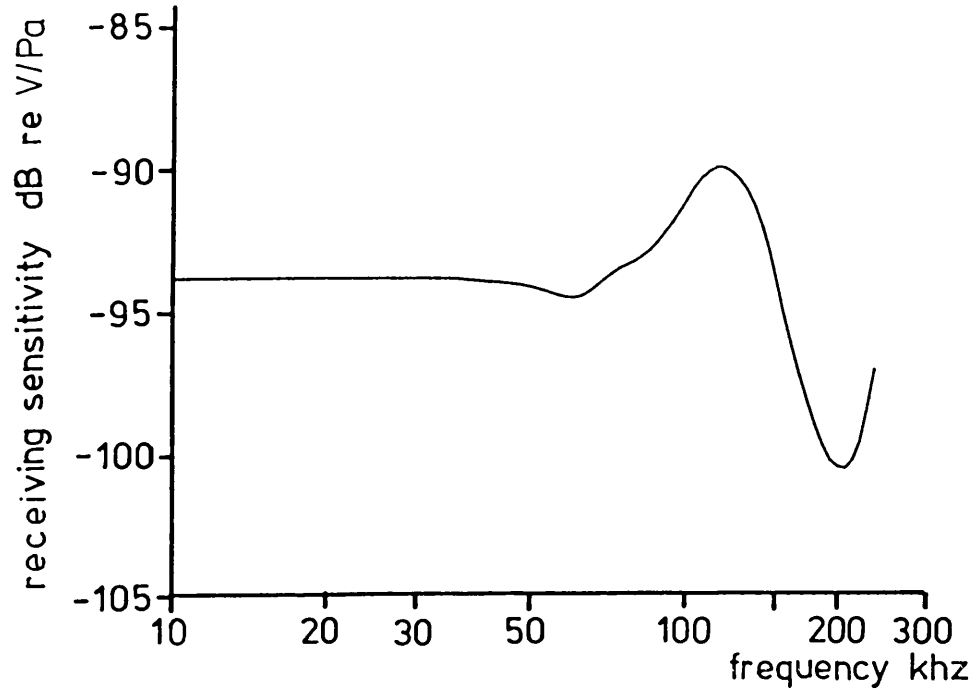

Figure 22 B and K 8103 hydrophone receiving.sensitivity as a function of frequency.

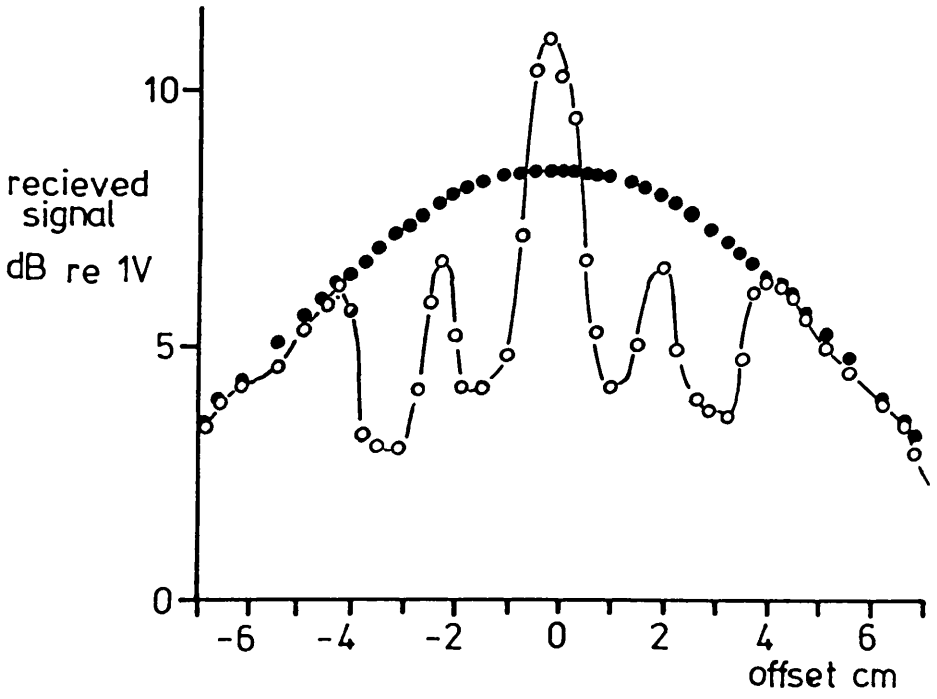

Figure 23 The effect on the secondary beam pattern of primary non-linearity on reception. ●: undisturbed beam pattern at 25 kHz; O: beam pattern with primaries incident upon the hydrophone.

the low cut would be set at 1 kHz to remove extraneous low frequency noise, the high cut at 700 kHz to remove any primary energy received by the hydrophone, or, occasionally, at a lower value when an antialias filter was required. Both these instruments were active devices.

Display and recording

The main display instrument was a Gould OS 3500 60 MHz oscilloscope, which was used to monitor both the voltage supplied to the transducer and the output of the hydrophone-amplifier-filter receiver. Two recording instruments were available for the digital recording of the signals, both of which were interfaced into the computer. For high (primary) frequency work and high signal-to-noise (SNR) ratios, a Datalab DL910 transient recorder was used, providing considerable flexibility of sample intervals and data lengths. With a high SNR the signal could be averaged in the computer with repeated recording. For very low SNR, when this method became too time-consuming, the transient recorder was replaced with a H.P. 3721A correlator. This instrument had a minimum sample interval of 1 μs (hence an alias frequency of 500 kHz) and would record only 100 samples. It would, however, hardware add up to 128000 recordings at a rate determined by the trigger, meaning that signals could be recorded in otherwise hopeless SNR environments.

The output from both instruments could be displayed in addition to being recorded on the computer. In the case of single frequency measurements the amplitude was measured directly from the display; for pulse measurements, the entire signal was recorded for processing later.

Linearity of the reception system

The presence in the water of two signals with a large difference in amplitude meant that it was important to establish that non-linearity in

the recording system could be neglected. Usually, in non-linear work, this problem is dealt with by the introduction of a passive filter between the hydrophone and amplifier. In this study, however, the passive filter concerned was acoustic, either the artificial butyl rubber one, or the natural filter of sediment attenuation.

Non-linearity in the detection system may be identified by the presence of the primary beam pattern being superimposed on the expected difference frequency beam pattern.[47] Figure 23 shows this effect clearly, in a beam cross-section measured at a difference frequency of 20 kHz, a range of 0.5 m, a drive level of 30 V, and 60 dB pre-amplifier gain. The cross-section has been measured both with no aoustic filter present, the black dots, and with the filter placed immediately in front of the hydrophone, the white dots. The removal of the filter allows the primaries to reach the hydrophone. The resulting signal generated non-linearly in the receiving system interferes with water generated difference frequency signal: the zone of interference, ±4 cm of offset, is equal to primary beam width at 0.5 m, as can be seen from Figure 20.

Figure 23 allows an estimate of the second order sensitivity,[47] $\tau_2(\omega_0)$, of the receiving system. $\tau_2(\omega)$ is defined by assuming the reception to have a (weakly) non-linear response to an incoming wave, $p_0(t)\cos(\omega' t - kx)$:

$$\tau(\omega',t) = \tau_1(\omega')p_0(t)\cos(\omega' t - kx) + \tau_2(\omega')\frac{p_0^2(t)}{2}[1+\cos 2\omega_0 t] \qquad (5.5)$$

Figure 23 shows the interference of the water generated difference frequency signal, $\tau_1(\omega)p(\omega)$ and the contribution of the primaries at the difference frequency *via* reception non-linearity, $\tau_2(\omega_0)p_0^2/2$. It is convenient to measure τ_2 referred back to the hydrophone output. With the acoustic filter present, the on axis incident pressure is 100 Pa. The +3.5 dB - 5 dB interference implies that

$$\frac{\tau_2(\omega_0)p_0^2(t)}{2} \simeq 0.5\ \tau_1(\omega)p(\omega) \qquad (5.6)$$

At 30 V, drive level $p_0(t)$ is (from Figure 20) 2.1×10^5 Pa, and making the relevant substitutions, gives:

$$\tau_2(\omega_0) = -258 \text{ dB re } 1 \text{ V/Pa}^2$$

Referring $\tau_2(\omega_0)$ back to the hydrophone makes it independent of pre-amplifier gain. Experimentally, it was found to be a very weak function of amplifier gain (±3 dB) up to 60 dB. Above this value it rose rapidly with pre-amplifier gain. For this reason, gains higher than 65 dB were avoided.

The sediment

The sediment used throughout this study was a fine sand supplied by British Industrial Sands Ltd., Redhill. Its physical properties are summarised in Table 5.1.

Table 5.1 (from ref. 48)

Diameter (ϕ)	Deviation (σ_ϕ)	Porosity (%)	Wet density (kg m^{-3})	Specific gravity
2 (250 μm)	0.5	43	1946	2.64

The sand was contained within the smaller of the two tanks in Figure 13. The dry sand was placed in a pressure vessel (a beer barrel, in fact) and this was evacuated. The barrel was then emptied into the sediment under water. This procedure ensured the sand was air-free, and using two tanks allowed the water level to alter without aerating the sand.

Acoustically, the wet sand was found to be variable in its properties. A continual problem during the experiments was the uneven settlement of the sand, and of the hydrophone "plant" when buried in the sand. To provide as

uniform and consistent a sediment as possible, each time the sand was disturbed, it was shaken for some hours with a 1" vibrating poker of the type used to remove air from wet concrete.

The sound attenuation and velocity dispersion were measured using the wideband signal generated by a truncated parametric array. The attenuation as a function of frequency is shown in Figure 24; the velocity dispersion in Figure 25. The scatter of these data gives an indication of the acoustic variability of the sand itself. These measurements are of considerable intrinsic interest: previous attempts to measure the velocity dispersion in saturated sands have failed to find any.[55,56] For this reason, a detailed account of the experimental procedure is given in Appendix C.

The solid line in Figure 24, which has displaced +10 dB for clarity, shows an absorption of 0.36 dB/λ, which was taken to be representative of the data. (For the reasons described in Appendix C, no attempt at regression has been made.) The solid line in Figure 25, displaced by +0.004 for clarity, is the velocity dispersion required by the constraint of wave causality when the attenuation is 0.36 dB/λ: it is as reasonable a description of the dispersion as 0.36 dB/λ is of the absorption. These two solid lines were used in any theoretical description of the sediment.

Hydrophone calibration in the sediment

The calibration of the hydrophone introduced the first large uncertainty in the measurements in the sediment. Even after shaking the sand, the calibrations still showed variations of $\lesssim$ 2 dB due, presumably, to "plant" *i.e.*, the local disruption of the sand around the hydrophone. Because of this variation, the three transducer calibration[43] was performed with two of the hydrophones in the water above the interface, as shown schematically in Figure 26. The usual equation for the sensitivity becomes slightly more

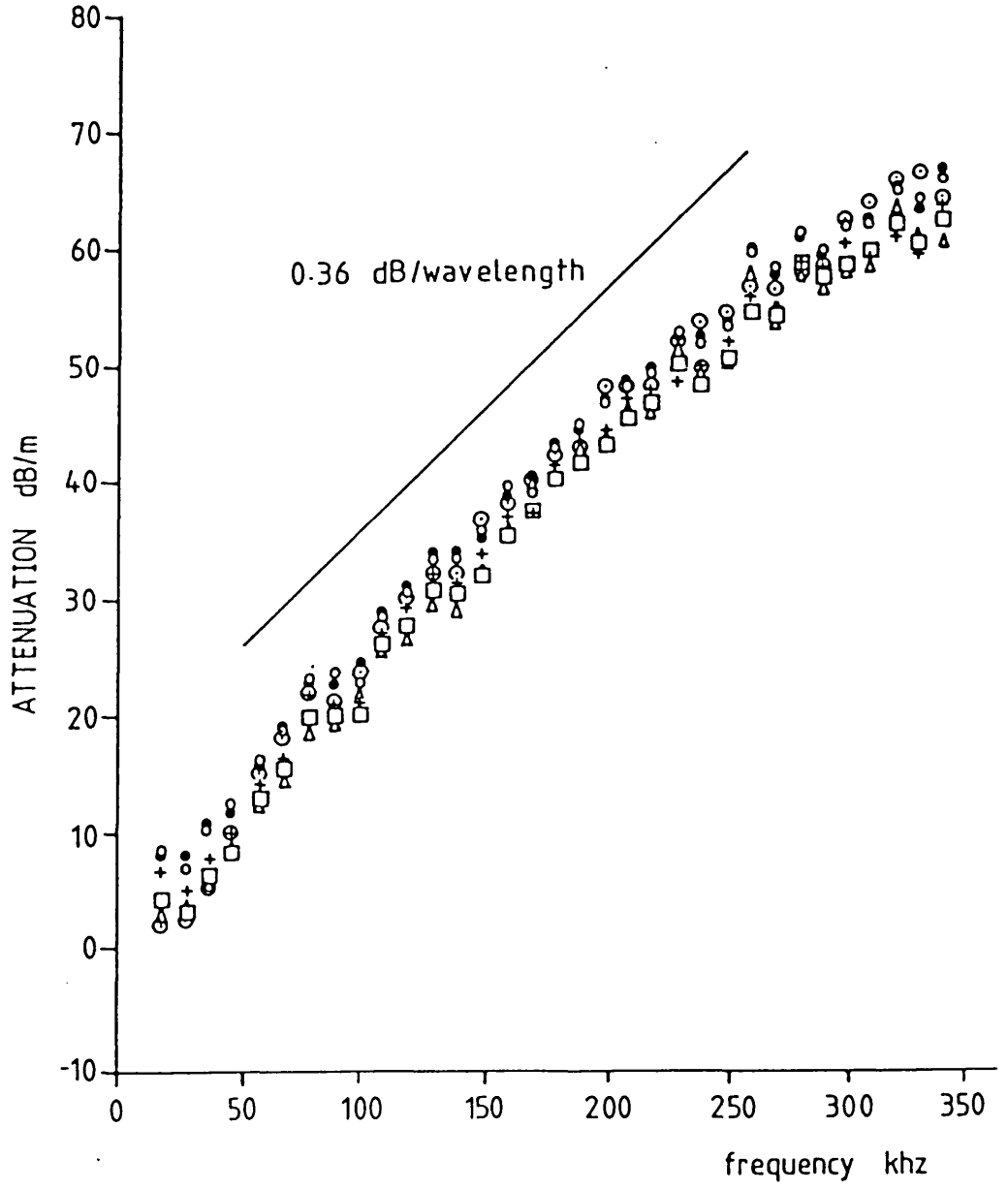

Figure 24 The attenuation of the sound in the sediment. (See Appendix C for a detailed description of this graph.)

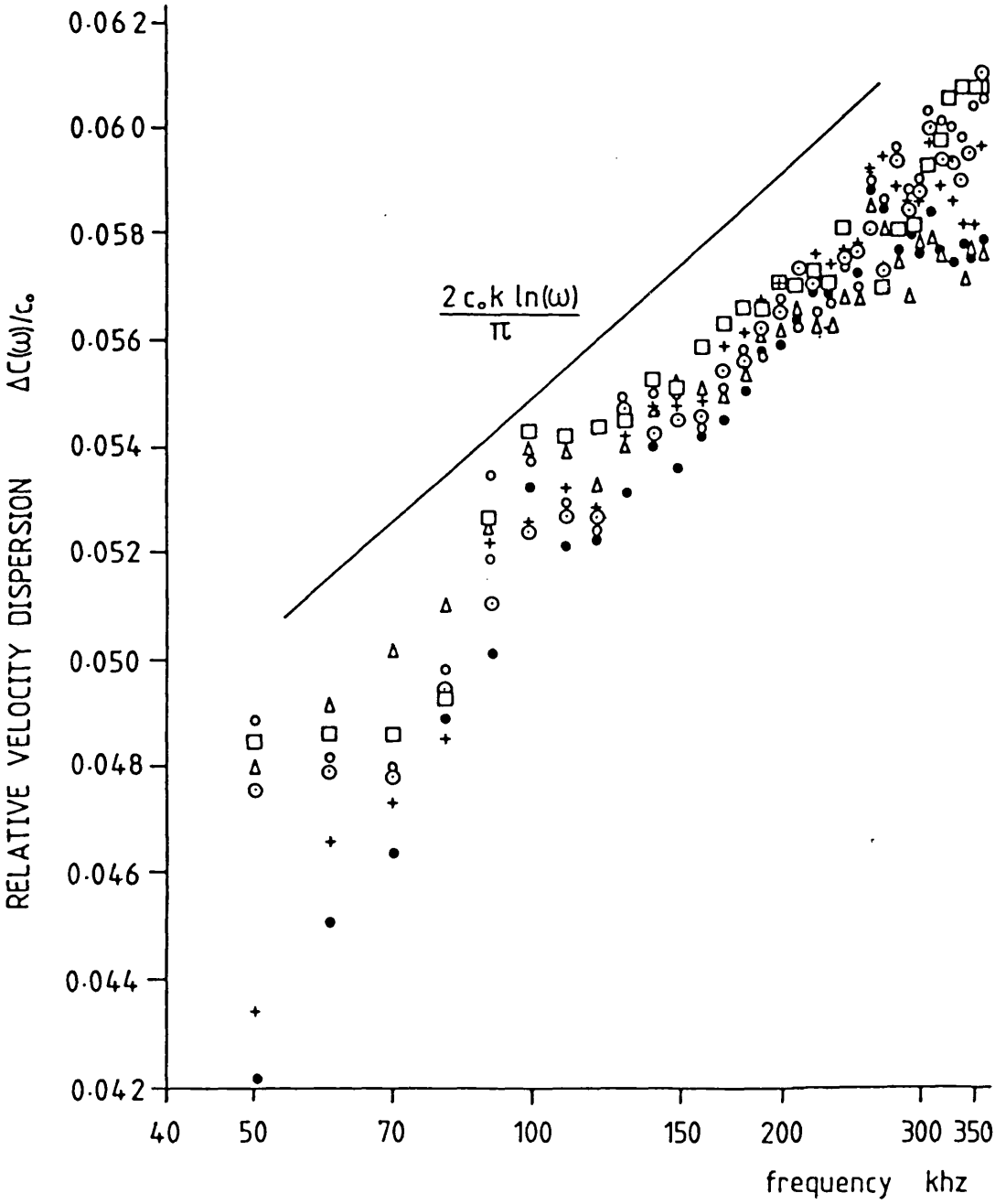

Figure 25 The dispersion of sound in the sediment. (See Appendix C for a detailed description of this graph.)

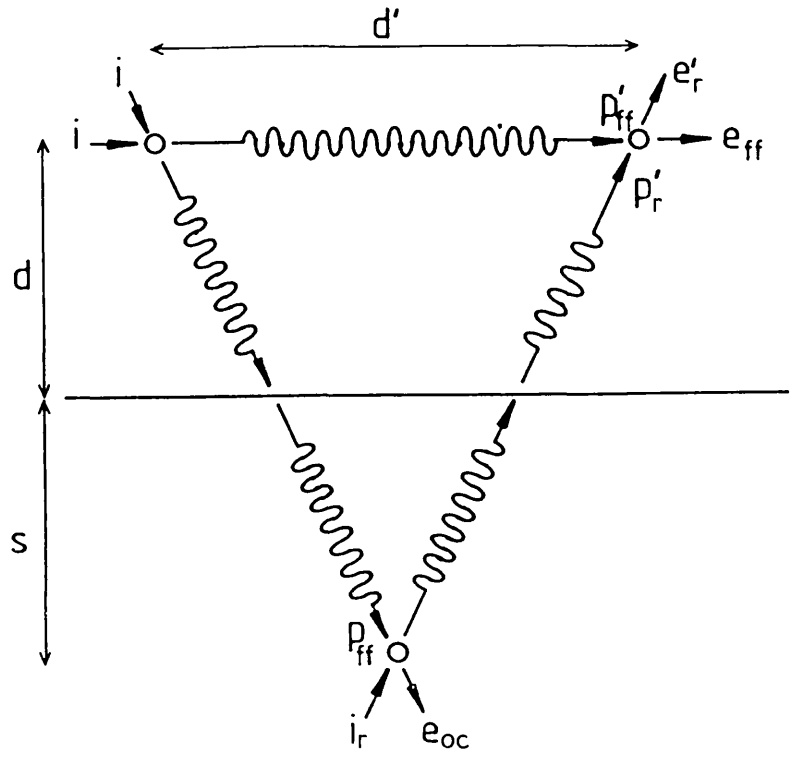

Figure 26 Schematic representation of the reciprocity calibration through an interface.

Notes: $\tau_s(\omega)/S_s(\omega) = J_s(\omega) = (4\pi d_0/i\omega\rho)e^{ikd_0}$, where $J_s(\omega)$ is the reciprocity constant in sediment and $S_s(\omega)$ is the transmission sensitivity in sediment.

By definition $\tau_s(\omega) = e_{oc}/p_{ff}$

$$= \frac{e_{oc}(d+s/n)}{p_{ff}'d'T_{12}} e^{ik(d-d')+ik_sS}, \text{ where } T_{12} = \frac{2\rho_s c_s}{(\rho_s c_s+\rho c)},$$

$$= \frac{e_{oc}e'_r}{e_{ff}p_r'} \frac{(d+s/n)}{d'T_{12}} e^{ik(d-d')+ik_ss}$$

$$= \left(\frac{e_{oc}e_r'}{e_{ff}i_r}\right) \frac{(d+s/n)(s+nd)}{d'T_{12}T_{21}} \frac{e^{2i(kd+k_ss)-ikd'-ikd_0}}{S_s(\omega)d_0},$$

where $T = \frac{2\rho c}{(\rho_s c_s+\rho c)}$. Therefore:

$$\tau_s^2(\omega) = \left(\frac{e_{oc}e_r'}{e_{ff}i_r}\right)\left[\frac{(d+s/n)(s+nd)}{d'T_{12}T_{21}}\right]\left(\frac{4\pi}{i\omega\rho_s}\right)e^{ik(2d-d')+2ik_sS}$$

complicated than usual,* as correction must be made for transmission through the interface. In passing through the interface a (high frequency) spherical wave refacts, changing the centre of its spherical divergence, and only a fraction gets transmitted. (These remarks follow from the derivation of Section 3.) The plane wave transmission coefficient at normal incidence is given by equation (2.18) with $k_2 = \omega/c$ and $k_S = \omega/c_S$. The spherical spreading correction comes from a more general form of equation (3.28) to include the raypath in water. In the notation of Figure 26, the spherical spreading from water to sediment is $1/(d+s/n)$; from sediment to water $1/(nd+s)$. These two results may be used to modify the reciprocity calculation used in water. Figure 26 has a schematic representation of the derivation, resulting in the following equation for the hydrophone sensitivity in sediment $\tau_S(\omega)$:

$$\tau^2{}_S(\omega) = \left(\frac{e_{oc}}{e_{ff}} \frac{e_r}{i_T}\right) \frac{(cd+c_s s)}{(\rho c+\rho_S c_S)^2} \frac{4\pi\rho}{\omega} e^{2i\omega(d/c+s/c_S)} \qquad (5.7)$$

where it is appreciated that c_S is complex.

The results of the three calibrations, each separated by a reburial of the hydrophone, are shown in Figure 27. The scatter around 100 kHz is $\sim$1.5 dB. In comparison with the calibration in water, Figure 22, the hydrophone in sediment is marginally less sensitive, but the differences are not dramatic.

---

*There is, of course, the tacit assumption that both reciprocity holds and the reciprocity constant remain unchanged in the presence of absorption. Short of a model of sediment absorption, there is little alternative.

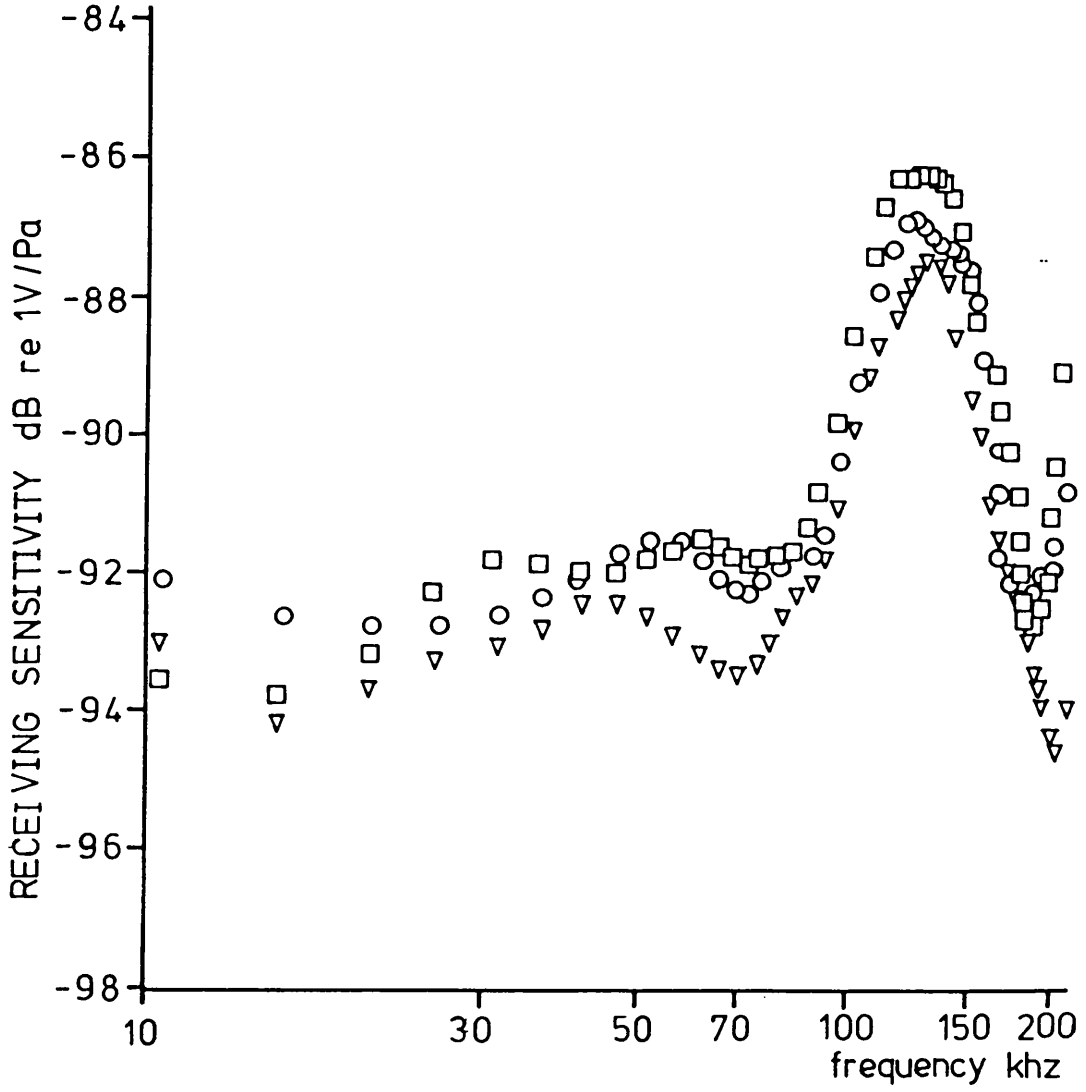

Figure 27 The receiving sensitivity of the B and K 8103 hydrophone in sediment. Each curve corresponds to a separate reburial of the hydrophone.

CHAPTER 6

Secondary Field Measurements in Water and Sediment

In this chapter, the experimental measurements of the secondary field are described. These were designed to test the predictions of the theory, in particular that:

(a) the simplified model of the primary field was adequate;

(b) the high incident angle penetration associated with parametric arrays was due to the truncation aperture;

(c) this penetration is limited to a shallow region beneath the interface by the directivity of the truncation aperture; and

(d) the field very close to the interface is dominated by the evanescent arrival.

The ability to truncate the primaries artificially in water using the acoustic filter allowed (a) to be investigated independently of the interface. In addition, measuring the field in water provided a yardstick for the performance in the sediment both with regard to qualitative features such as the sharpness of the truncation aperture and quantitative features such as the accuracy of the farfield theory.

In the sediment, nearfield truncation theory concludes that the relationship between the primary beam incident angle and the transmitted secondary field is complicated; indeed, a unique angle of transmission of a parametric array at finite range is not definable (see Figure 3). A detailed investigation of the secondary field would have to include measurements of the spatial and angular distribution of the secondary field. Therefore, to investigate (b) and (c), the secondary field was measured throughout two perpendicular planes in the sediment at fixed incident angles, and over a range of incident angles at fixed locations in the sediment.

Very close to the interface, the possibility of reflections made the toneburst experiments ambiguous. The very shallow arrivals were observed with both toneburst and pulse measurements to investigate (d).

The secondary field in water

The secondary field measurements in water were carried out using the geometry of Figure 28. The primary field was truncated using the acoustic filter at distance L from the transducer and the hydrophone placed at a range P and offset H. The array was driven with a 100 kHz toneburst [voltage signal: equation (5.1)], and received signal amplitude was measured directly from the oscilloscope.

The simplest test of the model used to describe the primaries would be to measure the on-axis secondary field as a function of range from the transducer with the array unterminated. At large enough ranges, the secondary field due to collimated plane waves would grow logarithmically.[51] To avoid problems of non-linearity, the only slightly more complicated arrangement of having the filter immediately in front of the hydrophone was used (*i.e.*, L = P), and the results are shown in Figure 29. The measured pressure is compared with the "exact" expression, equation (3.13), which also grows logarithmically at large ranges.

Up to ranges of $\sim$0.4 m, the form of the two curves is the same, but there is some 1-2 dB difference. Above 0.4 m the secondary pressure ceases to grow and the divergence from the theory increases. The > 2 dB agreement at lower ranges is consistent with other investigations.[52] Partly reflecting the gross approximations to the primary field, the error also embodies the uncertainty in the primary pressure calibration. It is the square of this value which enters the theoretical calculation and introduces an uncertainty of $\sim$ 1 dB. The gradually increasing difference between the two

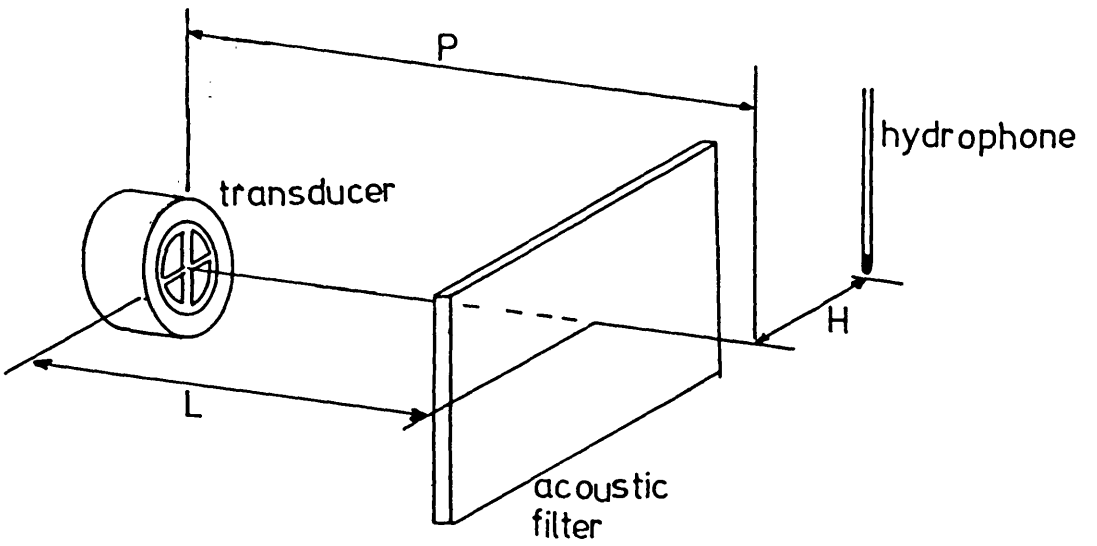

Figure 28 The geometry of the experiments measuring the secondary field in water.

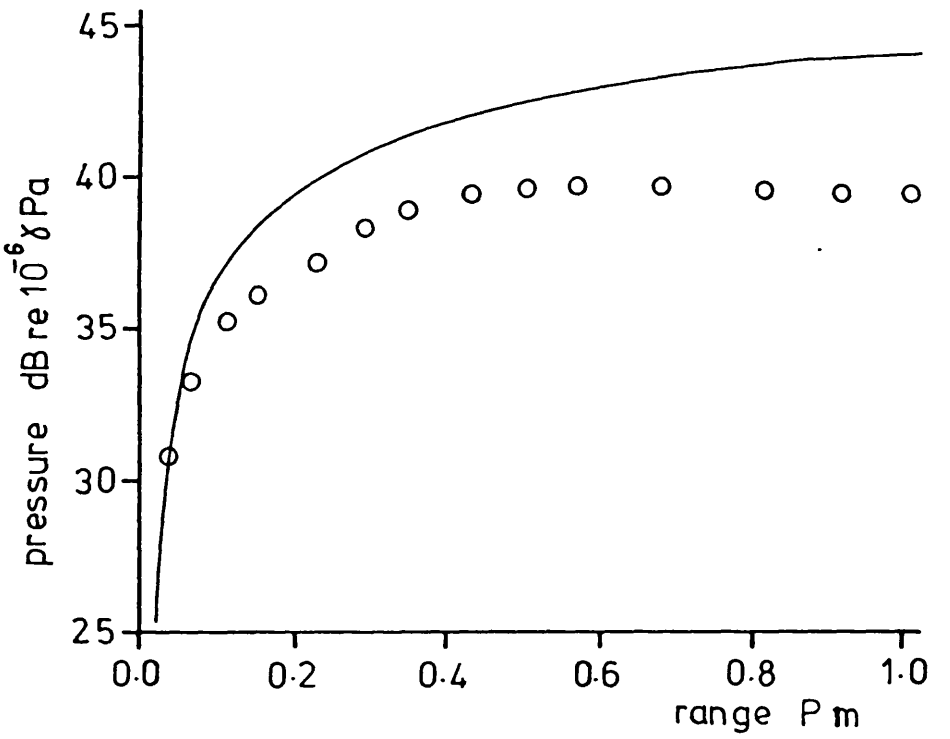

Figure 29 The variation of secondary pressure with range. The array was truncated at a distance L equal to P. ——— : "exact" theory, equation (3.13); O: experiment.

curves above 0.4 m is due to the primaries' spherical spreading. Smith *et al.*,[32] by extrapolating Rolleigh's[26] results into the nearfield, would conclude the changeover between plane and spherical regimes (of the secondary nearfield) occurs at a distance of 0.8 m for this transducer, although Humphrey's[52] experiments, in common with the author's, place the secondary maximum at a smaller range.

The theoretical expressions in the sediment are strictly valid only in the farfield of the array. The equivalent expression in water, equation (3.9), was compared with the variation in on-axis secondary pressure from an array truncated at 0.5 m. The results are shown in Figure 30. Also plotted on the graph is the "exact" result, equation (3.13), and the farfield expression. In common with the "exact" result, the measured pressure shows a more pronounced spherical decay than the farfield expression, indicating that the centre of the secondary sources is closer to the field point than the transducer. Not surprisingly, all three curves tend to a similar asymtote; the difference between the measured pressure and the farfield prediction at a range of twice the array length is < 1.5 dB.

The behaviour of the secondary beam in cross-section at a range of 1 m from the array truncated at 0.5 m is shown in Figure 31. In addition, the theoretical farfield, equation (3.9), and Fresnel corrected, equation (3.11), expressions have been plotted. Even at this range, the Fresnel correction is necessary to predict correctly the beam width of the main lobe; the farfield expression overestimates the beamwidth by several degrees. Berktay[30] introduced the correction for just this purpose.

In the skirts of the beam, the position is more confused. The measured pressure does not have the sidelobes which the theoretical curves predict; rather, the pressure decreases in smooth steps away from the beam axis. The

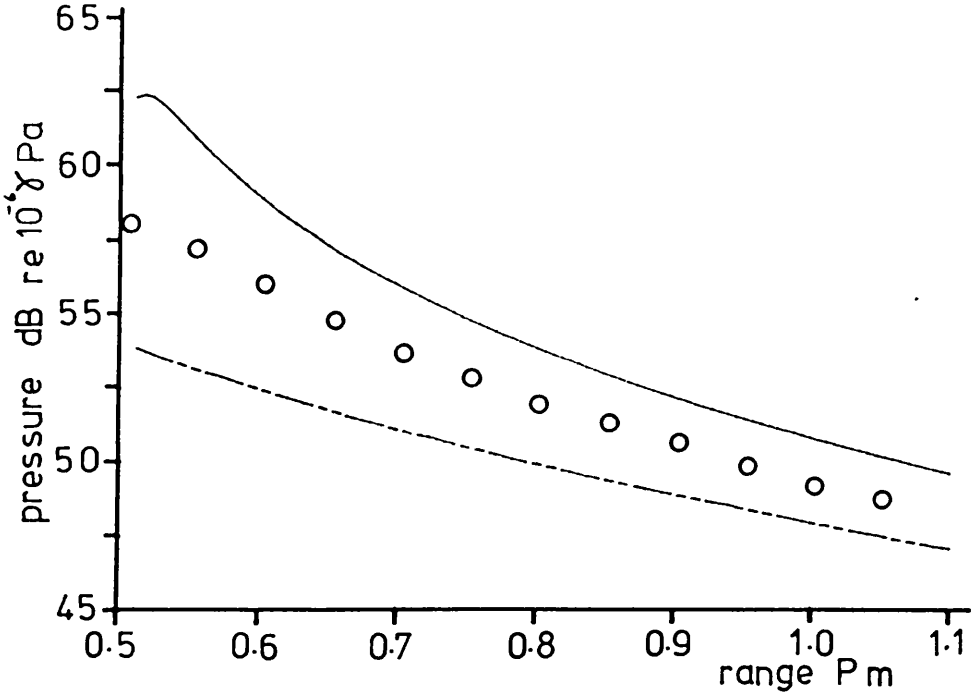

Figure 30 The variation of secondary pressure with range for a fixed truncation length L = 0.5 m. ————: "exact" expression, equation (3.13); – – – ····: farfield expression, equation (3.9); O: experiment.

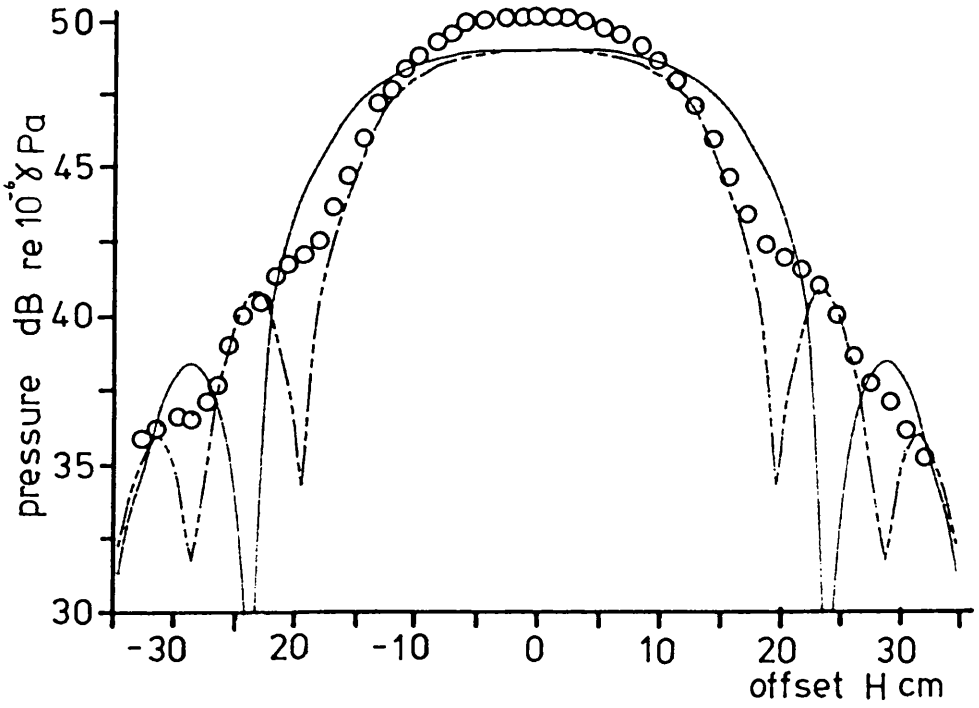

Figure 31 The variation of secondary pressure in cross-section at a range P = 1 m for a fixed truncation length L = 0.5 m. ————: farfield expression, equation (3.9); – – –: Fresnel corrected expression, equation (3.11); O: experiment.

location and general pressure level of the steps does coincide with the sidelobes of the Fresnel prediction. This behaviour can be accounted for by assuming the truncation arrival to be rather smaller than predicted, interfering with the transducer arrival, but insufficient to cancel it completely. However, the detailed behaviour of the truncation aperture may not be inferred from Figure 31. It does give warning that the off-axis behaviour of the secondary field in sediment may differ in detail from the theoretical predictions.

The secondary field in the sediment

The field in the sediment was measured with the hydrophone buried in the sediment. In Figure 3, the geometry of the experiments is shown. The relationship of the transducer to the hydrophone is uniquely described by the four space co-ordinates x, y, L, d and the tilt co-ordinate α (equal to the incident angle of the primary beam on the interface). For all the experiments in the sediments, L was fixed and equal to 0.2 m.

The hydrophone was buried using the procedure described previously for its calibration. The interface was levelled with a horizontal metal scraper attached to the gantry which was lowered to the interface and traversed back and forth until the boundary was flat. The final traverse was performed using the computer driven stepping motor at a very low speed, which ensured a plane finish. The surface finish of the interface was checked by shining (reflected) light across it at a very acute angle. Any imperfection could be identified easily by the shadow it threw. Following this procedure, the hydrophone was located acoustically with the array normally incident on the boundary.

The secondary field in sediment at fixed primary incident angles

In these experiments, the field was measured in two vertical planes through the sediment; one coincident with the beam axis, and the second

perpendicular to it. Because of the obvious difficulty of moving the hydrophone through the sediment, the pressure variation throughout the plane was synthesised in the following manner.

The hydrophone was buried at a suitably large depth (usually ∿20 cm) with its equatorial plane set vertically. The array incident angle was set to the desired value and the field from a 100 kHz toneburst measured at the hydrophone. The range x or offset y was varied by moving the transducer, rather than the hydrophone, and in this way the secondary field anywhere in the horizontal plane d = constant could be measured. A known thickness of sand was then removed from the interface, which was then scraped flat again in the manner described, and the transducer was lowered by the depth of sand removed to maintain a constant height above the interface, L = 0.2 m. The measurements could then be repeated throughout another plane d = constant. By the removal of a number of layers of sediment, a picture of the pressure variation in vertical planes through the sediment could be built up, and used to draw pressure contour maps for each plane.

It has already been shown that pressure measured by the hydrophone varies with each reburial, introducing an uncertainty of ∿1.5 dB at 100 kHz. Experience showed that the scatter of pressure measurements at non-normal incidence was rather greater than this: 2 - 2.5 dB. Figure 32 shows the pressure measured for the traverse x = 0.2 - 0.7 m, y = 0 and d = 0.1 m, with a beam incident angle of 50°, after three reburials of the hydrophone, and it is seen that the scatter is 2 - 2.5 dB. There are two possible causes for this increase in uncertainty over that due to the hydrophone: scattering from an imperfect interface; scattering of the beam from within the sand. Either of these is possible, but in view of the exhaustive efforts to produce a good quality finish at the interface, the latter is considered to be more likely. Much time was spent trying to locate the cause of this scattering without much success; the use of the concrete poker served to minimise its

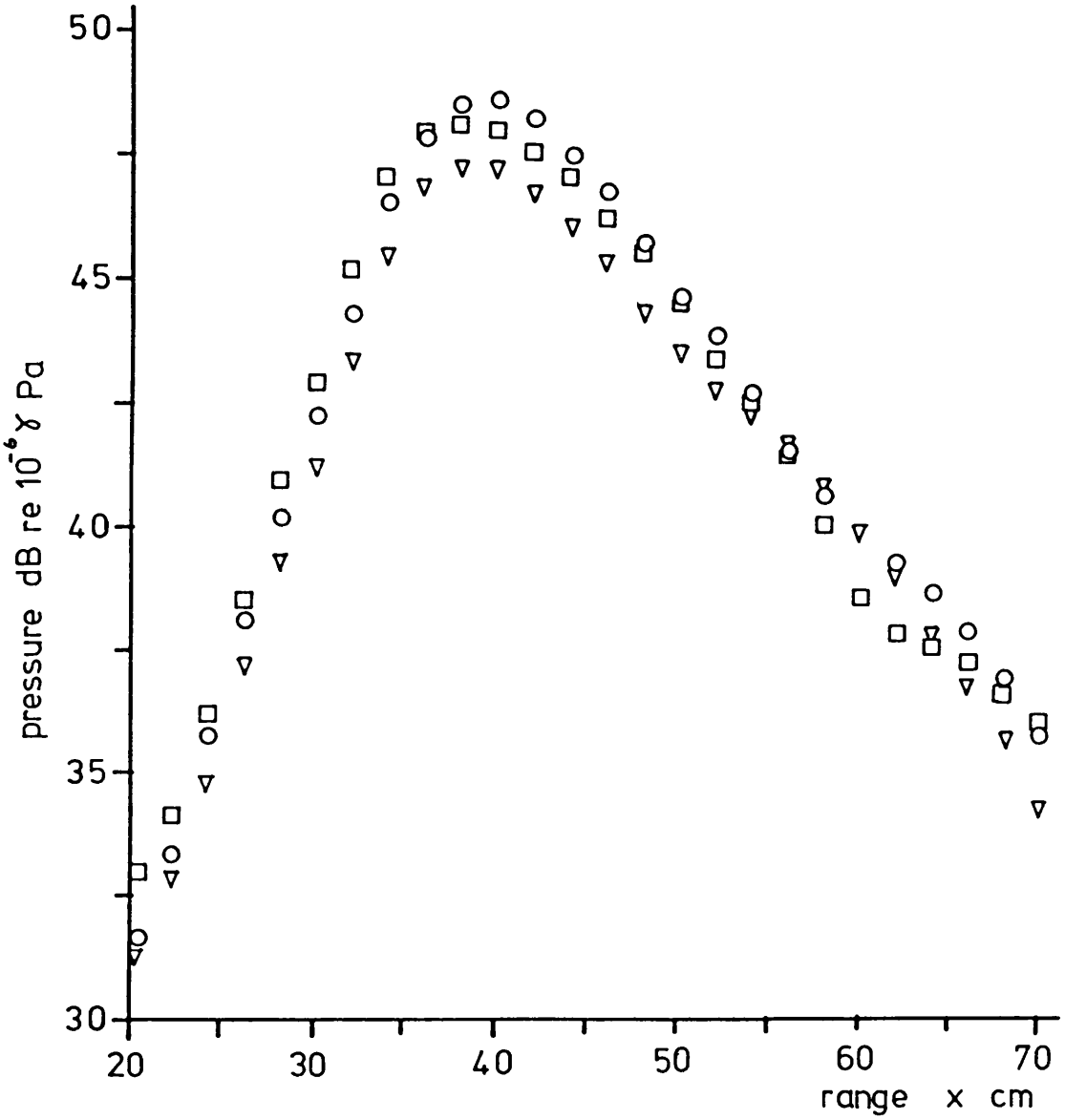

Figure 32 The secondary pressure in sediment along the line y = 0, d = 10 cm with an array incident angle of 50°, at 100 kHz. Each curve corresponds to a separate reburial of the hydrophone.

effects. The acoustic variability of sediment has caused other workers problems.[49] At any rate, it is important to appreciate that all the succeeding graphs have an implicit variability explicit in Figure 32, and this may be regarded as the limit of the approximation of the sediment as homogeneous.

Subcritical incidence: $\alpha = 50°$

At a subcritical angle of beam incidence, $\alpha = 50°$, the pressure was measured in the two planes $y = 0$ and $x = 50$ (see Figure 3 for the geometry). The contour plots of the pressure contours throughout the entire planes were built up from the traverse measurements in the following manner.

The location of the traverse pressure variation's intersection with a 5 dB contour interval was recorded. In view of the unpredictable variation of Figure 32, 5 dB was chosen as the contour interval; variations of this magnitude should be significant (in the statistical sense). These locations were then mapped onto graph paper and the contours drawn by hand. (The position of a "*" on the contour plot is thus recorded data; the position of the contours is an interpretation.)

Figure 33 shows the pressure contours in the $y = 0$ plane, and Figure 34 shows the pressure contours in the $x = 0.5$ m plane. These may be compared directly with Figures 5 and 6 which were calculated with the correct values of the relevant constants. The agreement throughout is to within 2.5 dB; the slightly wavy quality of the experimental contours is the expected consequence of the problems of settlement discussed earlier. The theoretical prediction that the array behaves similarly to a conventional array at subcritical angles of incidence is correct. The "transmission angle" seen in Figure 33 is the Snell's law angle; the beam is slightly asymmetric top bottom, the width of the beam is little changed by the interface, as comparison

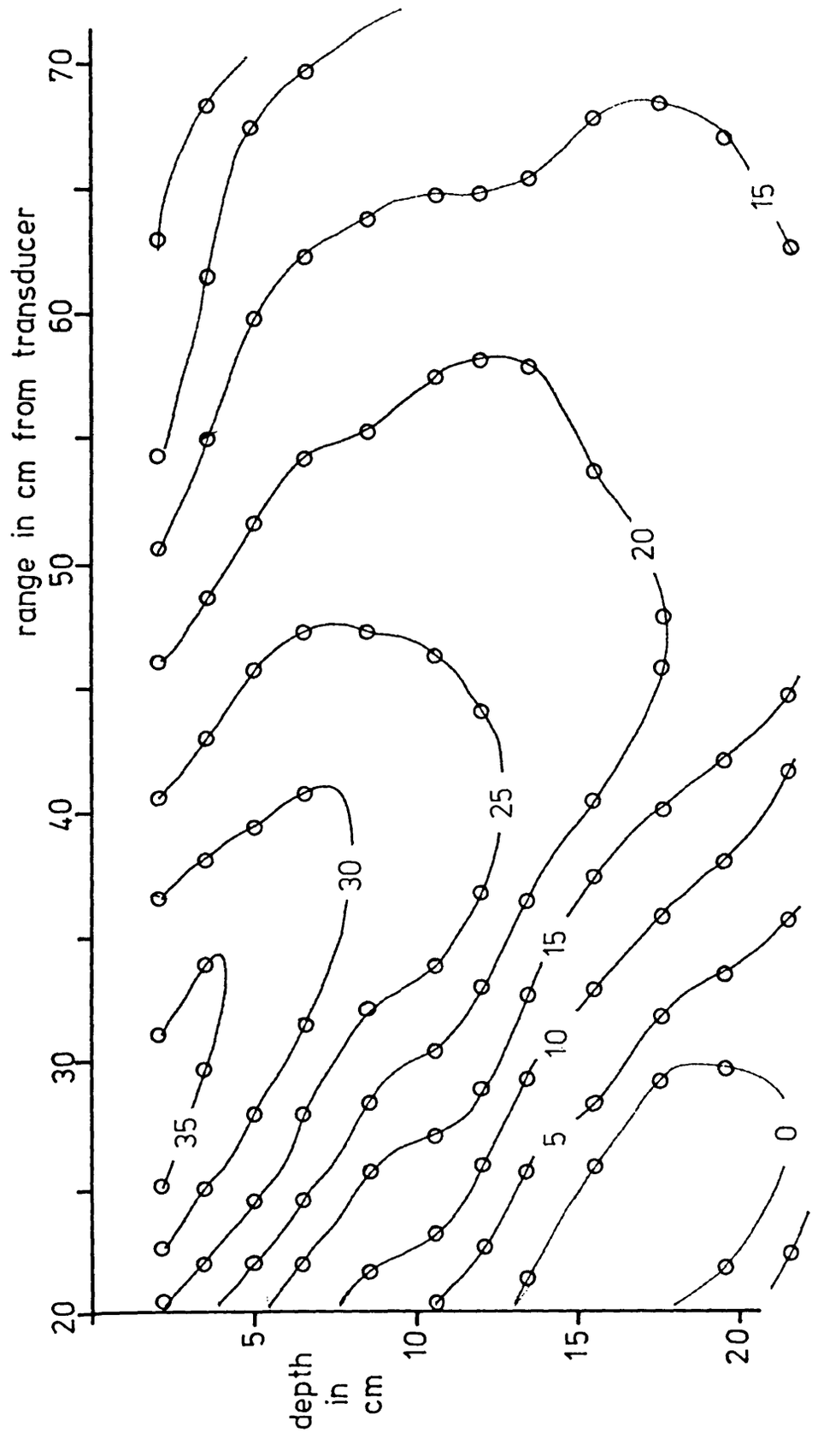

Figure 33 The measured secondary pressure contours [dB re 10^{-6} Y Pa] in the sediment in the plane of the beam when the array incident angle is 50°. O: measured location of a 5 dB contour.

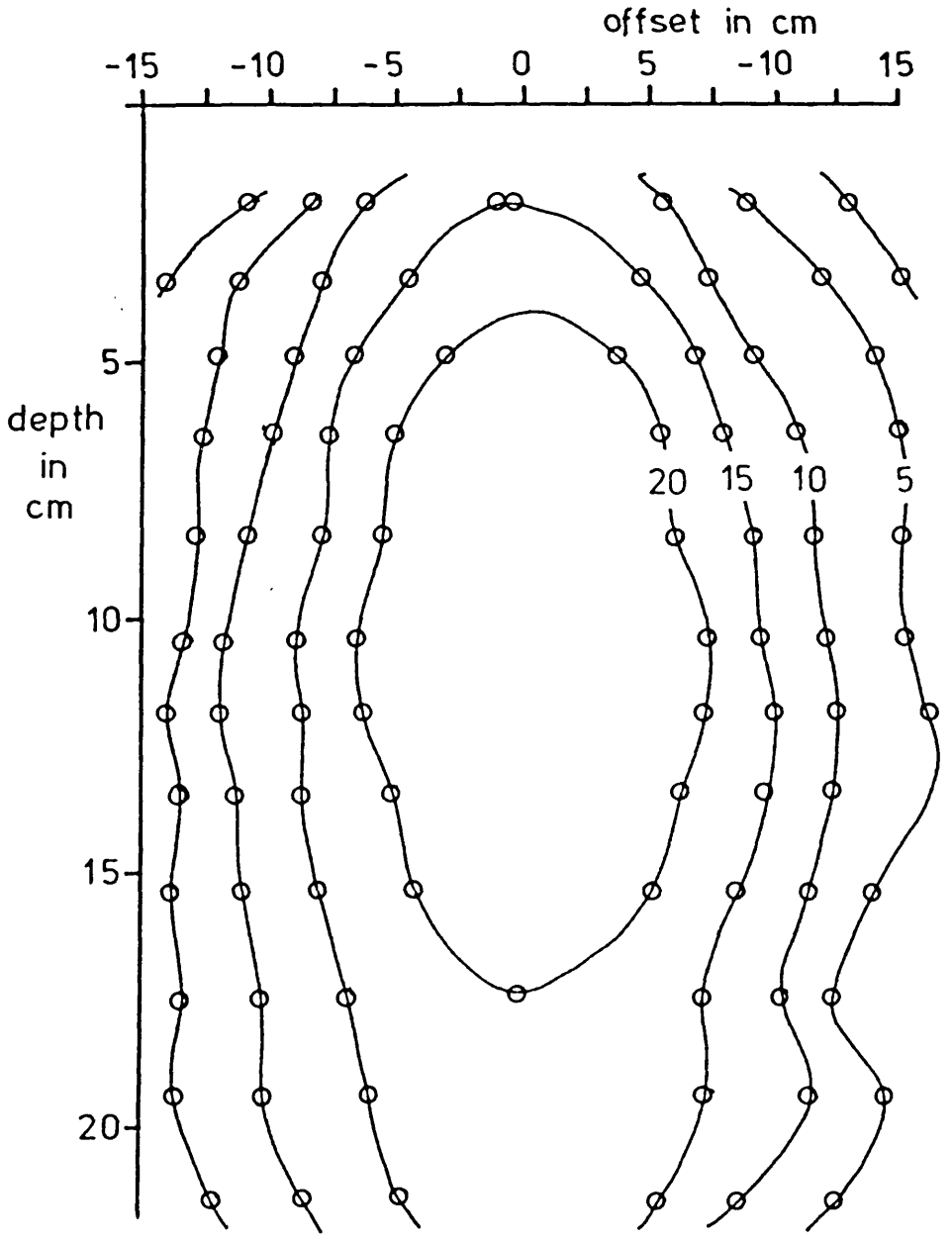

Figure 34 The measured secondary pressure contours [db re 10^{-6} γ Pa] in the sediment in the plane x = 50 cm when the array incident angle was 50°. O: measured location of a 5 dB contour.

of Figure 34 with Figure 31 shows. In addition, the farfield expressions diverge only slowly from the measured values as the field point approaches the truncation, so that, as a first approximation, the farfield calculation may be used close in to the truncation.

Postcritical incidence: $\alpha = 70°$

The pressure was measured in the planes $y = 0\,m$ and $x = 0.7\,m$ at a postcritical angle of primary beam incidence, $\alpha = 70°$, and contour plots drawn in the manner described previously (see Figure 3 for the geometry). The pressure contours in the plane $y = 0\,m$ are shown in Figure 35, the contours in the plane $x = 70$ in Figure 36. These figures may be compared directly with Figures and .

Qualitatively, the comparison is good, particularly in the following aspects:

(i) in the axial plane, Figure 35, the main region of penetration is limited to an angular fan, centred at the truncation, bounded by the interface and a line dipping at 25° (say) to the interface;

(ii) behind and below this line the contours are slowly varying and dip only very gently into the sediment;

(iii) the main "beam" dips at an angle of 75° to the vertical;

(iv) close to the interface the contours turn horizontal, and maxima and minima appear at shallow depths;

(v) the "beam" cross-section, Figure 36, is strongly top-bottom asymmetric; and

(vi) the "beam" width is narrower than in the subcritical case.

Quantitatively, the agreement is poorer. At depths greater than 0.15 m the contours become confused and the theory provides only the roughest estimate of their amplitude. At more shallow points in the plane, the agreement is rather better, but generally only to within $\sim$3-4 dB. Once again, though,

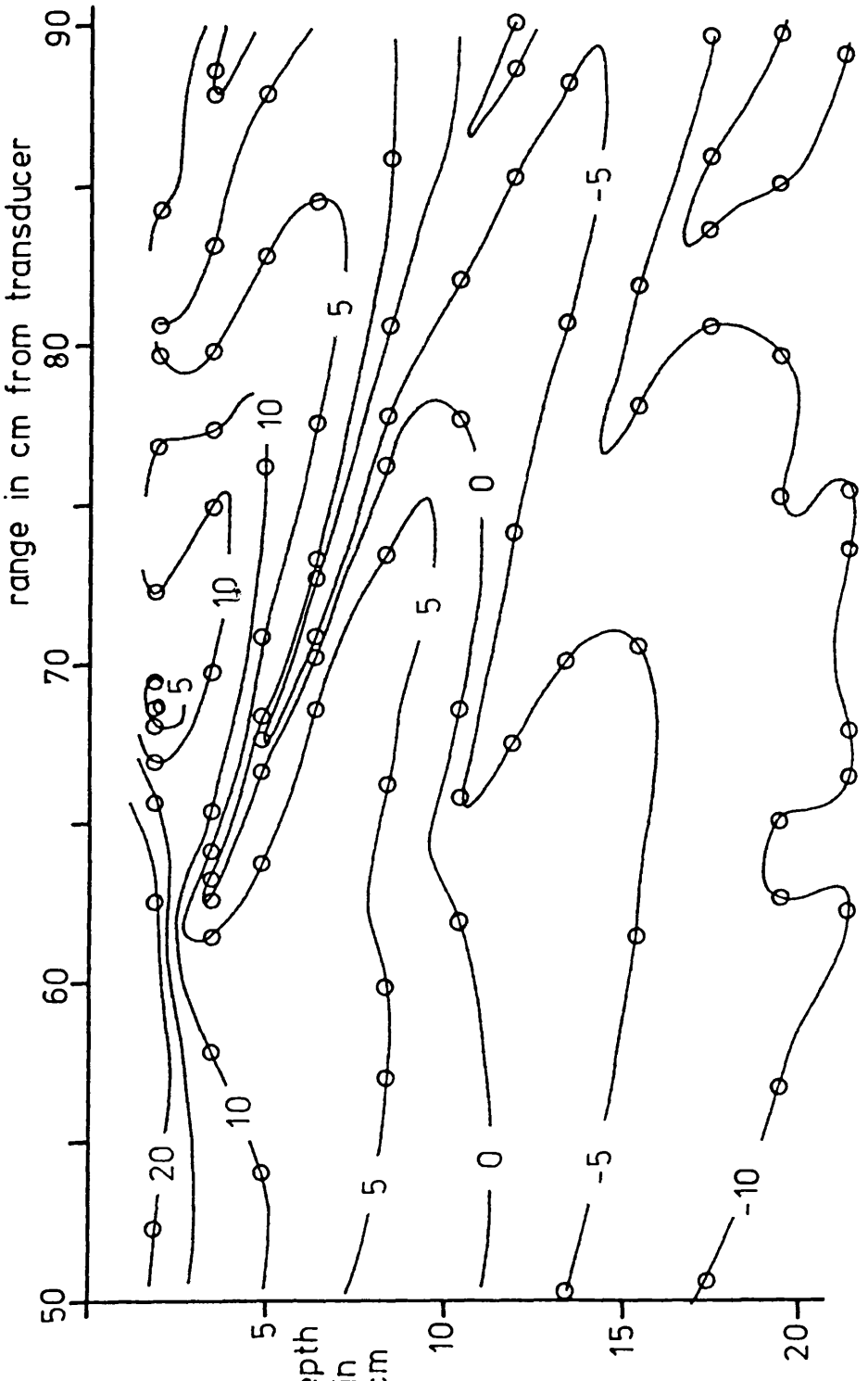

Figure 35 The measured secondary pressure contours [dB re 10^{-6} Y Pa] in the sediment in the plane of the beam with an array incident angle of 70°. O: measured location of a 5 dB contour.

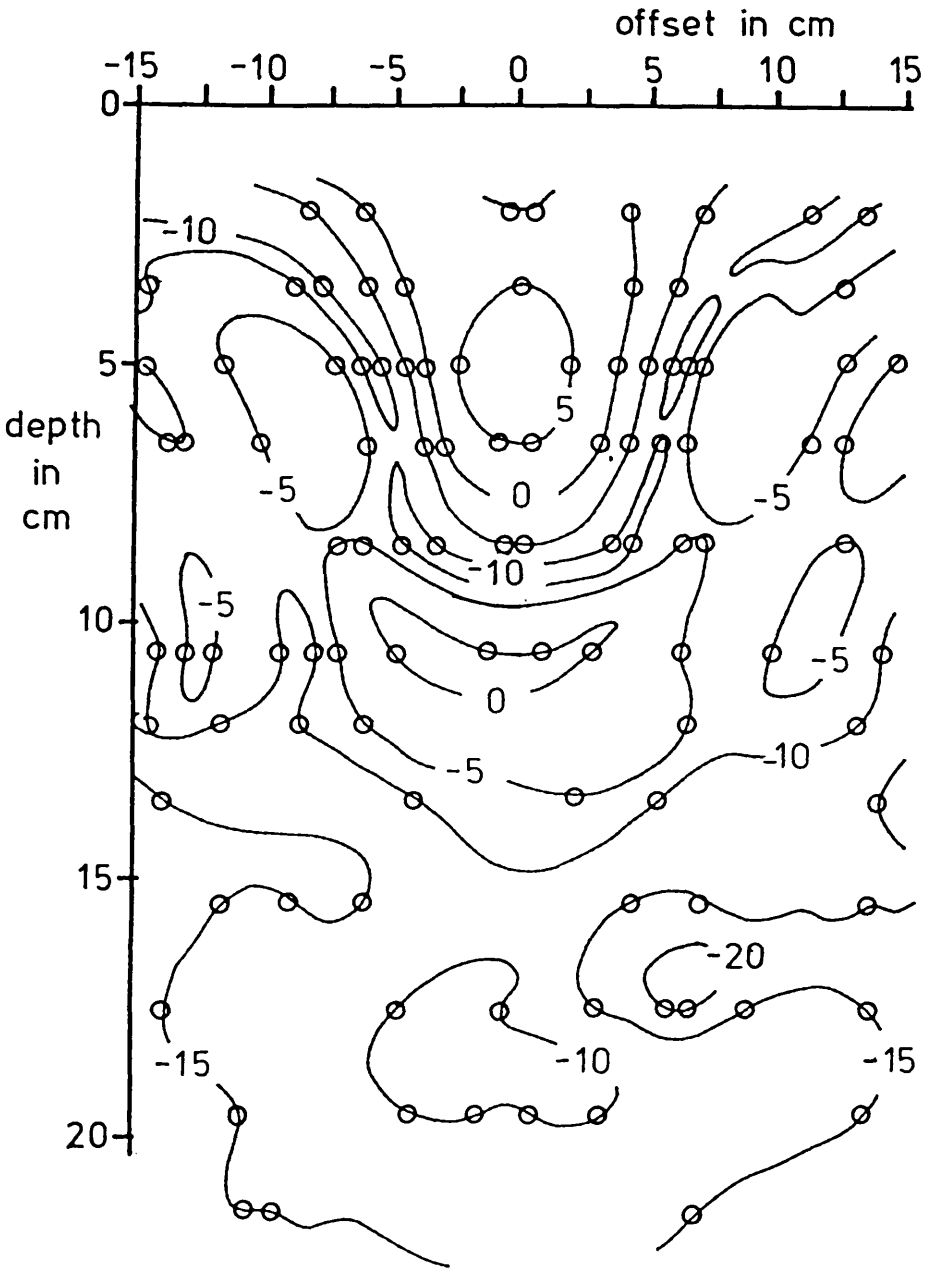

Figure 36 Measured secondary pressure contours [dB re 10^{-6} Y Pa] in the sediment in the plane x = 75 cm when the array incident angle is 70°. O: measured location of a 5 dB contour.

these remarks hold good for field points well inside the theoretical limits for the validity of the farfield expressions [equations (3.29)-(3.32)].

The agreements, (i)-(iv) above, are enough to demonstrate that the theoretical model is substantially correct. The slowly varying contours behind the truncation are associated with the transducer arrival. They are slowly varying because the transducer is some way distant; they are nearly horizontal because the incident angle associated with the transducer (see Figure 3) is well off the array axis. As the field point comes forward of the truncation, so the truncation arrival starts to interfere with the transducer arrival. The detail of the sidelobes is different in theory and practice; but this was anticipated from the results in water. However, the major lobes are correctly positioned. A comparison of Figure 31 (the beam cross-section in water), with Figure 35, shows how the importance of the truncation arrival is emphasised relative to the transducer arrival by the differential "spherical spreading" at the interface. In the former case it was not large enough to cause sidelobes, in the latter it is big enough completely to cancel the transducer arrival.

The asymmetry of the beam cross-section in Figure 36 serves to emphasise the remarks made in the theoretical discussion concerning the "incident" angle of the truncation arrival; the top half of the beam has been removed. It is because only the lower half remains that the beamwidth has been reduced by the interface.

The contours turn horizontal as the hydrophone approaches the interface, and interference patterns are found at shallow depths. These can be ambiguously interpreted. Close to the surface, hydrophone/surface/hydrophone reflection paths may become important. Certainly the interference maxima and minima seen in Figure 35 could be caused by just such reflections. This ambiguity could be removed if the arrival times of the interfering components

could be established, and later in the chapter an experiment which does just this is described. The noticeable feature of the growing pressure as the field point approaches the surface is that the theoretical prediction grows faster from a shallower depth. This is easily ascribed to the finite width of the hydrophone, effectively integrating over a depth of ∿1 cm.

The secondary field in sediment with varying angles of beam incidence

The field in sediment as a function of beam incident angle α was investigated at fixed locations in the sediment at a difference frequency of 100 kHz. The geometry of these experiments is shown in Figure 37. Three locations were chosen so that the "line-of-sight" to the shallowest depth, 2 cm, was well postcritical (74°), and the two other locations were chosen so as to examine how the field changed with depth. Figure 39 shows the results at the three depths d = 0.1 m, 0.06 m and 0.02 m, and range x = 0.75 m (y = 0 m), together with the theoretical predictions from equations (3.21) and (3.25). In the case of 2 cm burial, the theory has only been plotted up to α = 68°; beyond this angle the field can in no respect be described as 'farfield'.

The figure shows how, as the field point becomes shallower, the maximum pressure occurs at higher angles of incidence, and in addition, the pressure at lower angles of incidence is reduced. In fact, as the depth decreases, the whole weight of the pressure distributions moves towards higher angles of incidence. This is a very neat demonstration of how, as the field point gets closer to the truncation, the transducer arrival is reduced by the effects of "spherical spreading" and the truncation arrival is increased. The asymmetry of the main beam is a combination of this effect with the increasing secondary source volume as α increases. However, although in all cases the maximum pressure is postcritical, it is important to stress how shallow the effects are. The variation at 10 cm depth is not much different

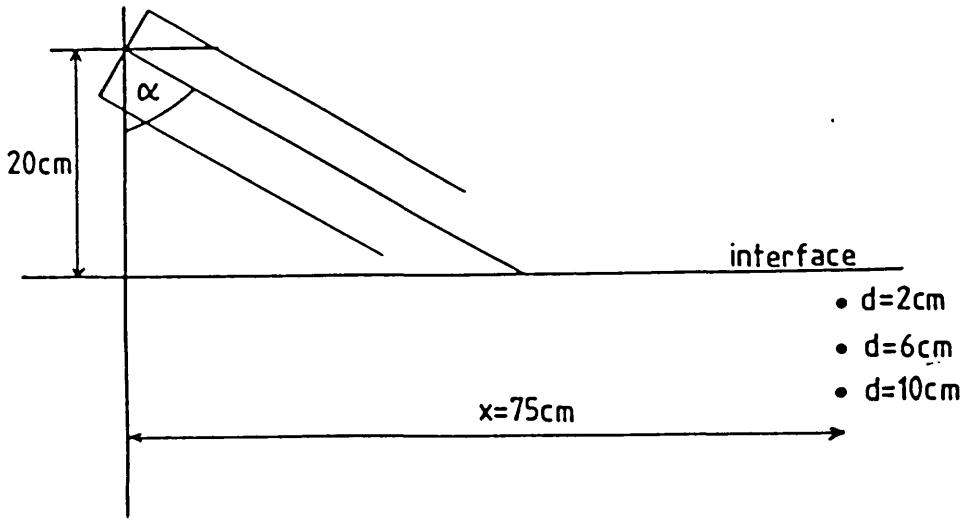

Figure 37 The geometry of the three hydrophone locations for the fixed location experiments.

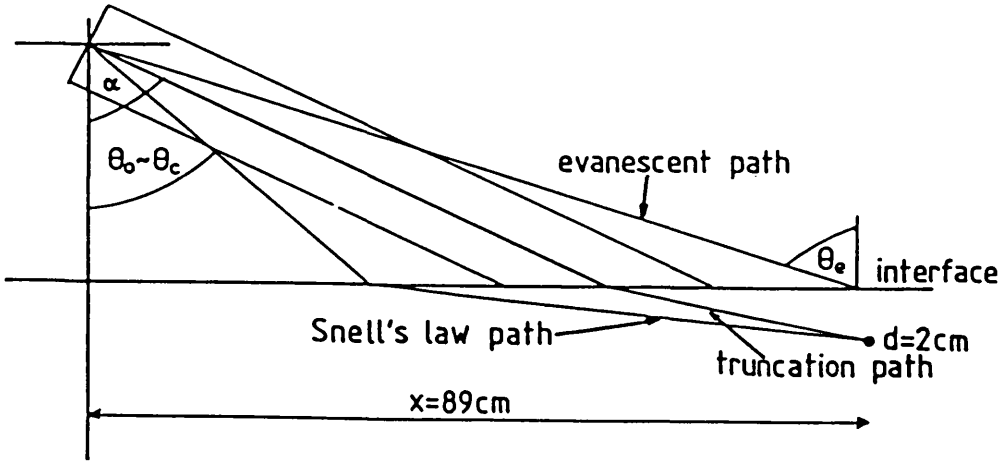

Figure 38 The geometry and associated raypaths for the pulse experiment to distinguish the evanescent arrival.

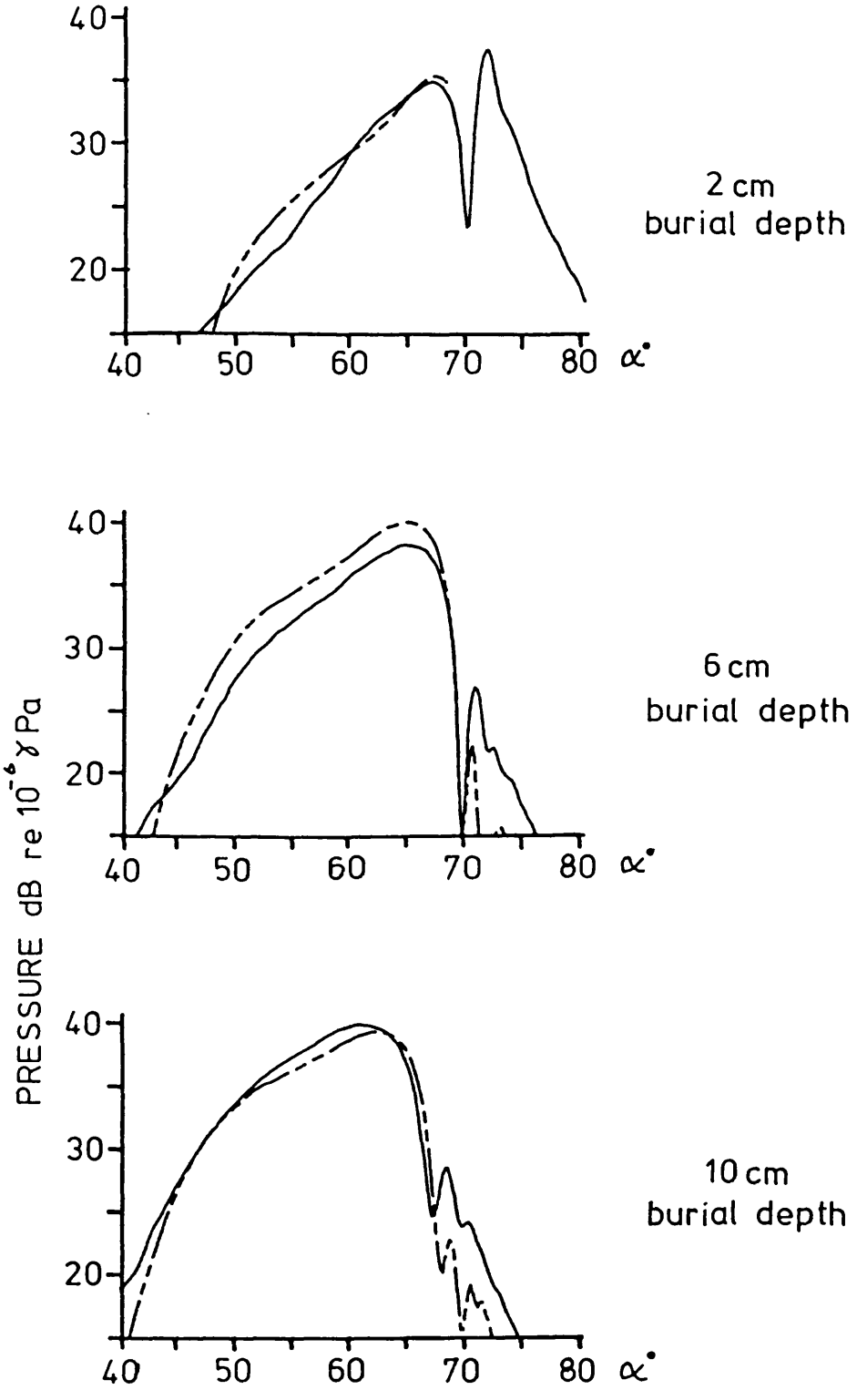

Figute 39 The measured secondary pressure in sediment at the three locations shown in Figure 37 as a function of beam incidence angle. ———: equations (3.21) and (3.25); - - -: experiment.

from a conventional beam. Only at the shallowest depths, where the spherical spreading advantage of the truncation arrival is not offset by its directional disadvantage, is there any real gain over a conventional beam.

Pulse investigation of the shallow arrivals

Theoretically, the evanescent arrival is expected to be dominant near the interface and the single difference frequency experiments produced evidence that this was indeed the case. The results were ambiguous though, because reflections between the hydrophone and the interface could have (somehow) been responsible for the observed effects. To remove this ambiguity, an experiment with short pulses was carried out, so that various arrivals could be identified by their arrival time.

The geometry of the experiment is shown in Figure 38. It was chosen so as to accentuate as far as possible the delay between the Snell's law arrival and the assumed evanescent arrival. The hydrophone was buried at $x = 0.89$ m, $y = 0$, and $d = 0.02$ m and the transducer was, as previously, 0.2 m above the interface. The array was driven in the pulse mode; the voltage waveform applied to the transducer was the form in equation (5.3). The waveform arriving at the hydrophone was recorded using the correlator for beam incident angles 60° to 90° in 0.3° increments.

In Figure 40, these traces are shown as a stacked plot. The only theoretical prediction that may safely be made is the arrival times of the pulses. The asymtotic solutions are not valid this close to interface; nor this close to the truncation; nor can they be used to predict the behaviour of wideband signals. Therefore, the arrival time diagram shown above the traces in Figure 40 [calculated from the stationary point equations (3.22) and (3.24)] makes no prediction as to the amplitude of the various arrivals, or even their existence.

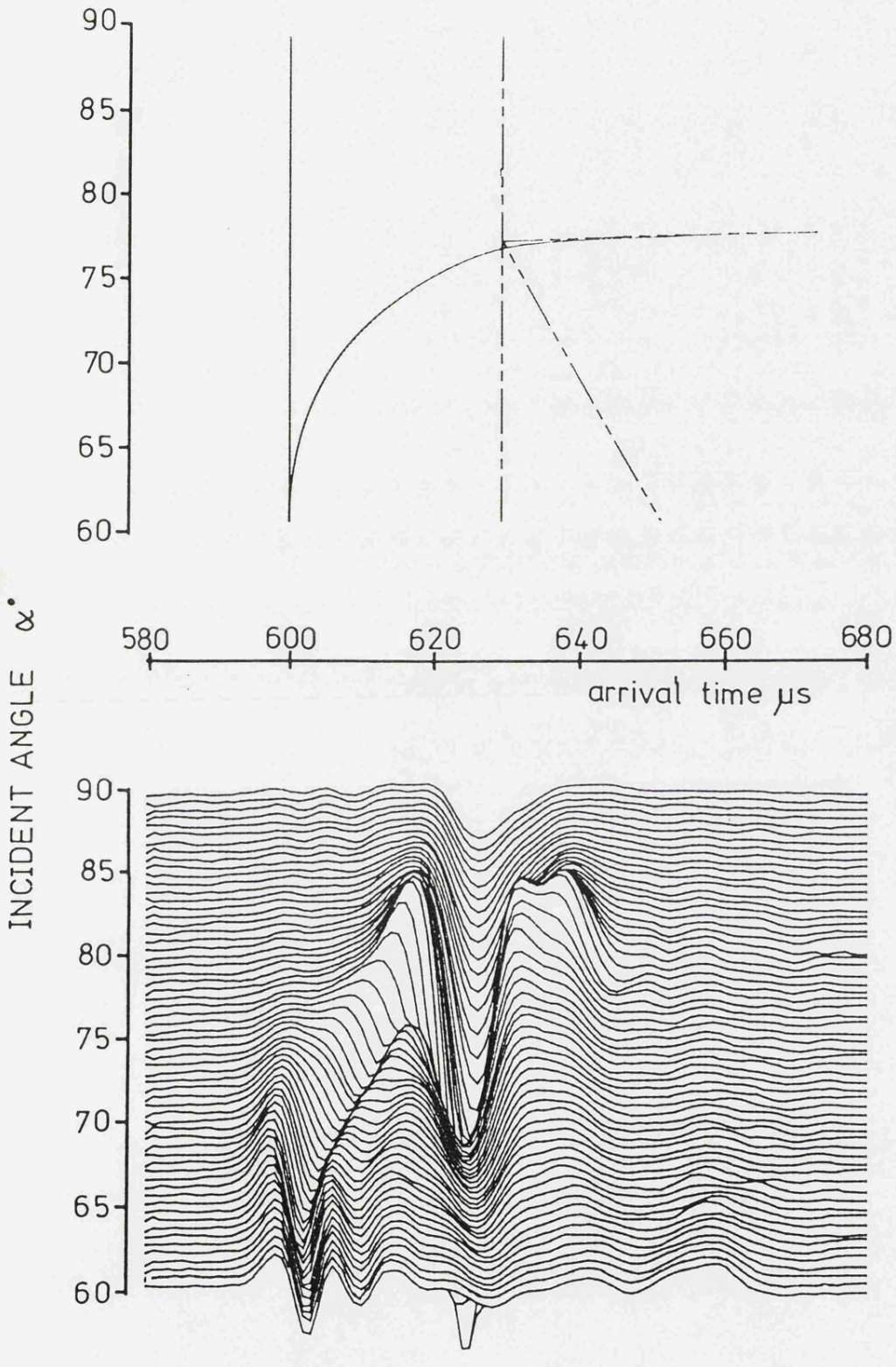

Figure 40 The pulse arrivals in the sediment at the location shown in Figure 38 as a function of beam incidence angle, together with the theoretically predicted arrivals. ———: Snell's law arrivals from the transducer and truncation: — — — —: evanescent arrivals from the transducer and truncation.

It may help in interpreting this figure to review Figure 38, which has a diagram of the relevant raypaths. A useful rule is that arrivals associated with the transducer are stationary in time, arrivals associated with the truncation have a move-out associated with its changing geometry. In Figure 40, there are two arrivals which are stationary in time. The first, at 600 μs, is rather weak and dies out as α approaches 70° of incidence. The second arrival, at 622 μs, is barely visible at 60° of incidence, but grows to a maximum at 78°, dying away as α tends to 90°. In addition to these two stationary arrivals is a third, which breaks away from the first arrival at 68°, and wings across the second arrival at 78°, where it, too, has a maximum. It then rapidly dies away, so that, by 83°, it has disappeared.

Comparison with the arrival time diagram allows easy recognition of the arrivals. The first and second arrivals are the Snell's law and evanescent arrivals from the transducer; the third arrival is the Snell's law arrival from the truncation. This interpretation is additionally supported by the amplitude information. The first arrival reflects the well-off-axis directivity of the transducer aperture. The evanescent arrival reflects the directivity of this aperture through its main beam, and has its maximum when the beam axis coincides with the evanescent raypath (*i.e.*, $\alpha = \theta_e$). The truncation arrival may be expected to have its maximum when the truncation is just above and in front of the hydrophone. But this is (almost) when $\alpha = \theta_e$, so this maximum should conicide with that of the evanescent arrival, which it does. Once the truncation has passed overhead of the hydrophone, its directivity ensures the rapid demise evident in Figure 40. [There was a possibility that, with the hydrophone this shallow, primaries could be responsible for this maximum through reception non-linearity. However, even at normal incidence, the primary level would be -13.5 dB down on

those in water. From the previously estimated second order sensitivity $\tau_2(\omega_0)$, this would generate an equivalent secondary pressure some -33 dB relative to the levels in Figure 40.]

There does not seem to be an evanescent arrival associated with the truncation aperture. As discussed in Appendix B, there are good theoretical grounds for assuming that this arrival would be reduced in amplitude relative to the transducer arrival. It is hard to make definite remarks, because of the difficulty of the mathematics.

CHAPTER 7

Discussions and Conclusions

The various theoretical and experimental results described in earlier chapters have each been followed by a discussion of their particular significance. In this conlcuding chapter a review of the main results and conclusions is given, their limitations and future extension are considered, a retrospective eye is cast over previous work in the field in the light of the present theory, and the chapter is completed with some general conclusions.

Review of the present work

The aim of this investigation was two-fold. Firstly, to provide a theoretical explanation of the properties of a parametric beam penetrating a water sediment interface, particularly at postcritical angles of incidence where its behaviour differs sharply from that of a conventional beam. Secondly, to compare quantitatively these theoretical predictions with the measured field in sediment so that the theory's practical usefulness can be tested.

The theoretical development started with the general integral solution in an infinite medium to Westervelt's scattering equation, equation (1.1). This integral was manipulated into a form which allows the inclusion of an arbitrary source distribution, and which was extended quite naturally to cover the presence of the interface and the sediment. A general, but formal, solution to the problem followed in the form of a double inverse Fourier transform, whose kernel, the plane wave spectrum, remained to be calculated for any particular case.

Unlike previous theoretical descriptions of this problem, in this study the effect of the interface on the virtual source distribution was explicitly acknowledged, and the problem of calculating the plane wave spectrum of the modified, or truncated, source volume fell naturally into two cases: depending on whether the primary field (and hence virtual source volume) was incident upon the interface in its nearfield or its farfield. Having made this calculation, the spectrum was substituted into the inverse Fourier transform and the high frequency farfield in the sediment was calculated by stationary phase and steepest descent integration.

In the case of nearfield truncation, the resulting integral for the plane wave spectrum was simple enough to be integrated explicitly, and a detailed picture of the secondary farfield could be given. The field in sediment was found to be equivalent to two apertures, a circular one lying at the transducer face, and an elliptical, phase shaded aperture, which has no analogue in the primary field, lying at the intersection of the primary beam and the interface.

At a fixed subcritical angle of incidence, the secondary field in sediment is similar to that of a conventional beam. However, the maximum pressure at a particular location in the sediment does not occur when the primary beam is coincident with the Snell's law path from the transducer to that point; but at an angle of incidence rather greater than the Snell's law angle. This effect is caused by the increasing volume of secondary sources with beam incident angle, and by the decreased spherical spreading from the truncation aperture to the field point.

At some angle of primary beam incidence angle sufficiently greater than critical, the secondary field is equivalent to the combination of the arrivals from the two apertures, and results in a deeper penetration than in the conventional case. The directivity of the truncation aperture becomes less

favourable to penetration as the primary beam incidence angle becomes large, so that a small aperture is required to maintain penetration at high primary beam incident angles.

The case of farfield primary truncation is studied next; but the complexity of the integral forms for the plane wave spectrum make it impossible to give such a detailed description of the secondary farfield as was possible in the case of nearfield primary truction. However, it is possible to determine that the secondary farfield will essentially consist of contributions from the nearfield of the primaries and from the truncation. An asymtotic solution to the plane wave spectrum of the truncation contribution is obtained and used to demonstrate an important conclusion: the behaviour of the parametric array will not differ qualitatively from a conventional array if the truncation of primaries occurs at a range from the transducer exceeding $R_0\omega_0/\omega$. This limit is that already noted by Mellen and Moffet[19] to mark the point at which the secondary field in water may be regarded as spherical waves.

This concludes the theoretical investigation and it is followed by a description of the experimental investigation of the secondary field in sediment from a nearfield truncated parametric array. The qualitative agreement between the results of these experiments and the theoretical predictions is very good; so good that the physics of postcritical penetration of parametric arrays no longer seems in doubt. There is, especially at high angles of primary beam incidence, quantitative disagreement in detail. These discrepancies are explained by the approximations made to the primary field in its nearfield, and by the considerable acoustic variability of the sediment. These are differences in detail only; the broader characteristics of both sub- and post-critical penetration are well accounted for.

At subcritical angles of incidence, these characteristics are similar to a conventional beam. At postcritical angles of incidence, the field in sediment is determined by the relative importance of the transducer and truncation apertures. The strength of an arrival from an aperture depends on the directivity of the aperture, and the absorption, spreading and refraction loss along the raypath. The relative importance of the two arrivals is therefore a strong function of geometry. As a result, at postcritical angles of incidence the secondary field in sediment may be divided into three regions:

(1) behind and below the truncation the field is due almost entirely to the transducer, and is similar to the field of a conventional postcritical beam with slowly varying horizontal contours;

(2) in front of the truncation and lying within an angular fan centred on the truncation, the field is due to the interfering arrivals from the truncation and transducer, giving a more oscillatory higher pressure contour than a conventional beam; and

(3) very close to the interface, the field is dominated by the evanescent arrival. This region is bounded on its lower side by interference minima and maxima indicating the Snell's law and evanescent arrival have equal magnitudes.

The interpretation of these shallow maxima and minima was confirmed by the short pulse experiments which time resolved the secondary field into its components. The arrival time of the Snell's law and evanescent waves was in good agreement with the theoretical prediction based on the steepest descent calculation.

Limitations and future work

The major limitation of the theory presented here is the obvious one: it has not been possible to make quantitative remarks concerning the nearfield

of the secondary field. This is not surprising. As was noted in Chapter 4, the considerably simpler nearfield problem of a piston radiator still awaits a solution. It is an omission of some importance, however, because this region is just that region which previous investigators were, and future sonar users may be, interested in. Predicting the pressure in this region would seem to be a numerical problem. The refraction problem close into the interface would make this a calculation of some size, considerably more complicated than Zemanek's[36] equivalent calculation of the nearfield of a piston radiator.

Time has prevented an experimental investigation of the case of farfield truncation* and there are no reports in the literature of such an investigation. This is a pity, because the present theory is only able to calculate the pressure in the sediment when the result is of little interest, *i.e.*, when the range of the truncation from the transducer exceeds $R_0\omega_0/\omega$. The complexity of the integrals would make the calculation of the pressure variation near the interface when the truncation lies between R_0 and $R_0\omega_0/\omega$ an unwieldy task.

It is the author's suspicion that the significant range of truncation distance is considerably less than $R_0\omega_0/\omega$. This comment is based on the observation that stationary phase approximations, on which the limit $R_0\omega_0/\omega$ is based, often work well outside their theoretical range of validity. As evidence for this, compare Figures 33 and 5. The stationary phase approximation, Figure 5, is seen to produce tolerable estimates of the measured pressure, Figure 35, well into the nearfield of the array. This behaviour is helped by the long wavelength of the secondary field in comparison with the

*Such an investigation is in hand at the time of writing. It is hoped the results will be made available in the open literature at some later date.

truncation aperture dimensions. Confirmation of this suspicion is well suited to an experimental investigation in which the variation of pressure with incident angle is observed as the value of $R_0\omega_0/\omega$ is changed.

This study has not concerned itself with the reflected secondary field, although the formal development of the farfield solutions lends itself just as easily to the reflected field as it does to the transmitted field. It has not been pursued because the primary field may no longer be dealt with simply. The reflected primary may no longer be ignored, and in addition, if the sediment is very lossy, or the incident angle postcritical, the secondary sources generated after the primary reflection will not be co-phasal with secondary sources generated by the incident primaries. The primary source volume is further complicated by the splitting in reflection of a postcritical primary beam into reflected and head waves, each generating its own secondary sources. In comparison, the account of the field in the sediment presented here is quite straightforward.

This simplicity has arisen because the truncation has been assumed sharp. With the particular ratio of primary to secondary frequencies in this study, this is a good approximation, as Pace and Ceen's experiments demonstrate.[13,14] At subcritical angles of incidence modifying the source volume to include an exponentially tapered transmitted primary beam (and, if desired, a reflected beam) would present no new theoretical difficulties. It would, however, be difficult to extend the present analysis to include a near- or post-critical transmitted primary beam, because it would no longer be describable by some simple geometric configuration.

Review of previous work: the secondary nearfield

In Muir *et al.*'s experiments,[2] the hydrophone was buried very close to the interface, which placed it in the nearfield of the truncation aperture.

As has just been noted, the present theory does not cover this case, except at very high incidence angles and frequencies. Yet this lack of an exact theory does not preclude some general remarks concerning the secondary nearfield, and earlier experimental and theoretical work provide a useful focus for this discussion.

Figure 41 is taken from Jarzynski and Flax's numerical account[12] of the penetration of a water sediment interface by a parametric array. The solid line shows the pressure measured at a shallowly buried hydrophone, with a geometry similar to that shown in Figure 37, from a parametric array incident on the boundary in its primary nearfield. (Jarzynski and Flax's second reference is ref. 3 in this thesis.) The dashed line is calculated on the assumption that the virtual source volume may be considered a line array. The calculated pressure differs from the measured pressure in three ways: the position of the main peak is misplaced by -4° of grazing angle, (grazing angle = 90° - incident angle); the minor peak at a grazing angle of ∿26° in the measured pressure is entirely absent from the theoretical calculation; the maximum pressure levels shown in the table above are overestimated by 9 dB. Comparison of this figure with Figure 39, which shows the result of a similar experiment at three different depths, makes it immediately apparent that all three errors can be attributed to the line array approximation.

The minor peak in Figure 41, rather arbitrarily assigned by Jarzynski and Flax as being due to attenuation, is recognisable as the main beam, and the main peak as a sidelobe whose importance is emphasised by the closeness of the truncation aperture. Acknowledging a finite aperture in the calculation would reduce the importance of the sidelobe both absolutely and relative to the main beam. The phasing of the aperture would also tend to reduce the angle of incidence at which the peak pressure occurs. The earlier discussion (Chapter 3) of the high angle nearfield emphasised how irrelevant to the total

TABLE I. Measured and calculated peak levels of the difference-frequency sound in the sand sediment. Also included are values of the array grazing angle at which the sound peak occurs, and the frequencies $f_{+,-}$ and pressure levels $p_{+,-}$ of the primary beams.

f_+ (kHz)	f_-	p_+ (dB re 1μPa)	p_-	Peak pressure level (dB re 1μPa)		Array grazing angle	
				Measured	Calculated	Measured	Calculated
210	205	214	215	140	143	15.5	13.3
205	195	215	214	143	146	16.0	13.6
210	190	214	213	137	146	15.5	13.6

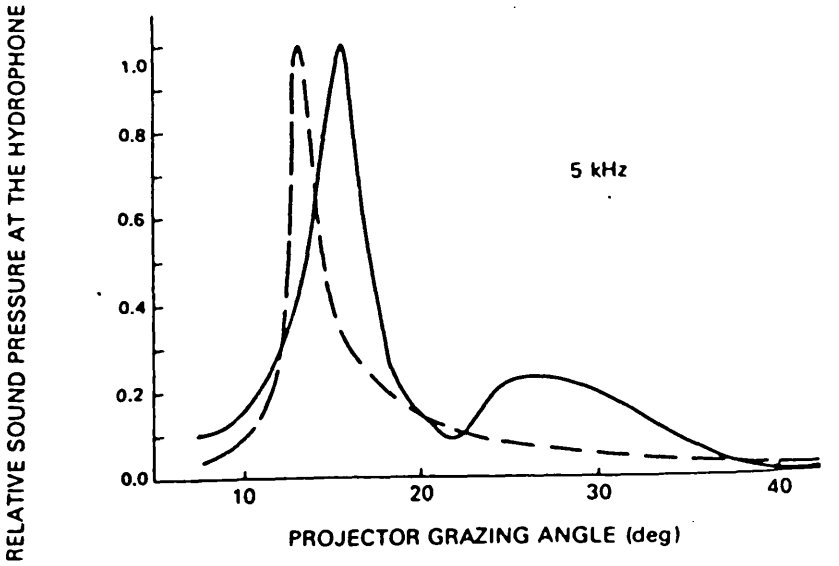

FIG. 3. Sound pressure in the sand sediment insonified by a parametric array. ——: experimental data of Ref. 2; – – –: calculated values.

Figure 41 [From Jarzinski and Flax, *J. Acoust. Soc. Am.*, 1978, 63(5), 1365.][12] This figure compares Muir's[3] experimental curves with Jarziniski and Flax's numerical calculations based on a line array model of the primaries.

field the closeness of the truncation aperture is if the sources are sufficiently out of phase. The phase difference across the aperture increases with incident angle: thus, the predicted maximum pressure of an array with finite aperture will occur at a smaller incident angle than for a line array.

These arguments, which account for the differences between the measured and predicted pressures in Figure 41, are strictly only applicable to the farfield. Directivity, for example, is not meaningful in the nearfield. It is clear from this discussion, however, that qualitatively the behaviour of the nearfield may be understood in these terms. We are no doubt helped by the characteristic low value of kR for parametric arrays.

The tendency of the truncation aperture to reduce the angle of incidence at which the maximum transmitted pressure at a particular location occurs has also led to what I suspect is the incorrect identification of beam displacement. The phenomenon of beam displacement is shown in Figure 42, which is taken from Muir *et al.*,[2] the paper used to introduce this thesis. The displacement is the discontinuous horizontal shift of the axis of the beam between incident and transmitted beams at the interface. The authors report a displacement of "approximately one foot" and measure the velocity of the beam over the displacement to be the same as the compressional wave velocity in the sediment.

This displacement is half a secondary beam width. The experimental measurements of Figure 35 also appear to exhibit a shift of similar magnitude: if the "main beam" is extrapolated back to the interface, it intersects at around x = 60 cm. However, these measurements are consistent in the farfield with the present theory, which explicitly assumes the displacement to be zero. In the farfield at least, this shift may be explained by virtue of aperture phase alone.

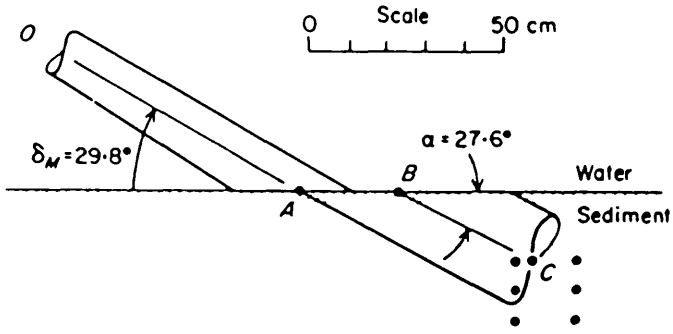

Figure 11. Displacement and half power angular response limits of the beam at the interface.

Figure 42 [From Muir, Horton and Thomson, *J. Sound Vib.*, 1979, 64(4), 539.][2] This figure illustrates the nature of displacement and is scaled to agree with the half power measurements of Muir *et al.*

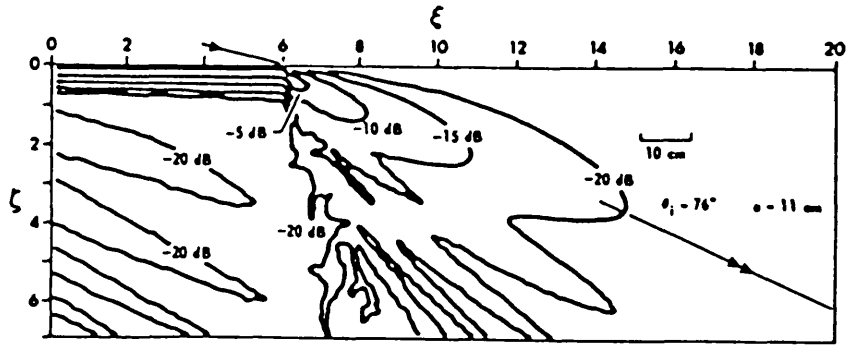

FIG. 8. Constant pressure amplitude curves in the plane of incidence

Figure 43 [From Tjotta and Tjotta, *J. Acoust. Soc. Am.*, 1981, 69(4), 998.][9] This figure shows the pressure contours in sediment due to a phased shaded elliptical spot lying between $\zeta = \pm 6$, *i.e.*, $\zeta = 0$ is the spot centre. The apparent "displacement" is quite clear.

Some insight into the behaviour of the nearfield may be gained from Tjotta and Tjotta's study [9] of a phase shaded elliptical aperture, briefly reviewed in the introduction. As noted in Chapter 3, this aperture has many similarities with the truncation aperture of the present theory, provided the cross-sectional radius of the secondary beam in water is replaced with the transducer radius. Figure 43 shows the calculated pressure contours in the vertical plane in the sediment containing the array axis. The centre of the primary beam is incident at $\zeta = 0$; the arrow incident at $\zeta = 6$ marks the edge of the secondary incident beam. In this case the beam axis again appears to be displaced by at least half a beam width. (The strange behaviour of the contours at $\zeta < 5$ is due to the parabolic approximation used by Tjotta and Tjotta, which anticipates zero wavefield in this region.) Tjotta and Tjotta's theory also explicitly excludes displacement* by virtue of the treatment of the boundary. These results, too, may be explained by aperture phase alone. In summary, the evidence for the displacement of a narrow beam on transmission is, at the least, ambiguous; and the use of a parametric beam, truncated by the interface in its primary nearfield, to investigate the phenomenon is likely to confuse, rather than clarify, the issue.

Conclusions

The purpose of this project was theoretically and experimentally to investigate the penetration of parametric beams into sediment and in particular, to understand the circumstances in which the parametric field in sediment differs from that of a conventional beam.

---

*Tjotta and Tjotta do actually refer to the shift seen in Figure 43 as "displacement". This is loose use of the terminology. Here, and in references 3 and 7 it is used in the precise sense defined by Brekhovskikh. The distinction has importance. In this more precise sense "displacement" refers to behaviour inexplicable in terms of geometrical optics.

The field from a conventional beam obeys Snell's law. In order to penetrate the sediment, it must have an incident angle less than critical, and when the incident angle is near critical, the transmitted beam suffers severe refraction loss. For this reason, a conventional beam has difficulty in insonifying regions in the sediment which lie at large horizontal distances from the source. In contrast to this behaviour, when a parametric beam is incident on a water sediment interface, the maximum pressure at large horizontal distances from the source occurs at angles of beam incidence greater than critical. The characteristic features of a parametric beam are its narrow beamwidth and distributed source volume.

The results presented in the thesis make it clear that the unconventional behaviour of parametric beams is due to the extended distribution of virtual sources above the interface. The truncation of the source distribution gives rise to a truncation aperture lying at the interface, and this aperture, which has no analogue in the conventional case, provides an additional path by which energy may cross the interface. It is this additional contribution to the field in the sediment which gives rise to the anomalous postcritical behaviour of parametric beams.

It is not sufficient merely to have secondary sources close to the interface in order to produce high postcritical pressures in the sediment. The source must also be suitably phased. Too large a phase difference across the truncation will result in poor penetration. When the array is truncated in the nearfield of the primary beam, this phase difference may arise as the result of too high an incident angle. If the array is truncated in the farfield of the primaries, this phase difference results from the spherical spreading of the primaries. At truncation ranges greater than $R_0 \omega_0/\omega$, the spherical phase lagging of the virtual sources is sufficient to prevent postcritical penetration. Increasing the secondary frequency will accentuate

phase differences which result from the temporal and spatial distribution of the virtual sources. Thus: narrow primary beams aid penetration; narrow secondary beams restrict it.

The field in sediment from a truncated parametric array is complicated. When the primaries are nearfield truncated at the interface, the field in the sediment results from the interferance of arrivals from transducer and truncation, giving rise to rapidly oscillating pressure contours. The amplitude of the arrivals from each end of the volume is a function both of the directivity of each aperture, and the refraction loss along each path. The refraction loss is a strong function of angle at large angles of transmission, so that the secondary field varies strongly with depth. As the truncation moves into the farfield of the primaries, so the importance of the truncation arrival is diminished, together with, it is expected, the complicated interferance pattern; but only at the cost of reduced postcritical penetration.

The complicated nature of the secondary field also makes it difficult to provide useful non-dimensional guides as to its performance. This is partly ture of parametric arrays in general; Mellen and Moffett[19] required three dimensionless constants to describe the secondary farfield in water. It also reflects the difficulty in non-dimensionalising the depth/angle/secondary wavelengths which are so important to the field in sediment.

In his review of the applications of parametric beams to underwater sonar,[50] Konrad remarks that the good penetration and high resolution, both spatial and temporal, of parametric beams may make sub-bottom profiling their most important task. They have certainly been used very successfully at normal incidence where their wide bandwidth makes them particularly useful.[51]

The results in this thesis undoubtedly have helped to understand the behaviour of parametric beam 'sub-bottom', and to provide expressions to calculate their field under certain restrictions. However, the difficulty in providing a wider quantitative picture, or providing general rules to achieve certain specifications, makes Konrad's prophesy no more certain. It remains to be seen whether a successful application will be found.

APPENDIX A

Details of the Asymtotic Solution to Equation (3.15)

In the following discussion those elements of the asymtotic solution to equation (3.15) which are in addition to the published discussions[27,33] of the point source problem are detailed.

The discussion will be limited to the first of the two terms in the integrand of equation (3.15), bearing in mind that a similar description applies to the second. Denoting this term I_s^t, from equation (3.15),

$$I_s^t = \int_0^{\pi/2+i\infty} B(\theta)d\theta \int_0^{2\pi} C(\theta,\phi)D(\theta,\phi)e^{-ik\Phi\sin\theta}d\phi \qquad (A.1)$$

where comparison with equation (3.15) allows $B(\theta)$ and $C(\theta,\phi)$ to be defined. The ϕ integral in equation (A.1) can be viewed as a complex integral with the contour running along the real ϕ axis from 0 to 2π in the complex ϕ plane. Noting that along this contour the phase of the exponential is real a stationary phase integration over ϕ is performed.

$D(\theta,\phi)$ has pairs of simple poles lying at $\pm\phi_p + m\pi$, ϕ_p imaginary, m any integer. As $\theta \to \alpha$, $\phi_p \to 0$, reaching 0 when $\theta = \alpha$. The phase has two stationary points $\phi_o, \phi_o + \pi$ on the contour given by

$$\phi_o = \tan^{-1}(x/y) \qquad (A.2)$$

There will be occasions, therefore, when a stationary point will be close to one pair of poles of $D(\theta,\phi)$, and a straightforward application of the stationary phase approximation would be incorrect, because $D(\theta,\phi)$ would not be slowly varying in the vicinity of ϕ_o. To deal with this problem $D(\theta,\phi)$ is factorised in the following manner

$$I_t^s = \int_0^{\pi/2+i\infty} B(\theta)d\theta \int_0^{2\pi} [C(\theta,\phi)D(\theta,\phi)(\phi-\phi_p)(\phi+\phi_p)] \frac{e^{-ik\Phi\sin\theta}d\phi}{(\phi-\phi_p)(\phi+\phi_p)} \qquad (A.3)$$

The function in square brackets in equation (A.3) is now a slowly varying function. Making the standard stationary phase approximation equation (A.3) becomes,

$$I_t^s \sim \int_0^{\pi/2+i\infty} B(\theta)C(\phi_o,\theta)D(\phi_o,\theta)\frac{(\phi_o-\phi_p)(\phi_o+\phi_p)}{2\phi_p} e^{-ik\Phi(\phi_o)\sin\theta}d\theta \ . \qquad (A.4)$$

$$\int_{-\infty}^{+\infty} \frac{e^{-is^2}}{(s-s_p)} - \frac{e^{-is^2}}{(s+s_p)} ds$$

with

$$s^2 = \frac{k\sin\theta}{2}\Phi''(\phi_o)(\phi-\phi_o) \qquad (A.5)$$

which integrates to (see reference 27, page 240).

$$I_t^s \sim \int_0^{\pi/2+i\infty} B(\theta)C(\phi_o,\theta)D(\phi_o,\theta)\frac{(\phi_o-\phi_p)(\phi_o+\phi_p)}{2\phi_p} i\pi e^{-s_p^2}. \qquad (A.6)$$

$$[\mathrm{erfc}(-is_p) - \mathrm{erfc}(+is_p)]$$

for each stationary point.

The contributions from each stationary point may be combined into one by extending the θ-contour to run from $-\pi/2-i\infty$ (instead of 0) to $\pi/2+i\infty$. Finally, in connection with the ϕ integral note that if $\phi_o-\phi_p$ is large, the error functions may be replaced by their asymtotic expansion

$$\operatorname{erfc}(z) \sim \frac{e^{-z^2}}{\sqrt{\pi}z}, \quad \text{large } z \tag{A.7}$$

and equation (A.6) may be manipulated into the form shown in equation (3.17).

The θ-integral may now be written

$$I_s^t \sim \int_{-\pi/2-i\infty}^{\pi/2+i\infty} [E(\theta,\phi_o)D(\theta,\phi_o)(\phi_o - \phi_p)(\phi_o + \phi_p)] \frac{e^{-ik\Theta(\theta,\phi_o)}}{2\phi_p} d\theta \tag{A.8}$$

where comparison with equation (A.6) allows $E(\theta,\phi_o)$ to be defined.

While deforming the contour of equation (A.9) into that of steepest descent any contributions from singularities of the integrand must be included. Apart from the branch cut due to the radical $(n^2-\sin^2\theta)^{\frac{1}{2}}$, which can be shown[27] to have no contribution, the integrand has a branch cut due to the term k_r in $E(\theta.\phi)$ and a pole due to ϕ_p.

The branch cut can be ignored because $J_1(k_rR)/k_r$ is a symmetric function of k_r taking the same values on either side of the cut. The poles of $D(\theta,\phi)$, which lie symmetrically about the real θ axis, are negated by the zero's of $\phi_o - \phi_p$ and $\phi_o + \phi_p$. The term in brackets is thus a smoothly varying function of θ and may be removed from the integral in the steepest descent approximation. ϕ_p is a function of θ but not ϕ_o and has a simple zero at $\theta = \alpha$ on the real θ axis. When the contour is deformed, the residue from this pole must be included, but it can be shown that it cancels with the residue from the truncation aperture term.

With these preliminaries completed, the contour is deformed and together with the substitution

$$s^2 = \frac{k}{2}\theta''(\theta_o,\phi_o)(\theta - \theta_0)^2 \tag{A.9}$$

the integration of (A.8) results in

$$I_s^t \sim \frac{2\pi k}{\Theta''(\theta_o,\phi_o)}^{\frac{1}{2}} e^{i\pi/4} E(\theta_o,\phi_o)D(\theta_o,\phi_o) \frac{(\phi_o - \phi_p)(\phi_o + \phi_p)}{2\phi_p(\theta_o)}$$

$$e^{-ik\Theta(\theta_o,\phi_o)} \tag{A.10}$$

If θ_o is not close to α the error functions may be replaced with their asymtotic expansion and equation (3.21) results.

As $\theta_o \to \alpha$ and $\phi_o \to 0$, the asymtotic solution equation (A.10) tends to the residue at $\theta = \alpha$ and the two contributions from each end of the array cancel exactly. In this case the alternative form equation (3.8) for the plane wave spectrum is used in equation (A.1). This is correct in those regions of the θ and ϕ planes that contribute to the integral, *i.e.*, around θ_o and ϕ_o. In this case there are no problems with additional singularities and equation (3.25) results. Thus, provided the plane wave spectrum is put in a suitable form, its singularities do not contribute to the integral.

APPENDIX B

The Contour of Steepest Descent

The purpose of this appendix is to discuss the contour of steepest descent associated with the integral

$$I = \int_{-\pi/2-i\infty}^{\pi/2+i\infty} F(\theta)e^{-ik\Phi(\theta)}d\theta \quad , \tag{B.1}$$

where the phase $\Phi(\theta)$ is given by

$$\Phi(\theta) = R\sin\theta + L\cos\theta + d(n^2-\sin^2\theta)^{\frac{1}{2}}, \tag{B.2}$$

and in particular, what happens when:

(a) R becomes large;

(b) $L \to 0$, and then

(c) $d \to 0$.

The most detailed published discussion of this contour is given by Gerjouy in the $u = \sin\theta$ plane.[33] The description of the contour is simpler in the θ-plane; it is in this plane that this discussion is framed. Its derivation is essentially similar to that of Gerjouy's, but is made simpler with a copy of Professor Berktay's notes on the subject.[54]

Figure B.1 shows the steepest descent contour, the contour of B.1, the branch cuts of $(n^2-\sin^2\theta)^{\frac{1}{2}}$ and the stationary points of Φ. Starting on the lower Riemmann sheet at $-\tan^{-1}(\frac{L+d}{R})-i\infty$ it crosses into the 4th quadrant and onto the upper sheet. It passes into the 1st quadrant at the first (Snell's law) stationary point, $\theta = \theta_0$. Once again on the lower sheet,

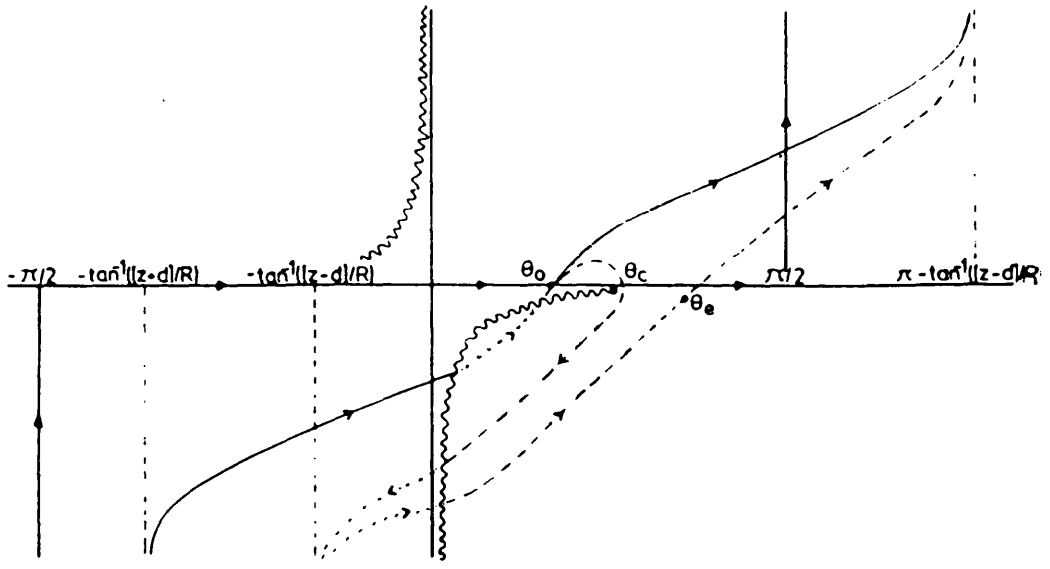

Figure B.1 The contours of integration of the θ integral. ——— : steepest descent contour on lower sheet with no evanescent arrival; ····: steepest descent paths on upper sheet; ----: steepest descent path on lower sheet including evanescent arrival; ∿∿∿ : branch cuts.

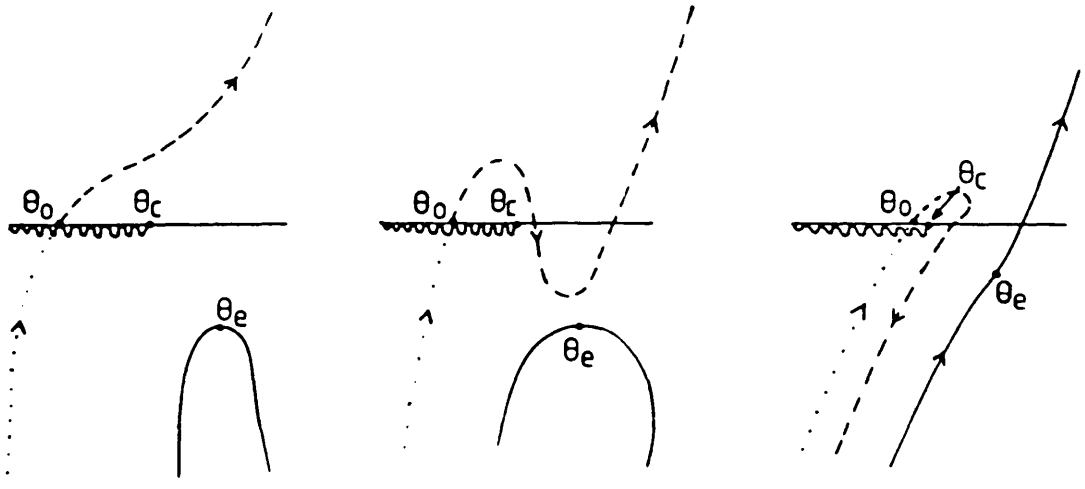

Figure B.2 The behaviour of the steepest descent contour as the field point becomes shallow, *i.e.*, d → 0. ····: Snell's law path on upper sheet; – – – –: Snell's law path on lower sheet; ———: evanescent path on upper sheet; ∿∿∿: branch cuts.

if R is small it then heads directly to $\pi-\tan^{-1}(\frac{L+d}{R})+i\infty$. If R is large enough, however, it curls around $\theta = \theta c$ and returns to the 3rd quadrant and upper sheet at $-\tan^{-1}(\frac{L-d}{R})-i\infty$, before finally arriving at $\pi-\tan^{-1}(\frac{L+d}{R})+i\infty$ *via* the second (evanescent) stationary point, $\theta = \theta e$.

(a) Gerjouy suspected that the change in the contour would occur when

$$\mathrm{Re}[\Phi(\theta_0)] \lesssim \mathrm{Re}[\Phi(\theta e)] \quad . \tag{B.3}$$

The contour has been examined numerically and it has been established that inequality (B.3) is indeed the condition for the inclusion of the second stationary point at θe. Figure B.2 shows the changing contour as the field point (R,L,d) comes closer to the surface. It is of particular interest to note that the behaviour of the contour on the $\mathrm{Re}(\theta)$ axis is not sufficient to determine whether θc should be included. Once the stationary points have been found, however, it is easy to test (B.3). Finding the stationary points was achieved with a simple iteration scheme (also due to Berktay[54]), for real n.

In the vicinity of the stationary point

$$\Phi'(\theta_0+\delta\theta) = \delta\theta\Phi''(\theta o) + O(\delta\theta^2) \quad , \tag{B.4}$$

and hence

$$\delta\theta \simeq \Phi'(\theta_0+\delta\theta)/\Phi''(\theta_0+\delta\theta) \quad . \tag{B.5}$$

Starting with an initial guess for θ_0, equation (B.5) was used to iterate to the stationary point. It was found to be equally efficient around θ_0 or θe, converging to 6-figure accuracy within 7 steps.

To deal with absorption, this solution is perturbed by assuming that if $n = n_r+\delta n$, $\theta_0 = \theta_0^r+\delta\theta$ and substituting in $\Phi'(\theta_0^r) = 0$. Equating powers

of δn and $\delta\theta$ yields

$$\delta\theta = 2n\delta n \left[\sin 2\theta_0 + \left(\frac{n^2 - \sin^2\theta_0}{\frac{d}{4}\sin 2\theta_0} \right)^{3/2} \left\{ R\sin\theta_0 + L\cos\theta_0 + \frac{d\cos 2\theta_0}{(n^2 - \sin^2\theta_0)^{1/2}} \right\} \right]^{-1}, \tag{B.6}$$

(b) Of particular interest in this study were sources just above the interface, *i.e.*, $L \to 0$. Provided d is not too small, nothing untoward happens to the contour, the stationary point equations and asymtotic solutions remain valid.

(c) However, if L is small and $d \to 0$, then $\theta_0 \to \theta_c$ and $\theta_e \to \pi/2$. Neither of these cases is satisfactory for, in the former case $T(\theta)$ changes rapidly, and in the latter $T(\theta) \to 0$. In the comments following equation (3.28), it was noted that the spherical spreading terms $\to 0$ as $\theta_0 \to \theta_c$, but it may be argued that this conclusion is not valid in this region because of the behaviour of $T(\theta)$. In fact, as $d \to 0$, the paths on the upper and lower sheets, which meet at $\theta = \theta_0$, become closer and closer together, until at $d = 0$ they coincide. Therefore, regardless of the detailed behaviour of $T(\theta)$, the contribution from this stationary point will tend to zero as $d \to 0$. The contribution from the second stationary point is not zero however; only the leading term of the asymtotic series for I is zero, so that the most important evanescent contribution to I will be $0(1/k)$ and not $0(1/k)^{\frac{1}{2}}$.

APPENDIX C

The Dispersion of Sound in Sediment

It is well known that a plane wave suffering attenuation in a linear medium must also suffer dispersion. To a good approximation the attenuation of sound through sediment is linear;[55] indeed, it is usually characterised experimentally by measuring $\alpha(\omega)$ (in Np m^{-1}) of the linear attenuating filter $e^{-\alpha(\omega)x}$. Yet, in his extensive review of measurements of the speed and attenuation of compressional waves in sediment, Hamilton[56] was able to conclude: "that velocity dispersion, if present, is negligibly small from a few kHz to the MHz range".

A wave which is attenuated without being dispersed is acausal, *i.e.*, arrives at a receiver before being projected from the source. This is clearly unsatisfactory, and it is natural to enquire how large the variation in phase velocity needs to be in order that a wave, passing through sediment, remains causal. The functional relationship between the attenuation and phase velocity, or equally, the real and imaginary parts of the refractive index, of a causal medium, has been a matter of commonplace discussion in electromagnetic,[57] quantum mechanical[58] and network[59] theory. It has also been widely exploited in acoustics. In three apparently independant papers Ginzberg,[60] Futterman[61] and O'Donnell *et al.*,[62] give discussions of varying sophistication of the application to acoustics of the Kramers-Kronig relationship between the real and imaginary parts of the refractive index; and it has been used by O'Donnell[62] to predict the dispersion of sound in $CoSO_4$ solution and polythene, by Beltzer[63] to predict dispersion in composites, and in particular by Horton[64] to predict dispersion in sediment. Unfortunately, he incorrectly deduced that in the important case of $\alpha(\omega)$ being a linear function of frequency

there is no dispersion; a conclusion which may be shown to lead to acausal absorption. The affect on a plane wave of passing through a linear medium may be characterised by a linear filter

$$p(x_1,t) = p(x_0,t)*f(x_1-x_0,t) \qquad (C.1)$$

The filter $f(x_1-x_0,t)$ must be causal. In addition, we would expect no disturbance to be transmitted from x_0 to x_1 faster than some velocity c_0; thus we may put

$$f(x_1-x_0,t) = g(x_1-x_0,t)*\delta[t-(x_1-x_0)/c_c] \quad , \qquad (C.2)$$

where g(t) is a causal filter such that it is not possible to define a third causal filter h(t) for which $h(t) = g(t)*\delta(t-t_0)$, $t_0 > 0$. Fourier transforming equations C.1 and C.2, denoting transformed quantities by an upper case symbol, and substituting for $F(x_1-x_0,\omega)$ gives

$$P(x_1,\omega) = P(x_0,\omega)e^{-[\alpha(\omega)+i\beta(\omega)+i\omega/c_0](x_1-x_0)} \qquad (C.3)$$

where

$$G(x_1-x_0,\omega) = (1/\sqrt{2\pi})e^{-[\alpha(\omega)+i\beta(\omega)](x_1-x_0)} \qquad (C.4)$$

From equation (C.4), $\alpha(\omega)$ can be identified as the attenuation coefficient in Np m^{-1} and $c(\omega) = [1/c_0+\beta(\omega)/\omega]^{-1}$ as the phase velocity. $\alpha(\omega)$ and $c(\omega)$ are related to the refractive index, $N(\omega) = N_r(\omega)+iN_i(\omega)$, where $N_r(\omega)$ and $N_i(\omega)$ are real functions, by

$$N(\omega) = c_0/c(\omega) + ic_0\alpha(\omega)/\omega \quad . \qquad (C.5)$$

The refractive index has a real causal inverse transform, n(t), and as a

result[60,61 or 62] satisfies:

$$N_r(\omega) - N_r(\omega_0) = 2\left(\frac{\omega^2-\omega_0^2}{\pi}\right)\int_0^\infty \frac{N_i(n)udn}{(u^2-\omega^2)(u^2-\omega_0^2)} \quad , \qquad (C.6)$$

i.e., $N_i(\omega)$ is a known function of ω, then $N_r(\omega)$ is calculable to within a real constant.

The attenuation of sound in a wide range of sediments is characterised by an absorption coefficient which is linear with frequency:

$$\alpha(\omega) = k|\omega| \quad \text{and hence} \quad N_i(\omega) = c_0 k\,\mathrm{sgn}(\omega) \quad , \qquad (C.7)$$

where the modulus is necessary because n(t) is real. Strictly $N_i(\omega)$ is not an analytic function and may not be substituted in equation (C.6). This difficulty may be avoided either by following Futterman[61] and replacing sgn(ω) with an analytic function such as $(1-e^{-\gamma|\omega|})\mathrm{sgn}(\omega)$ and letting γ become large, or by ignoring equation (C.6) altogether and exploiting the causality of n(t) together with the known transforms of generalised functions.[65] Either way it is found that

$$N_r(\omega) = \frac{2c_0k}{\pi}\ln|\omega| + N_0 \quad , \qquad (C.8)$$

where N_0 is a real constant. From the definition of g(t) and equation (C.5), we get

$$N_0 = 1 \qquad (C.9)$$

From equations (C.7), (C.8) and (C.9):

$$\begin{aligned} n(t) &= \delta(t) + 2kc_0/\pi t \quad , \quad t \geqslant 0 \\ &= 0 \quad , \quad t < 0 \end{aligned} \qquad (C.10)$$

The 1/t singularity at t = 0 is physically unacceptable. Its cause is the behaviour of $N_r(\omega)$ as $\omega \to \infty$. This serves to emphasise that equations (C.7), (C.8) and (C.9) are low frequency approximations valid for wavelengths greater than, in the case of sediment, the particle size. Futterman and Ginzberg discuss this point in some detail.

The value of k for the sand used in this study was previously known to be $\sim 4 \times 10^{-6}$ Np m^{-1} s^{-1}. Over a range of frequencies from 50 kHz to 250 kHz, equation (C.8) predicts a variation in phase velocity of the order of 0.5%. A change of this magnitude is well within the scope of relative measurement, if not in absolute value.

The measurement of the phase dispersion

The variation in phase velocity, $\Delta c_p(\omega)$, due to absorption is known to be small; it is therefore much easier to measure this variation directly than to attempt to measure the absolute quantity $c_0+\Delta c_p(\omega)$. If the spectrum of a plane pulse $p(x,t)$ is measured at two locations x_0 and x_1, the phase velocity may be calculated by division. $\Delta c_p(\omega)$ can be distinguished by its non-linear behaviour:

$$c_0 + \Delta c_p(\omega) = \frac{\omega(x_1-x_0)}{\arg[p(x_1,\omega)/p(x_0,\omega)]} \qquad (C.11)$$

Clearly, it is not necessary to know c_0 to measure $\Delta c_p(\omega)$ to an accuracy determined by (x_1-x_0). This method amounts to measuring to total phase difference between the dispersed wave and one travelling at constant velocity c_0 over a distance (x_1-x_0). In liquids, Carstensen's now standard method[66] for measuring $\Delta c_p(\omega)$ is to find the distance (x_0-x_1) for which the total phase difference is 2π. Both methods are essentially equivalent;

but in the case of sediment the difficulty in moving the hydrophone makes the former preferable.

To this end, the receiver, a B + K 8103 hydrophone was buried 40 cm deep in saturated air-free sand at the bottom of a water filled tank, as shown in Figure C.1. The sand used in the experiments was 250 μm diameter (ϕ = 2, σ_ϕ = 0.5) medium sand with a density of 1946 kg m^{-3} and 50% porosity. The sand surface could be smoothed plane by a scraper attached to a trolley running on rails above the tank. The quality of the surface finish was maintained by shining light across the surface at a very acute angle: any imperfection could readily be seen from the shadow it threw.

A truncated parametric array[13] was used to generate a broadband pulse incident normally on the sediment surface vertically above the hydrophone. The received waveform was amplified antialias filtered and recorded digitally on the transient recorder. To reduce the noise to negligible levels each pulse was repeatedly recorded and summed on the computer. (The trigger uncertainty of 0.1 μs introduces an error in the summed estimate; but this may be ignored below 300 kHz.) After each measurement the sand surface was lowered by removing 4 cm of sand and then again smoothed plane. In all, seven such 4 cm steps were taken. The eight recorded pulses are shown in Figure C.2 in order of increasing sand depth.

The velocity c_0 was measured from a graph of arrival time *versus* sand depth removed. It was found that c_0 = 1690 ± 30 ms^{-1}. The spectrum of each pulse was then estimated with the F.F.T. algorithm (512 samples at 0.2 μs). Sediment is not as acoustically homogenous as, say water, nor was it known with any certainty how acoustically repeatable the surface was. The eight spectra allowed more than one estimate of the dispersion and

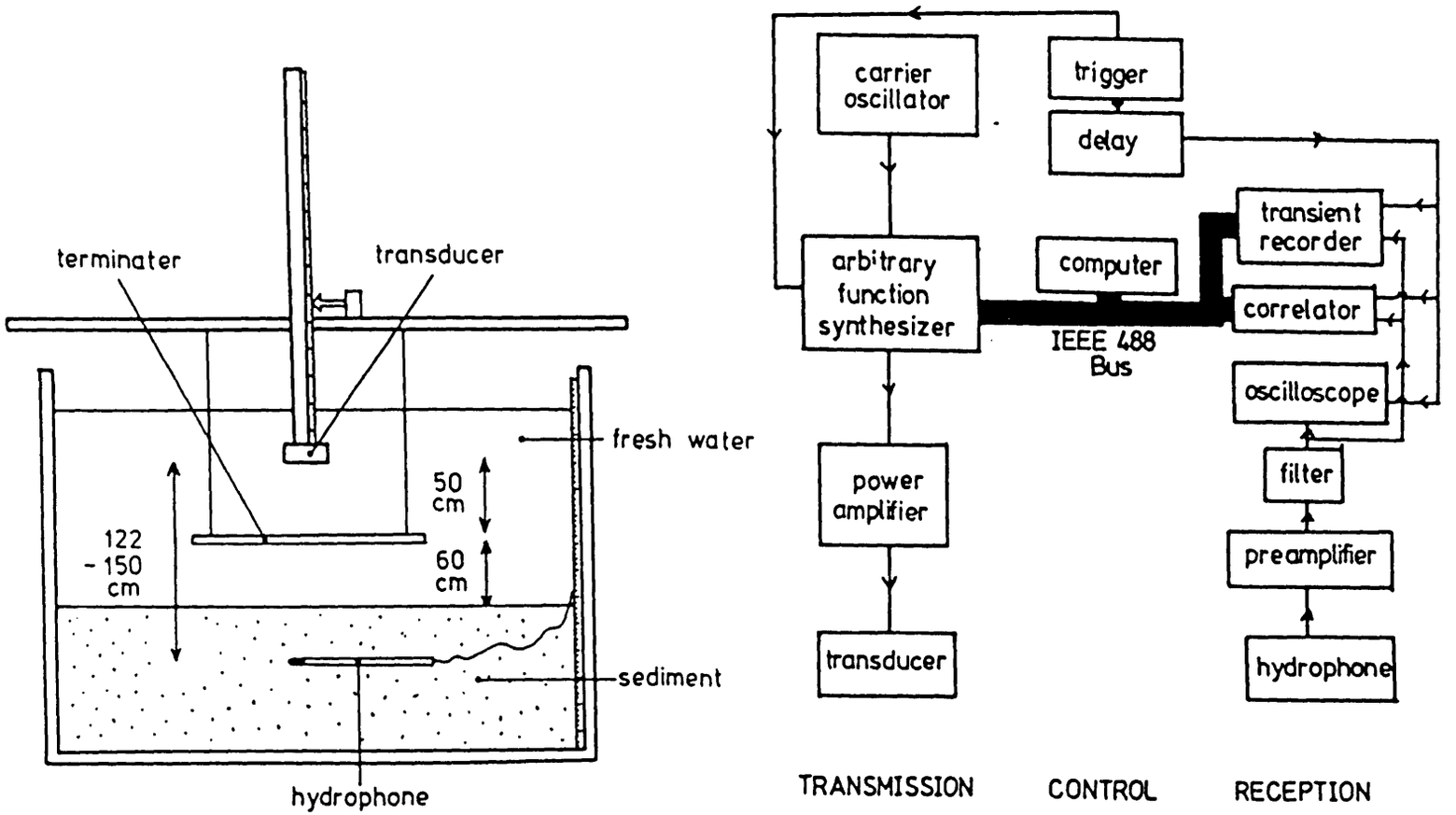

Figure C.1 The experimental arrangement and electronic configuration for the experiments to measure the sound dispersion in sediment.

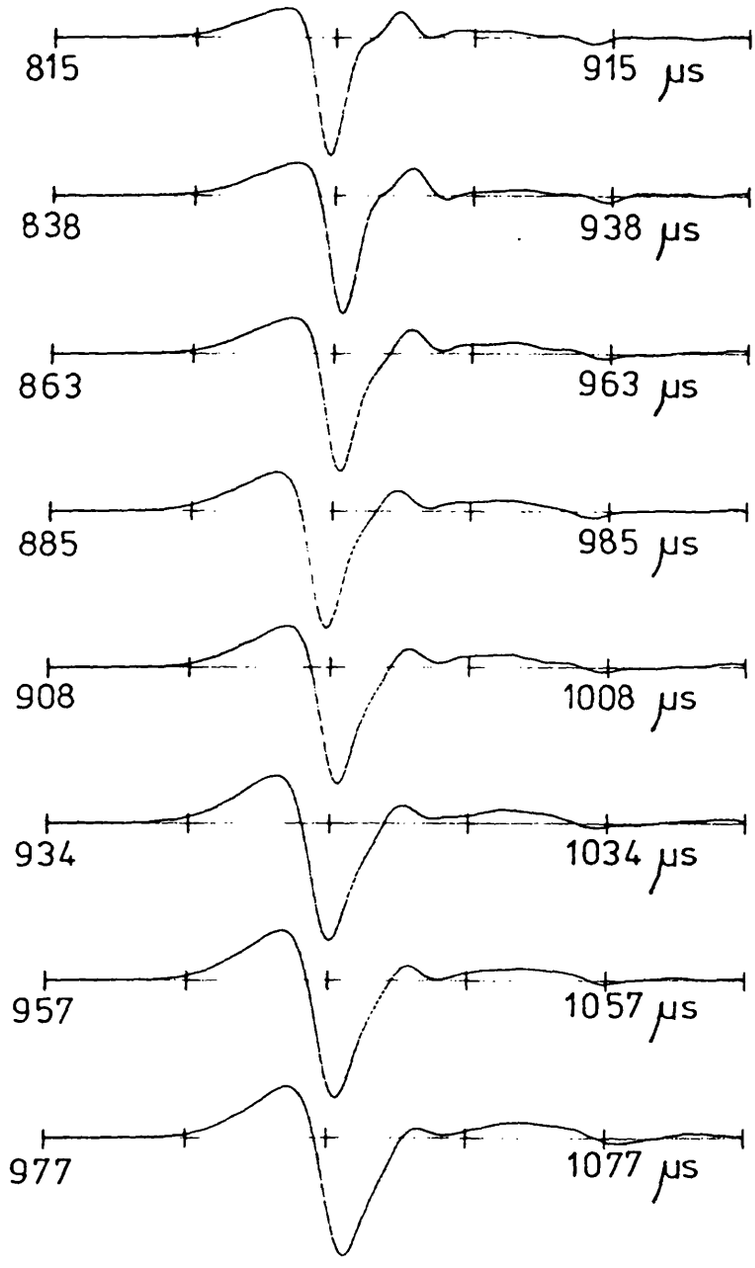

Figure C.2 The eight arrivals in order of increasing path length through sediment (downwards). The phase change from ∿ zero phase to ∿ 90° phase is quite evident.

attenuation at each frequency: seven estimates of the passage through 4 cm; six estimates of the passage through 8 cm, *etc.* Thus the increased dispersion and attenuation at larger separations was partly offset by having fewer estimates. It was found that the single measurement through 28 cm and the average of 4 cm were of poor quality. The remaining estimates of attenuation and dispersion are plotted in figures 24 and 25 respectively.

The attenuation is seen to follow a linear dependance on ω. The solid line in Figure 24 corresponds to a value of $k = 3.9 \times 10^{-6}$ Np m^{-1} s^{-1}. This value for k, and the value measured for c_0, are consistent with values measured previously for the same sand.[48] (This fact helps to confirm that any air has been completely removed from the sane. Earlier investigators have observed anomalous behaviour in sediment[49] for which trapped air is assumed to be responsible.[56])

The solid line plotted in Figure 25 is the functional dependance from equation (C.8): $\Delta c_p(\omega) = 2c_0^2 k \ln|\omega|/\pi$. It can be seen that this curve is as good a summary of the dispersion as $\alpha(\omega) = k|\omega|$ is of the attenuation. The variation over the frequency range measured is indeed small; but it is sufficient nonetheless to ensure that a wave remains causal when passing through sediment.

APPENDIX D

Three Mathematical Results

In this appendix, the derivation of some mathematical results used in the main text is given.

1. The first is the integral

$$I(\lambda) = \int_a^b \psi(t) e^{i\lambda\phi(t)} dt \quad . \tag{D.1}$$

The problem is to find an asymtotic expansion for $I(\lambda)$ in inverse powers of λ as $\lambda \to \infty$, given that $\phi(t)$ has no stationary points on $a < t < b$.

Now

$$\frac{d}{dt}\left(\frac{e^{i\lambda\phi(t)}}{\phi'(t)}\right) = e^{i\lambda\phi(t)}\left[i\lambda - \frac{\phi''(t)}{\phi'(t)^2}\right] \quad ,$$

hence

$$\int_a^t e^{i\lambda\phi(u)} du = \frac{1}{i\lambda}\frac{e^{i\lambda\phi(t)}}{\phi'(t)} + \int_a^t \frac{\phi''(u)}{\phi'(u)^2} e^{i\lambda\phi(u)} du \tag{D.2}$$

Integrating (D.1) by parts:

$$I(\lambda) = \frac{1}{i\lambda}\left[\psi(t)\int_a^t e^{i\lambda\phi(t)} du\right]_a^b - \int_a^b \psi'(t)\int_a^t e^{i\lambda\phi(u)} du\, dt \tag{D.3}$$

and substituting from (D.2) gives

$$I(\lambda) = \frac{1}{i\lambda}\left[\frac{\psi(t)e^{i\lambda\phi(t)}}{\phi'(t)}\right]_a^b$$

$$+ \frac{1}{i\lambda}\left[\psi(t)\int^t \frac{\phi''(u)}{\phi'(u)^2} e^{i\lambda\phi(u)}du\right]_a^b - \frac{1}{i\lambda}\int \frac{\psi'(t)e^{i\lambda\phi(t)}}{\phi'(t)} + \psi'(t)\int^t \frac{\phi''(u)}{\phi'(u)^2}e^{i\lambda\phi(u)}du\,dt,$$

and repeated application of integration by parts and equation (D.2) yields

$$I(\lambda) = \frac{1}{i\lambda}\left[\psi(t)e^{i\lambda\phi(t)}\right]_a^b + O(1/\lambda^2) \quad , \tag{D.4}$$

which is the desired result.

2. The second derivation is the proof of the result

$$I(s_p) = \int_0^\infty \frac{se^{is^2}ds}{(s^2-s_p^2)} = -\frac{e^{is_p^2}}{2}\left[E_1(is_p^2) \begin{matrix} + 2\pi i \\ + 0 \end{matrix}\right] \quad , \tag{D.5}$$

where the upper term is taken if $Im(s_p) > 0$, and $E_1(2)$ is the tabulated exponential integral.[31] To prove equation (D.5), the known integral

$$\int_0^\infty se^{i\zeta s^2}ds = \int_0^\infty \frac{e^{i\zeta u}}{2}du = \frac{i}{2\zeta} \tag{D.6}$$

is multiplied by $e^{-i\zeta s_p^2}$ and the result integrated over ζ from 1 to some limit μ:

$$\int_1^\mu e^{-i\zeta s_p^2}\int_0^\infty se^{i\zeta s^2}dsd\zeta = \frac{i}{2}\int_1^\mu \frac{e^{-i\zeta s_p^2}}{\zeta}d\zeta \quad , \tag{D.7}$$

i.e.,

$$\int_0^{\infty} \left[\frac{s e^{i\zeta(s^2-s_p^2)}}{i(s^2-s_p^2)} \right]_1^{\mu} = \frac{i}{2} \int_1^{\mu} \frac{e^{-i\zeta s_p^2}}{\zeta} d\zeta \qquad (D.8)$$

The limit μ is taken to infinity so as to ensure the integrals converge for all s_p:

$$\frac{s e^{i(s^2-s_p^2)}}{(s^2-s_p^2)} ds = -\frac{1}{2} \int_1^{\pm\infty} \frac{e^{-i\zeta s_p^2}}{\zeta} d\zeta \quad , \qquad (D.9)$$

where the upper sign is taken for $\mathrm{Im}(s_p^2) > 0$. Making the substitution $\rho = \pm\zeta s_p^2$, equation (D.9) becomes

$$I(s_p) = -\frac{e^{is_p^2}}{2} \int_{\pm s_p^2}^{\infty} \frac{e^{\pm i\rho}}{\rho} d\rho \qquad (D.10)$$

and hence

$$I(s_p) = -\frac{e^{is_p^2}}{2} \left[E_1(is_p^2) \begin{matrix} + 2\pi i \\ + 0 \end{matrix} \right] \quad , \qquad (D.11)$$

which is equation (D.5), the desired result. The jump discontinuity when $\mathrm{Im}(s_p) = 0$ is to be expected because the residue at the pole $s = s_p$ is added as the pole crosses the real s axis. Note that if $|s_p|$ is large, E_1 may be replaced by its asymtotic expansion and equation (D.11) becomes

$$I(s_p) \sim -\frac{e^{is_p^2}}{2} \left[\frac{e^{-is_p^2}}{s_p^2} \begin{matrix} + 2\pi i \\ + 0 \end{matrix} \right] \quad . \qquad (D.12)$$

3. (After N.G. Pace). In this last section the rationale for the choice of wideband primary modulation, $v_{wb}(t)$, equation (5.3), is discussed. This choice arose from the natural desire to choose a primary modulation for which the secondary source function s(t) [equation (2.7)] is a delta function. Initially the choise of modulation was a Gaussian:

$$p_m = e^{-n^2t^2} \qquad \text{so that} \qquad s(t) = 4n^2e^{-2n^2t^2}(4t^2-1) \qquad (D.13)$$

The set of functions $s_g(t,n)$ have the interesting property that

$$\int_0^\infty \frac{s_g(t,n)}{n}\,dn = \sqrt{8\pi}\,\delta(t) \quad , \qquad (D.14)$$

so that by summing over an infinity of wavelets from Gaussian modulation, the secondary signal would be a delta function. In practice, the range of n is limited by the transducer bandwidth, so the secondary signal in the water will be

$$s_{wb}(t) = \frac{4}{(n_2-n_1)}\left[n_1e^{-2n_1^2t^2} - n_2e^{-2n_2^2t^2}\right] \quad , \qquad (D.15)$$

where n_1 and n_2 are the upper and lower limits on n. This function is plotted in Figure 16. This choice for $s_{wb}(t)$ has the spectrum

$$s_{wb}(\omega) = \frac{4}{(n_2-n_1)}\sqrt{\frac{\pi}{2}}\left\{e^{-\omega^2/8n_1^2} - e^{-\omega^2/8n_2^2}\right\} \quad . \qquad (D.16)$$

It remains to find what modulation, $p_m(t)$ will produce $s_{wb}(t)$ *via* equation (2.7):

$$\frac{d^2}{dt^2} p_m{}^2(t) = \int_{n_1}^{n_2} \frac{s_g(t,n)}{n} dn = \frac{1}{n_2-n_1} \frac{d^2}{dt^2} \int_{n_1}^{n_2} \frac{e^{-2n^2t^2}}{n^2} dn \qquad (D.17)$$

and the substitution $2n\,t = x$ and an integration by parts yields

$$p_m(t) = \left(\frac{1}{n_2-n_1}\right)^{\frac{1}{2}} \left[\frac{e^{-2n_1{}^2t^2}}{n} - \frac{e^{-2n_2{}^2t^2}}{n_2} + t\sqrt{2\pi}\{\mathrm{erf}(\sqrt{2}n_1t) - \mathrm{erf}(\sqrt{2}n_2t)\} \right]^{\frac{1}{2}} \qquad (D.18)$$

which is choice of envelope function seen in Figure 16(A).

REFERENCES

1. M. Ewing and J.L. Worzel, *Geol. Soc. Am.*, 1948, Mem.27.

2. T.G. Muir, C.W. Horton Sr., and L.A. Thompson, "The penetration of highly directional acoustic beams into sediments", *J. Sound Vib.*, 1979, 64(4), 539.

3. T.G. Muir, "A survey of several nonlinear acoustic experiments on travelling wavefields", Proceedings of the 1973 Symposium on Finite-Amplitude Wave Effects in Fluids, Copenhagen, (Ed) L. Bjørnø, IPC Science and Technology Press (Guildford), 1974.

4. P.J. Westervelt, "Scattering of Sound by Sound", *J. Acoust. Soc. Am.*, 1957, 29(2), 199.

5. M.J. Lighthill, *Maths Revs*, 1958, 19, 915.

6. P.J. Westervelt, "Parametric Acoustic Array", *J. Acoust. Soc. Am.*, 1963, 35(4), 535.

7. C.W. Horton Sr., "The penetration of highly directional acoustic beams into a sedimentary bottom. Part 1", Applied Research Laboratories Technical Report No.74-28, Applied Research Laboratories, University of Texas at Austin, 1974.

8. K. Aki and P.G. Richards, "Quantitative Seismology. Theory and Methods", Vol.1, first edition, W.H. Freeman and Company (San Francisco), 1980.

9. J.N. Tjotta and S. Tjotta, "Theoretical study of the penetration of highly directional acoustic beams into sediments", *J. Acoust. Soc. Am.*, 1981, 69(4), 998.

10. J.N. Tjotta and S. Tjotta, "Reflection and Refraction of Parametrically Generated Sound at a Water-Sediment Interface", Proc. NATO Conf. on Bottom-Interacting Ocean Acoustics, SACLANT ASW Research Centre, Italy, 9-13 June, 1980, (Eds) W.A. Kuperman and F.B. Jensen, Plenum Press (New York), 1980.

11. A.H.A. Moustafa, "Penetration of Acoustic Waves into Sediments", PhD Thesis, Birmingham University, 1979.

12. J. Jarzynski and L. Flax, "Penetration into a sand sediment of difference-frequency sound generated by a parametric array", *J. Acoust. Soc. Am.*, 1978, 63(5), 1365.

13. N.G. Pace and R.V. Ceen, "Time domain study of the terminated transient parametric array", *J. Acoust. Soc. Am.*, 1983, 73(6), 1972.

14. N.G. Pace and R.V. Ceen, "Transient Parametric Arrays Terminated at a Water/Sediment Interface", Acoustics and the Sea-Bed, Proc. Inst. Acoust. Conf., 6-8 April, 1983, (Ed.) N.G. Pace, University of Bath, 1983.

15. H.O. Berktay and A.H.A. Moustafa, "Transmission of Sound across the Boundary between Two Fluids", Proc. NATO Conf. on Bottom-Interacting Ocean Acoustics, SACLANT ASW Research Centre, Italy, 9-13 June, 1980, (Eds) W.A. Kuperman and F.B. Jenson, Plenum Press (New York) 1980.

16. T.G. Muir and J.G. Willette, "Parametric acoustic transmitting arrays", *J. Acoust. Soc. Am.*, 1967, 52, 155.

17. H.O. Berktay and D.J. Leahy, "Farfield performance of parametric transmitters", *J. Acoust. Soc. Am.*, 1974, 55(3), 539.

18. M.B. Moffett and R.H. Mellen, "On parametric source aperture factors", *J. Acoust. Soc. Am.*, 1976, 60(3), 581.

19. M.B. Moffett and R.H. Mellen, "Model for parametric acoustic sources", *J. Acoust. Soc. Am.*, 1977, 61(2), 325.

20. R.B. Dingle, "Asymptotic Expansions: their Derivation and Interpretation", Academic Press (London and New York), 1973.

21. F.W.J. Olver, "Asymptotics and Special Functions", Academic Press (London and New York) 1974.

22. J.A. Stratton, "Electromagnetic Theory", McGraw-Hill Book Company Inc. (New York), 1941.

23. S.I. Aanousen, T. Barkve, J.N. Tjotta and S. Tjotta, "Distortion and harmonic generation in the nearfield of a finite amplitude sound beam", *J. Acoust. Soc. Am.*, 1984, 75(3), 749.

24. J.N. Tjotta and S. Tjotta, "Nonlinear equations of acoustics, with application to parametric acoustic arrays", *J. Acoust. Soc. Am.*, 1981, 69(6), 1644.

25. H.O. Berktay, "Possible exploitation of non-linear acoustics in underwater transmitting applications", *J. Sound Vib.*, 1965, 2(4), 435.

26. R.L. Rolleigh, "Difference frequency pressure within the interaction region of a parametric array", *J. Acoust. Soc. Am.*, 1975, 58(5), 964.

27. L.M. Brekhovskikh, "Waves in Layered Media", second edition, Academic Press (New York), 1980.

28. A. Sommerfeld, "Partial Differential Equations in Physics", Academic Press (New York), 1964, P.242.

29. P.J. Westervelt, "Scattering of sound by sound", *J. Acoust. Soc. Am.*, 1957, 29(8), 934.

30. H.O. Berktay, "Nearfield effects in parametric end-fine arrays", *J. Sound Vib.*, 1972, 20(2), 135.

31. M. Abramowitz and I.A. Stegun, "Handbook of Mathematical Functions", ninth edition, Dover Publications (New York) 1970.

32. B.V. Smith, H.O. Berktay, B.S. Cooper and J.R. Dunn, "Nearfield Effects in Non-linear Acoustics", Underwater Applications of Non-linear Acoustics, Proc. Inst. Acoustics Conf., 10-11 September, 1979, University of Bath, 1979.

33. E. Gerjouy, "Refraction of waves from a point source into a medium of higher velocity", *Phys. Rev.*, 1948, 73(12), 1442.

34. H.O. Berktay and J.A. Shooter, "Nearfield effects in end-fire arrays", *J. Acoust. Soc. Am.*, 1975, 53(2), 550.

35. J.N. Tjotta and S. Tjotta, "An analytical model for the nearfield of a baffled piston transducer", *J. Acoust. Soc. Am.*, 1980, 68(1), 334.

36. J. Zemanek, "Beam behaviour within the nearfield of a vibrating piston", *J. Acoust. Soc. Am.*, 1971, 49(1: Part 2), 181.

37. R.V. Ceen and N.G. Pace, "Acoustic Propagation Behaviour in Sedimentary Material", Progress Report, November, 1977, School of Physics Internal Report, School of Physics, University of Bath, 1977.

38. "DATABASE Arbitrary Function Synthesizer, Preliminary Operating Manual", Database, 1 Vale View Place, Claremont Road, Bath BA1 6QW.

39. D.J. Wingham and N.G. Pace, "Assessment of a Simple Time Domain Model of the Parametric Array", Progress Report, June, 1982, School of Physics Internal Report, School of Physics, University of Bath, 1982.

40. E.N.I. MODEL 2100L POWER AMPLIFIER, Instruction Manual, E.N.I. Inc., 3000 Winton Road South, Rochester, New York 14623.

41. G. Kossoff, "The effects of backing and matching on the performance of Piezo-electric ceramic transducers", *I.E.E.E. Trans. Sonics Ultrasonics*, 1966, SU-13(1), 20.

42. J.M. Pelmore, "The Ultrasonic Properties of some Epoxy Materials", Ultrasonics International 1977 Conf. Proc., IPC Science and Technology Press, 1977, pp 316-322.

43. L.L. Beranek, "Acoustics", first edition, McGraw-Hill Book Company Inc., (New York), 1954, pp 377-382.

44. K. Brendel and G. Ludwig, "Calibration of ultrasonic standard probe transducers", *Acustica*, 1976, 36(3), 203.

45. B. Woodward and R.C. Chandra, "Underwater acoustic measurements on polyvinylidene fluoride transducers", *Electrocomponent Science and Technology*, 1978, 5, 149.

46. R.T. Beyer, "Nonlinear Acoustics", Naval Sea Systems Command, Dept. of the Navy, Office of Naval Research, Arlington, Virginia 22217, U.S.A., 1974.

47. V.F. Humphrey and C.H. Hsu, "Nonlinearity of Cylindrical Hydrophones used for the Measurement of Parametric Arrays", Transducers for Sonar Applications, Proc. Inst. Acoustics Conf., 16-17 December, 1980, University of Birmingham, 1980.

48. P.R. Thomas and N.G. Pace, "Broadband measurements of acoustic attenuation in water-saturated sands", *Ultrasonics*, 1980, January, 13.

49. L.D. Hampton, "Acoustic properties of sediments", *J. Acoust. Soc. Am.*, 1967, 42(4), 882.

50. W.L. Konrad, "Applications of the Parametric Acoustic Source", Underwater Applications of Non-Linear Acoustics, Proc. Inst. Acoustics Conf., 10-11 September, 1979, University of Bath, 1979.

51. H.O. Berktay, B.V. Smith, H.B. Braithwaite and M. Whitehouse, "Sub-bottom Profilers using Parametric Sources", Underwater Applications of Non-linear Acoustics, Proc. Inst. Acoustics Conf., 10-11 September, 1979, University of Bath, 1979.

52. V.F. Humphrey, "The Measurement of Acoustic Properties of Specimens of Limited Size by Use of a Parametric Source", School of Physics Internal Report, University of Bath, 1983.

53. L. Brekhovskikh and Yu. Lysanov, "Fundamentals of Ocean Acoustics", first edition, Springer-Verlag (Berlin), 1982.

54. H.O. Berktay, personal communication.

55. E.L. Hamilton, "South velocity and related properties of marine sediments, North Pacific", *J. Geophys. Res.*, 1970, 75(23), 4423.

56. E.L. Hamilton, "Compressional-wave attenuation in marine sediments", *Geophysics*, 1972, 37(4), 620.

57. J.D. Jackson, "Classical Electrodynamics", second edition, J. Wiley and Sons (New York), 1975, pp 306-312.

58. N.G. Kampen, "S-Matrix and causality condition. I. Maxwell field", *Phys. Rev.*, 1953, 89(5), 1072.

59. H.W. Bode, "Network Analysis and Feedback Amplifier Design", fourteenth edition, Van Nostrand Company Inc., (New York), 1964.

60. V.L. Ginzberg, "Concerning the general relationship between absorption and dispersion of sound waves", *Sov. Phys-Acoust.*, 1955, 1, 32.

61. W.I. Futterman, "Dispersive body waves", *J. Geophys. Res.*, 1962, 67(B), 5279.

62. M. O'Donnell, E.T. Jaynes and J.G. Miller, "Kramers-Kronig relationship between ultrasonic attenuation and phase velocity", *J. Acoust. Soc. Am.*, 1981, 69(3), 696.

63. A.I. Beltzer, "Kramers-Kronig relationships and wave propagation in composites", *J. Acoust. Soc. Am.*, 1983, 73(1), 355.

64. C.W. Horton Sr., "Dispersion relationships in sediments and sea-water", *J. Acoust. Soc. Am.*, 1974, 55(3), 547.

65. M.J. Lighthill, "Introduction to Fourier Analysis and Generalised Functions", fifth edition, Cambridge University Press, 1964.

66. E.L. Carstensen, "Measurement of dispersion of velocity of sound in liquids", *J. Acust. Soc. Am.*, 1954, 26(5), 858.

67. B.D. Simmons and R.J. Urick, "The plane wave reciprocity parameter and its application to the calibration of electroacoustic transducers at close distances", *J. Acoust. Soc. Am.*, 1949, 21(b), 633.